Electron Vortices - Beams with Orbital Angular Momentum

S. M. Lloyd, M. Babiker, G. Thirunavukkarasu and J. Yuan

Department of Physics,
University of York,
Heslington, York, YO10 5DD,
UK*

The recent prediction and subsequent creation of electron vortex beams in a number of laboratories occurred after almost 20 years had elapsed since the recognition of the physical significance and potential for applications of the orbital angular momentum carried by optical vortex beams. A rapid growth in interest in electron vortex beams followed, with swift theoretical and experimental developments. Much of the rapid progress can be attributed in part to the clear similarities between electron optics and photonics arising from the functional equivalence between the Helmholtz equations governing the free space propagation of optical beams and the time-independent Schrödinger equation governing freely propagating electron vortex beams. There are, however, key differences in the properties of the two kinds of vortex beams. This review is concerned primarily with the electron type, with specific emphasis on the distinguishing vortex features: notably the spin, electric charge, current and magnetic moment, the spatial distribution as well as the associated electric and magnetic fields. The physical consequences and potential applications of such properties are pointed out and analysed, including nanoparticle manipulation and the mechanisms of orbital angular momentum transfer in the electron vortex interaction with matter.

CONTENTS

* jun.yuan@york.ac.uk, m.babiker@york.ac.uk

I. INTRODUCTION

Electron vortex beams are a new member of an expanding class of experimentally realisable freely propa-

gating vortex states having well-defined orbital angular momentum about their propagation axis; the prototypical example of which is the much studied optical vortex beam. The term vortex beam refers to a beam of particles - electrons, photons or otherwise - that is freely propagating and possesses a wavefront with quantised topological structure arising from a singularity in phase taking the form $e^{il\phi}$ with ϕ being the azimuthal angle about the beam axis and l an integer quantum number also known as the topological charge (or winding number). The topological structure of the wavefront was first described by Nye and Berry (1974) as a screw-type dislocation in the wavetrains in analogy with crystal defects.

Over the last two decades optical vortices have been a subject of much interest, after the publication of the seminal work of Allen *et al.* (1992) in which the quantised orbital angular momentum of a Laguerre-Gaussian laser mode was examined (the earlier discussion of optical vortices in laser modes by Coullet *et al.* (1989) did not emphasise the quantisation of the orbital angular momentum about the propagation axis). Since then, optical vortices have been intensively studied leading to many diverse applications (Allen *et al.*, 2003, 1999; Andrews and Babiker, 2012), including optical tweezers and spanners for various applications (Dholakia *et al.*, 2002; Grier, 2003; He *et al.*, 1995; Ladavac and Grier, 2004): micromanipulation (Galajda and Ormos, 2001); classical and quantum communications (Yao and Padgett, 2011); phase contrast imaging in microscopy (Baranek and Bouchal, 2013; Fürhapter *et al.*, 2005; Züchner *et al.*, 2011); as well as further proposed applications in quantum information and metrology (Molina-Terriza *et al.*, 2007; Yao and Padgett, 2011) and astronomy (Lee *et al.*, 2006; Tamburini *et al.*, 2011; Thidé *et al.*, 2007). The discussion of photonic spin and orbital angular momentum in various situations, and the similarities and differences between the two types of angular momentum have led to new ways of thinking about, and examining orbital angular momentum in this context. The spin and orbital angular momentum can not be clearly separated in general, i.e without the imposition of the paraxial approximation (Barnett and Allen, 1994; O'Neil *et al.*, 2002; Van Enk *et al.*, 1994), which leads to the possibility of the entanglement of the two degrees of freedom (Khoury and Milman, 2011; Mair *et al.*, 2001). More subtle quantum effects due to the interaction of optical vortices with atoms and molecules involve internal atomic transitions at near resonance with the beam frequency. Here too, optical forces and torques are at play (Allen *et al.*, 1996a; Andersen *et al.*, 2006; Babiker *et al.*, 1994; Lembessis *et al.*, 2011; Surzhykov *et al.*, 2015), leading to the trapping and manipulation of individual atoms in certain regions of the beam profile, with promising applications in the new field of atomtronics (Andersen *et al.*, 2006; Lembessis and Babiker, 2013; Pepino *et al.*, 2010; Seaman *et al.*, 2007), as well as the proposed generation of

atom vortex beams (Hayrapetyan *et al.*, 2013; Lembessis *et al.*, 2014). A related recent advance in matter vortex beams is the realisation of neutron vortex beams in the laboratory (Clark *et al.*, 2015).

Although the basic concepts in terms of beam formation of electron vortices essentially stem from those encountered in the optical vortex case, the electron vortex is distinguished by additional properties, most notably the electric charge and half-integer spin. They are thus fermion vortex states characterised by a scalar field in the form of the Schrödinger wavefunction for non-relativistic electrons and Dirac spinors for the ultra-relativistic electron beams, while optical vortex beams are bosonic states described by vector fields. Furthermore, there are substantial differences in scale. Currently, electron vortices created in a medium-voltage (100-300 kV) electron microscope have de Broglie wavelengths of the order of picometers while optical vortices in the visible range have wavelengths of the order of several hundreds of nanometers. Electron vortex beams can thus probe much smaller features than is possible for the optical vortex beams, and as such the range of applications of electron vortices is predicted to be substantially different from the existing scope of optical vortex beams.

The earliest work on particle vortex beams is due to Bialynicki-Birula and Bialynicka-Birula (2001); Bialynicki-Birula *et al.* (2000, 2001). The current research activity specifically in electron vortex beams was stimulated by work due to Bliokh *et al.* (2007), shortly followed by the experimental realisation in several laboratories (McMorran *et al.*, 2011; Uchida and Tonomura, 2010; Verbeeck *et al.*, 2010). It has now been established that electron vortices can be created inside electron microscopes and there exist a number of techniques for vortex beam creation, including computer generated holographic masks applied in similar ways to those routinely adopted in the creation of optical vortex beams (Heckenberg *et al.*, 1992a,b). This review aims to describe the recent developments in the expanding field of electron vortex physics, and highlight significant areas of potential applications. Specifically, electron vortex beams are hoped to lead to novel applications in microscopical analysis, where the orbital angular momentum of the beam is expected to provide new information about the crystallographic, electronic and magnetic composition of the sample. Chiral-dependent electron diffraction has been detected (Juchtmans *et al.*, 2015, 2016) as well as the demonstration of magnetic-dependent electron energy-loss spectroscopy (EELS) (Verbeeck *et al.*, 2010), and it is predicted that the high resolution achievable in the electron microscope will lead to the ability to map magnetic information at atomic or near-atomic resolution. Additionally, the inherent phase structure of the vortex is considered ideal for applications in high resolution phase contrast imaging, as required for biological specimens with low absorption contrast (Jesacher *et al.*,

2005). Applications of electron vortex beams are, however, not restricted to diffraction, spectroscopy and imaging - the orbital angular momentum of the beam may also be used for the manipulation of nanoparticles (Gnanavel *et al.*, 2012; Verbeeck *et al.*, 2013), leading to electron spanners analogous to the widely used optical tweezers and spanners. Electron vortex states are also relevant in the context of quantum information and, in particular, the electron vortex may potentially be used to impart angular momentum into vortices in Bose-Einstein condensates (Fetter, 2001). The orbital angular momentum and magnetic properties of the electron vortex may also find potential uses in spintronic applications, either in the characterisation of spintronic devices, or in contexts employing spin-polarised current injection, through spin-to-orbital angular momentum conversion processes (Karimi *et al.*, 2012).

Our aim in writing this review has been to strive to provide a report on the current state of the new subject of electron vortex beams and their interactions. We have endeavoured to survey much of the relevant literature, but any omissions of specific references would certainly be inadvert and we would apologise for not having come across them. For more focused prospectives, the readers can consult two recently published papers on the subject (Harris *et al.*, 2015; Verbeeck *et al.*, 2014).

The outline of this review is as follows: section II introduces the quantum mechanics governing the propagation of electron vortex beams, namely the wave equation discussed in the non-relativistic and relativistic regimes. The mechanical and electromagnetic properties arising from the vortex mass and electric charge are then considered, along with the role of the vortex fields in the spin-orbit interaction within the beam. Section III covers the dynamics of the electron vortex in external fields. Section IV discusses the various methods for the realisation of electron vortex beams in the laboratory that have hitherto been considered, drawing comparison with the creation of optical vortex beams wherever such an analogy can be identified. Section V deals with the methods one can use to analyse the various properties associated with vortex beams. The interaction of electron vortex beams with matter is covered in VI. The prospects of using electron vortex beams to determine chirality and other magnetic information are discussed in terms of both theoretical and experimental considerations, with concluding remarks about the field given in section VII.

II. QUANTUM MECHANICS OF ELECTRON VORTEX BEAMS

Freely propagating vortex states having the required $e^{il\phi}$ phase factor may be written as solutions to the Schrödinger, Klein-Gordon and Dirac equations, (Bliokh *et al.*, 2007, 2011; Bliokh and Nori, 2012b; van Boxem

et al., 2013; Karlovets, 2012; Schattschneider and Verbeeck, 2011) yielding non-relativistic, relativistic and spinor electron vortex beams, respectively. The spatial distributions of these vortex solutions may take various forms in the relativistic, non-relativistic and paraxial limits and each state is characterised by the distinguishing feature of a vortex, namely the node on the propagation axis. Such states have been mostly described either by the Bessel functions, prototypes of non-diffracting vortex beams (McGloin and Dholakia, 2005), or by the Laguerre-Gaussian (LG) functions which are well known in optics (Allen *et al.*, 1992), with LG representing a beam with a well defined waist at the focal plane. Since both the Bessel and Laguerre-Gaussian sets of functions form complete orthonormal basis sets, any beam, vortex or otherwise, may be described in terms of these vortex states. In the non-paraxial and relativistic limits of the Dirac equation, the spin of the electron also plays a role, and the particular distribution is modified by a spin-orbit interaction intrinsic to the beam (see section II.D). Note that there is an interesting alternative approach describing electron vortices as a natural consequence of the skyrmion model of a fermion (Bandyopadhyay *et al.*, 2014, 2016, 2017; Chowdhury *et al.*, 2015), but this will not be discussed any further in this review.

The remainder of this section introduces the specific properties of the electron vortex beam mainly in the non-relativistic and paraxial limits, focusing on solutions to the Schrödinger equation. This will not only enable direct comparison with the commonly applied paraxial solutions in optics, a comparison facilitated by the functional equivalence between the Schrödinger and the scalar Helmholtz equations, but also illustrates the most important properties of electron vortex beams and serves as a basis for understanding more complex vortex beams.

A. Phase properties of vortex beams

The phase structure of a vortex wave is topologically different to that of a plane wave. In contrast to a plane wave, with phase-fronts that are normal to the propagation direction, the phase front of the vortex wave describes a helix about the axis of propagation (Nye and Berry, 1974) such that the phase is dependent on the angular position about the axis. This topological structure was first described by Nye and Berry (Nye and Berry, 1974) as screw-type dislocations in wave trains, in analogy with crystal defects. The topological charge l (also called the winding number) quantises this winding such that there are l twisted wavefronts about the beams axis, or equivalently a phase change of $2\pi l$ during a full rotation about the axis, as shown in Fig. 1. The phase factor of $e^{il\phi}$ that gives rise to this helical phase structure is a characteristic feature of orbital angular momentum (c.f. the similar phase factor in the azimuthal components

of the orbital angular momentum-containing hydrogenic wavefunctions). The functions characterising a vortex beam propagating with a well defined axis (taken along the z direction) have a general form which can be conveniently written in cylindrical coordinates $\mathbf{r}(\rho, \phi, z)$:

$$\psi_l(\mathbf{r}, t) = u(\rho, z) e^{il\phi} e^{ik_z z} e^{-i\omega t}, \tag{1}$$

with $u(\rho, z)$ a suitable mode function such as the Laguerre-Gaussian functions (section B1), which are characterised by the azimuthal index l and the radial index p, or the Bessel functions of the first kind (section B2), which are charecterised by just the azimuthal index l. The helical phase structure of the vortex beam leads to the phase at the core of the beam as indeterminate since it is connected to all possible phases of the wave. This central phase singularity is not physically viable, and is compensated by the requirement that all functions must vanish on axis (at the location of the singularity), giving the beam a cross-sectional distribution in the form of a ring, or concentric rings. This has led to the nickname of 'doughnut' beams for a particular class of vortex beams - the Laguerre-Gaussian vortices with non-zero winding number $|l|$, but zero radial index ($p = 0$), each being a bright ring surrounding a central dark core. The requirement that all vortex functions must vanish on axis is, however, not sufficient to describe a vortex beam - there must be some topological difference between a region of the beam containing the vortex, and a region that does not (Nye and Berry, 1974). For the present purposes, the topology of the vortex describes the connectedness of the phase fronts. The phase front of the vortex is topologically distinct from that of a plane wave, as one cannot be transformed into the other through continuous deformations. Similarly, the $l = 1$ phase front cannot be deformed into the $l = 2$ or any other l phase front, and this is the reason why the winding number l has also been termed the topological charge, characterising the 'strength' of the vortex. As has been pointed out earlier, the phase front of any vortex is characterised by the factor, $e^{il\phi}$, leading to a phase singularity along the propagation axis. In order to appreciate the significance of the topological charge we shall assume that the function ψ given in Eq. 1 represents a wavefunction of a vortex beam state of a particle of mass m. It is easy to show that a closed loop integration of the probability current density $\mathbf{j}(\mathbf{r}) = \frac{\hbar}{2mi} \{\psi^*(\mathbf{r}, t)\nabla\psi(\mathbf{r}, t) - \psi(\mathbf{r}, t)\nabla\psi^*(\mathbf{r}, t)\}$ along a path C encircling the axis gives a quantised value proportional to the topological charge of the beam (Bialynicki-Birula et $al.$, 2000).

$$\oint_C \mathbf{j}(\mathbf{r}) \cdot d\mathbf{s} = \frac{2\pi\hbar}{m}l \tag{2}$$

where $d\mathbf{s}$ is a line displacement vector tangential to the path C.

For the vortex beam given in the form Eq. 1 we have

(a) Spiral phase front for l = 1

(b) Phase change in the transverse plane for l = 1

(c) Spiral phase front for l = 3

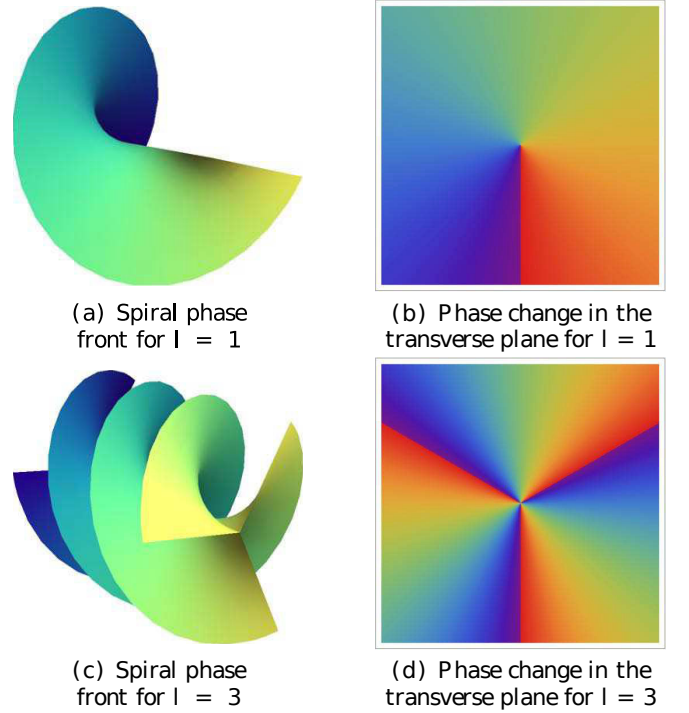(d) Phase change in the transverse plane for l = 3

FIG. 1: (Color online) The phase character of $l = 1$ and $l = 3$ vortex beams. (a) shows the single helix phase front of an $l = 1$ vortex around the beam axis. (b) shows the corresponding continuous phase ramp in one of the transverse plane perpendicular to the beam axis. The total phase change on one rotation is exactly 2π. For the $l = 3$ vortex there are three helical surfaces of constant phase, each move around the axis as shown in (c). This leads to a total phase change on one rotation of exactly 6π. We used wrapped phase representation, with all phase mapped to values between 0 and 2π (represented between blue to red in the 2D phase maps in (b) and (d))), so there are three 'artificial' phase jumps from 0 to 2π in the phase-wrap representation as shown in (d). In both cases, the only real phase discontinuity of significance is on beam axis.

the normalised probability current density

$$\mathbf{j}(\mathbf{r}) = \frac{\hbar}{m} \left(\frac{l}{\rho}\hat{\boldsymbol{\phi}} + k_z\hat{\mathbf{z}} \right). \tag{3}$$

Integrating this about a loop enclosing the z axis gives $\frac{2\pi\hbar}{m}l$, while any other closed path gives zero, showing the topological distinction between a region of space containing the vortex and one that does not. Thus, on circling the z-axis an additional phase of $2\pi l$ is acquired.

B. Vortex beam solutions of the Schrödinger equation

The wavefunction $\psi(\mathbf{r}, t)$ describing an electron vortex beam is a solution of the Schrödinger equation, namely

$$\mathcal{H}\psi(\mathbf{r}, \mathrm{t}) = \mathcal{E}\psi(\mathbf{r}, \mathrm{t}) \tag{4}$$

where $\mathcal{E}$ is the energy eigenvalue. In free space, the Hamiltonian $\mathcal{H}$ is given by the kinetic energy of the electron beam only:

$$\mathcal{H} = \frac{\mathbf{p}^2}{2m} \tag{5}$$

where $\mathbf{p}$ is the linear momentum operator. Equation 4 can be re-arranged to look like the Helmholtz equation for monochromatic light:

$$\nabla^2 \psi(\mathbf{r}, \text{t}) + k^2 \psi(\mathbf{r}, \text{t}) = 0, \tag{6}$$

where k is the wave vector of the electron wavefunction and is given by

$$k^2 = \frac{2\text{m}\mathcal{E}}{\hbar^2} \tag{7}$$

This equivalence is the basis for treating freely propagating electron and light on the same footing, at least at the scalar field level. Indeed the fields of electron microscopy, ion beam physics and accelerator physics started on this basis. The same is true for the electron vortex beam research.

In general, the vortex solution of the Schrödinger equation requires the complex wavefunctions to be identically zero to cope with the phase indeterminacy at the vortex core (Bialynicki-Birula et al., 2000). This means that both real and imaginary parts of the wavefunction should be zero separately. Each condition defines a surface and the vortex core can be considered as the intersection of the two surfaces, resulting in a line of vortex cores. In the following, we first consider two simple solutions in which the vortex core forms a straight line along the z-axis. We then introduce a specific and a general solution, which is more useful in the context of the practical electron vortex beams which are usually generated under bandwidth-limited conditions. In general, the vortex lines can be curved, closed and knotted (O'Holleran et al., 2008), but they can be regarded as a superposition of the simpler straight vortex lines introduced below.

1. Laguerre-Gaussian beams

Optical vortex beams are most commonly discussed in terms of Laguerre-Gaussian modes, as these are a good approximation to the vortex modes created from Hermite-Gaussian laser modes (Lax et al., 1975; Padgett, 1996). The Laguerre-Gaussian vortex beam state arises as a solution of the paraxial approximation of the Helmholtz equation for light or Schrödinger equation for electrons in free space:

$$\left(\nabla_\perp^2 + 2ik_z \frac{\partial}{\partial z} \right) \psi = 0; \tag{8}$$

where ψ is a component of the vector field and the subscript $\perp$ in $\nabla_\perp$ indicates differentiation only with respect
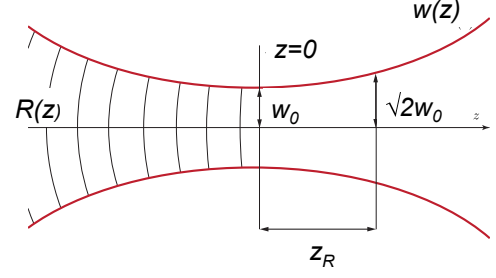

FIG. 2: (Color online) Schematic representation of the Gaussian profile showing the characteristic parameters, namely the width $w(z)$, with w_0 the width at the narrowest part of the beam; z_R the Rayleigh range and $R(z)$ the in-plane radius of curvature at axial position z

to in-plane (transverse) coordinates. This equation describes a component of the relevant field propagating in the z direction with axial wavevector of magnitude k_z. The variations along the axis are considered so small that the second axial derivative may be neglected (Kogelnik and Li, 1966; Lax et al., 1975). The solutions of Eq. 8 represent a vortex for which the magnitude of the transverse momentum $\hbar k_\perp$ is much smaller than the axial momentum $\hbar k_z$ (overall $k_\perp^2 + k_z^2 = k^2$). A suitable vortex solution to Eq. 8 is the Laguerre-Gaussian form, which has a Gaussian envelope modified radially by a Laguerre polynomial, with appropriate phase factors. We have, written in cylindrical polar coordinates $\mathbf{r} = (\rho, \phi, z)$,

$$\psi_{p,l}^{\text{LG}}(\mathbf{r}, \text{t}) = \frac{C_{lp} z_R}{\sqrt{z_R^2 + z^2}} \left(\frac{\sqrt{2}\rho}{w(z)} \right)^l L_p^l \left(\frac{2\rho^2}{w^2(z)} \right)$$
$$\times e^{ik_z z} e^{-i\omega t} e^{il\phi}$$
$$\times e^{\left\{ -\frac{\rho^2}{w^2(z)} + \frac{ik_z \rho^2 z}{2(z_R^2 + z^2)} - i(2p+|l|+1)\tan^{-1}\left(\frac{z}{z_R} \right) \right\}} \tag{9}$$

where $L_p^l(x)$ is the generalised Laguerre polynomial, with azimuthal index l and radial index $p \geq 0$, and normalisation factor $C_{lp} = \sqrt{2^{|l|+1} p! / [\pi(|l| + p)!]}$. The z-dependence of the Gaussian envelope is depicted in Fig. 2, with the characteristic parameters of width $w(z)$ and Rayleigh range z_R given by

$$w(z) = w_0 \sqrt{1 - \left(\frac{2z}{k_z w_0^2} \right)^2}; \tag{10}$$

$$z_R = \frac{k_z w_0^2}{2}. \tag{11}$$

where $w_0 = w(0)$ is the beam radius at focus. The radial profile of the beam varies with the indices p and l. The azimuthal index l is responsible for the beam orbital angular momentum $l\hbar$ per electron and may take any integer value, either positive or negative; whereas the radial

index $p \geq 0$ specifies the number of intensity maxima, i.e. the number of rings in the radial intensity distribution, such that the beam has $p + 1$ maxima (for $l = 0$, the beam has a central spot, and p additional rings). The transverse distributions of the Laguerre-Gaussian beams are displayed in Fig. 3 for various sets of l and p. As can be seen, the modes with $|l| > 0$ have a central minimum, and Eq. 9 has the appropriate $e^{il\phi}$ phase factor, indicating that the Laguerre-Gaussian modes are endowed with the required feature of vorticity.
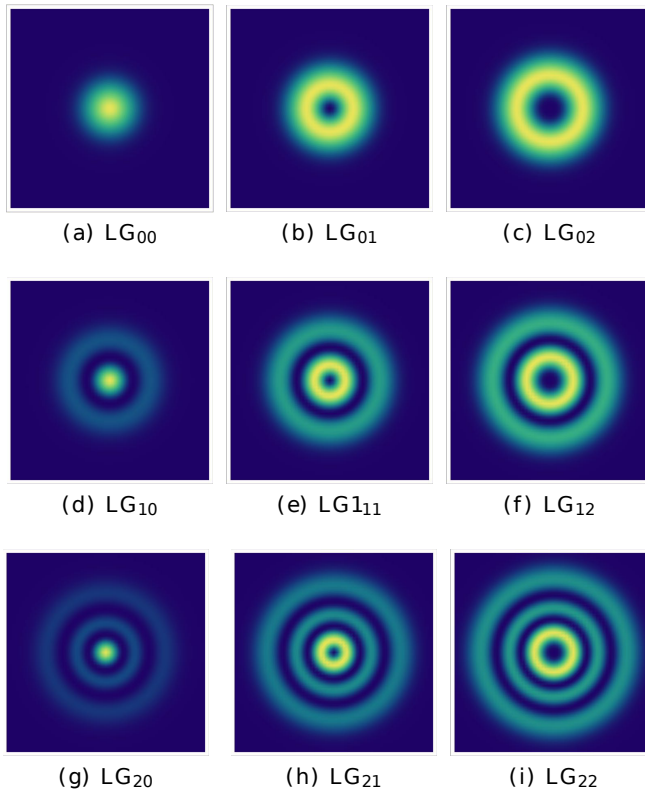

(a) LG$_{00}$ (b) LG$_{01}$ (c) LG$_{02}$

(d) LG$_{10}$ (e) LG1$_{11}$ (f) LG$_{12}$

(g) LG$_{20}$ (h) LG$_{21}$ (i) LG$_{22}$

FIG. 3: (Color online) Intensity distribution patterns for the LG$_{pl}$ modes, shown in the $z = 0$ plane. Intensity is given by $|\psi_l^{\mathrm{LG}}|^2$. The concentric ring structure of the orbital angular momentum carrying modes is clear, with $p + 1$ rings. Colour scale shows the intensity variation within individual modes (not the relative intensity variation across all modes). The Laguerre-Gaussian modes having $l < 0$ have the same intensity distributions as shown above, however the phase (not shown) has the opposite sign.

In addition to the phase factor relating to the orbital angular momentum the Laguerre-Gaussian beam also has a Gouy phase factor:

$$\exp\left[-i(2p + |l| + 1)\arctan\left(\frac{z}{z_R}\right)\right] \qquad (12)$$

which is associated with the focusing of the beam at the waist plane(Feng and Winful, 2001; Petersen *et al.*, 2014). As a result a convergent Gaussian beam experiences a phase change of $\frac{\pi}{2}$ as it passes through the focal plane from $-\infty$ to $+\infty$, whereas the phase shift of the Laguerre-Gaussian beam on focusing is given as

$$-(2p + |l| + 1)\frac{\pi}{2} \qquad (13)$$

The Gouy phase shift arises due to the spatial confinement of the beam, leading to momentum components in the transverse direction that contribute to the dynamic phase of the beam (Feng and Winful, 2001; Petersen *et al.*, 2014). Near the focal plane, the rate of change of the transverse momentum of the Laguerre-Gaussian beam is larger than that of the fundamental Gaussian beam due to the more complex radial profile. The magnitude of the Gouy phase change thus depends on the radial and azimuthal mode indices.

2. Bessel beams

The Bessel-type electron vortex function takes the form

$$\psi_l^B(\mathbf{r}, t) = N_l J_l(k_\perp \rho) e^{il\phi} e^{ik_z z} e^{-i\omega t} \qquad (14)$$

where $J_l(k_\perp \rho)$ is the Bessel function of the first kind, of order l, where, as above, l is the topological charge, or winding number. The wavenumbers k_z and $k_\perp$ are the axial and transverse wave vector components such that $|\mathbf{k}| = \sqrt{k_z^2 + k_\perp^2}$. N_l is a suitable normalisation factor, determined by the specific boundary conditions of the beam. Except for $l = 0$, all other Bessel functions satisfy $J_l(0) = 0$, so that they are suitable for describing a vortex beam. Their spatial distribution functions are functions of the radial coordinate ρ only, so that in contrast to Laguerre-Gaussian beams, freely propagating Bessel beams are non-diffractive (McGloin and Dholakia, 2005), and the use of the full Helmholtz or Schrödinger equations coincides with the paraxial limit in this case. The Bessel beams are indeed the simplest type of vortex beam and so provide an ideal theoretical platform to determine the general characteristics of vortex beams.

The oscillatory nature of Bessel functions gives the Bessel beam a cross-section of concentric rings, decreasing in brightness away from the axis. This concentric ring structure is shown in Fig. 4. However, unlike the Laguerre-Gaussian function, which decays exponentially with radial position, the Bessel function is infinite in extent, so that in principle the beam contains an infinite number of rings. Each ring of the Bessel beam carries the same power in the case of an optical vortex beam (McGloin and Dholakia, 2005) while for electron vortex beams the relevant property is the current, which implies infinite power being carried by the beam, which is of course physically unrealistic. What is meant by a physical Bessel-type beam is a beam that has amplitude modulation similar to a Bessel function, over a
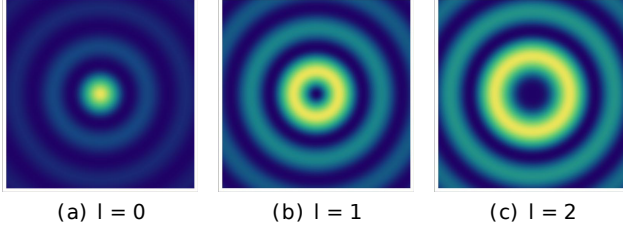
(a) $l = 0$ (b) $l = 1$ (c) $l = 2$

FIG. 4: (Color online) Plots of the intensity $|\psi_l^B(\mathbf{r})|^2$ of a Bessel beam with (a) $l = 0$, (b) $l = 1$, and (c) $l = 2$. The Bessel modes with $l < 0$ have the same intensity distributions as shown above, however the phase (not shown) has the opposite sign.

FIG. 5: (Color online) The Fourier transform of the Bessel beam results in a set of waves of fixed k_z and varying k_x and k_y, such that $k_\perp = \sqrt{k_x^2 + k_y^2}$. The vortex Bessel beam illustrated here has a phase factor $e^{il\varphi}$, so that the phase changes by $2\pi l$ on rotation about the k_z axis. This is illustrated for $l = 1$. The relationship between k_z and $k_\perp$ fixes the cone angle θ.

finite radius, and whose core components behave non-diffractively (such that the central maximum or minimum persists with very little spreading) over a reasonable, but finite, propagation length (McGloin and Dholakia, 2005). These are achievable by several methods in optics including axicon lenses, annular apertures and holograms (Durnin *et al.*, 1987; McGloin and Dholakia, 2005), and have also been generated in electron optics using kinoforms (Grillo *et al.*, 2014a). A kinoform is wavefront reconstruction device (for a reference see (Jordan *et al.*, 1970))

In the momentum representation $\mathbf{k}'(k_\perp', \phi', k_z')$ the Bessel beam has the form

$$\tilde{\psi}_l(\mathbf{k}') = \frac{i^{-l}}{2\pi} \frac{e^{il\phi'}}{k_\perp} \delta(k_z - k_z')\delta(k_\perp - k_\perp'); \quad (15)$$

which is interpreted as a superposition of plane waves of varying $k_\perp$ such that $k = \sqrt{k_\perp^2 + k_z^2}$ for each wave. For a given k_z the possible $k_\perp$ lie on a ring on the surface of constant k, so that there is a cone of plane waves of varying $\mathbf{k}$ that constitute the Bessel beam (Bliokh *et al.*, 2011; McGloin and Dholakia, 2005), with the phase of each given by $e^{il\varphi}$. This is the principle by which axicon lenses produce the rings of a Bessel-type beam (Herman and Wiggins, 1991). The conical propagation leads to another interesting property of the Bessel beam, namely that the original spatial distribution is reconstructed after propagation past an obstruction (MacDonald *et al.*, 1996; McGloin and Dholakia, 2005), as has been demonstrated for electron vortex Bessel beams (Grillo *et al.*, 2014b).

3. Bandwidth-limited vortex beams

In electron vortex beam research, the limited transverse spatial coherence of practical electron sources means that finite radius vortex modes defined using a circular aperture (or pupil) function is more appropriate in real situations. The simplest bandwidth limited vortex beam is generated by the Fraunhofer diffraction of a plane wave by a spiral phase plate with the transmission function:
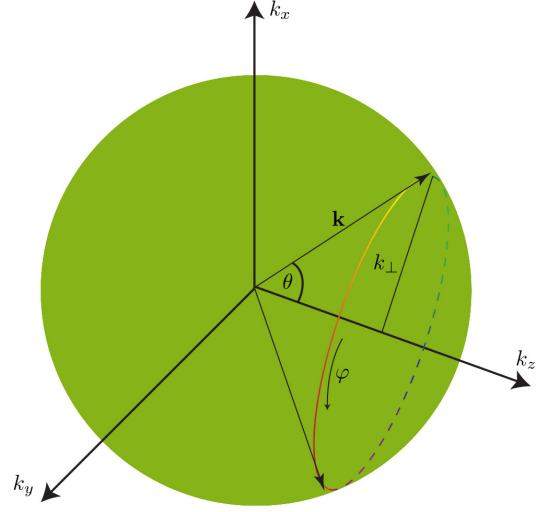
$$\psi(\rho', \phi', z) = e^{il\phi'} e^{ik_z z} \quad (16)$$

through an aperture of finite radius R_{max}. We have used the convention for the momentum/Fourier space representation of the variables as in Eq. 15, since the truncation is in practice taking place in the aperture plane of a convergent electron lens as shown in Fig. 6.

The diffracted beam intensity is related to the Fourier transform of the transmitted wave, which can be written as (Kotlyar *et al.*, 2006, 2007; Lubk *et al.*, 2013a)

$$\tilde{\psi}(\rho, \phi, z) = e^{il\phi} \frac{2\pi i^l 2^{-l} \rho^l R_{max}^{2+l}}{(2+l)\Gamma(1+l)} \times$$
$$_1F_2(1 + \tfrac{l}{2}; 2 + \tfrac{l}{2}; 1 + l; -\tfrac{1}{4}\rho R_{max}^2)(17)$$

where $_pF_q(a; b; c; z)$ is the generalized hypergeometric function. This is a limiting case of Hypergeometric-Gaussian beams (Karimi *et al.*, 2007) due to diffraction of apertured spiral phase masks by a Gaussian beam.

To represent the waveform of the arbitrary beam in similar bandwidth-limited situations, an orthonormal basis set characterised by orbital angular momentum has recently been reported for vortex beams (Thirunavukkarasu *et al.*, 2017), including both the azimuthal and radial quantum numbers l and p, respectively. It is based on describing the normal modes of the transverse wavefront confined to a finite radius at the pupil or aperture plane by an orthonormal set of truncated Bessel functions, much like the solutions of the

allowed normal modes of surface vibrations on a drum surface:

$$\psi_{p,l}^{TBB}(\rho',\phi',z) = N_{p,l}e^{ik_z z}e^{il\phi'}J_l(k_\perp^{p_l}\rho') \text{ for } \rho' \leq R_{max} \tag{18}$$

where the radial and azimuthal indices are p and l respectively following the convention used in the case of LG modes. We again used the cylindrical coordinates (ρ',ϕ',z) to describe the location in the aperture plane and R_{max} is the radius of the circular aperture. The magnitude of the transverse wavevector $k_\perp^{p_l}$ takes the discrete values $\frac{\lambda_{p,l}}{R_{max}}$, with $\lambda_{p,l}$ the $(p+1)^{th}$ zero of the lth order Bessel function J_l, and R_{max} is the radius of the aperture. The truncated Bessel functions, whose amplitudes are for $\rho \geq R_{max}$, together with the azimuthal phase factor form a complete two-dimensional basis set of the OAM modes at the aperture plane. The Fourier transform of these truncated Bessel beams forms a conjugate set of quantum basis set which we termed Fourier Transformed Truncated Bessel Beams (FT-TBB):

$$\psi_{p,l}^{FT-TBB}(k_\rho,\phi,z) = i^l \lambda_{p,l} J_l'(\lambda_{p,l})e^{il\phi}\frac{J_l(k_\rho R_{max})}{k_\perp^{p_l 2} - k_\rho^2} \tag{19}$$

where k_q is the transverse wavevector of the diffracted beams. At the focal plane of a lens of power $1/f$, the corresponding radial displacement (ρ) is given by $f\frac{k_q}{k_z}$ ($\sim f\frac{k_q}{k_0}$). The corresponding wavefunction in the focal plane coordinate (ρ,ϕ) becomes:

$$\psi_{p,l}^{FT-TBB}(\rho,\phi,z) = i^l \lambda_{p,l} \frac{f}{k_0} J_l'(\lambda_{p,l})e^{il\phi}\frac{J_l(k_\rho R_{max})}{\rho_{p_l}^2 - \rho^2} \tag{20}$$

where $\rho_{p,l}$ is the radius of the most prominent doughnut ring and is given by $\frac{\lambda_{p,l}f}{R_{max}k_0}$.

The inset in Fig. 6 shows the schematic phase distribution of some of the low order basis wavefunctions of the truncated Bessel beams (TBB). Also shown is the conjugate relationship between the TBB and and the FT-TBB.

The amplitude and phase of the first three p-modes of the $l=1$ FT-TBB subset are shown in Fig.7 respectively. These results show that the higher order radial modes are distinguished by $p+1$ bright rings, reminiscent of the corresponding LG modes (Allen *et al.*, 1992). However, the similarity does not extend to the additional faint ring structures that can be seen in the amplitude distribution of the FT-TBB$_{1,3}$ mode. These small ringed structures are caused by the ringing effect of the sharply defined aperture. Another noticeable feature is that the largest amplitude occurs when k_ρ approaches $k_\perp^{p_l}$, in which case the wavefunction locally becomes a sinc function of the radial coordinate.

FIG. 6: (Color online) The intensity and phase distribution of the transverse wavefunctions of FT-TBB at $z=0$. Image after Thirunavukkarasu *et al.* (2017) and are plotted for the same relative scale.

FIG. 7: (Color online) Computer-simulated fine structure of the diffraction of Truncated Bessel Beams (FT-TBB): First row for intensity and the second row for the corresponding phase distribution. From left to right, for the FT-TBB vortex beams with $l=1$ but with different radial modes ($p=0,1$ and 2). Images adapted after Thirunavukkarasu *et al.* (2017)

This can also be understood by regarding the original mask as the product of the unobstructed Bessel beam and a top-hat mask function. The transverse structures of the vortex beam at the focal plane can be considered as the convolution of the Fourier transform of the Bessel function (whose transverse structure is a ring with a radius controlled by the radial size of the first dark zone in the mask) and that of the top-hat mask (which is the well known Airy pattern with side band ring structures). This is consistent with the mathematical form of the Fourier transform of the normal modes in the aperture plane. As p increases, the size of the first node ring shrinks and the Bessel ring at the focal plane increases in size. This explains the size changes seen in Fig.7 (first row) for different values of p. The convolution of the Bessel rings with the Airy pattern functions results in side bands, but

they preserve the circular symmetry of the main Bessel peaks. The details of the experimental realization of the FT-TBB beams can be found in ref. (Thirunavukkarasu *et al.*, 2017)

The FT-TBB set of beams is one of the bandwidth-limited vortex beams whose spatial frequency is determined by the aperture size. As this FT-TBB set of modes forms a complete orthonormal set, it can be used to describe any such bandwidth-limited vortex beam. For example, the simplest and most investigated bandwidth-limited electron vortex beam as shown in Eq.17 can be expanded in terms of linear combinations of the FT-TBB set (Schattschneider and Verbeeck, 2011).

Both LG and Bessel beams are unbound solutions and are often discussed in theoretical developments because of their mathematical simplicity. On the other hand, bandwidth-limited beams are required for the precise description of electron vortex beams produced in real situations.

C. Mechanical and electromagnetic properties of the electron vortex beam

The global mechanical properties of electron vortex modes stem from the two basic properties of electrons, namely that the finite electron mass leads to inertial position-dependent mass flux with which are associated global inertial linear and angular momenta of the electron vortex beam while the finite electronic charge leads to position-dependent electromagnetic fields which are further sources of global linear and angular momenta. It is instructive to derive these global properties of the electron vortex with reference to the Bessel type, for mathematical convenience. Here we outline the treatment by Lloyd *et al.* (2013) who were first to show that the mechanical and electromagnetic properties of electron vortices emerge directly from the quantum mechanical wavefunction of the vortex mode. Concentrating on the Bessel-type vortex beam for which the wavefunction is given in Eq.(14) and writing $\omega = \mathcal{E}/\hbar$ we have

$$\psi(\mathbf{r}, t) = N_l J_l(k_\perp \rho) e^{ik_z z} e^{il\phi} e^{-i\mathcal{E}t/\hbar}, \tag{21}$$

The vortex beam is assumed to extend along the axis over a length D which is much larger than the beam width. The normalisation factor N_l follows straightforwardly in the form

$$N_l = \left(\frac{k_\perp^2}{2\pi D \mathcal{I}_l^{(1)}} \right)^{\frac{1}{2}}, \tag{22}$$

where $\mathcal{I}_l^{(1)}$ is the first moment integral of the Bessel function defined by

$$\mathcal{I}_l^{(1)} = \int_0^\infty |J_l(x)|^2 x \, dx. \tag{23}$$

1. Inertial mechanical properties

The inertial mechanical properties are associated with the finite electron mass and these can now be derived as follows. The vortex wavefunction $\psi(\mathbf{r}, t)$ gives rise to a local mass density $\rho_m(\mathbf{r}, t)$ and a mass current density $\mathbf{j}_m(\mathbf{r}, t)$ which are as follows

$$\rho_m(\mathbf{r}, t) = m\psi^*(\mathbf{r}, t)\psi(\mathbf{r}, t); \tag{24}$$

$$\mathbf{j}_m(\mathbf{r}, t) = \frac{\hbar}{2i} \left\{ \psi^*(\mathbf{r}, t)\nabla\psi(\mathbf{r}, t) - \psi(\mathbf{r}, t)\nabla\psi^*(\mathbf{r}, t) \right\}. \tag{25}$$

These emerge on substituting for $\psi(\mathbf{r}, t)$ in the form

$$\rho_m(\mathbf{r}, t) = m|N_l|^2 |J_l(k_\perp \rho)|^2; \tag{26}$$

$$\mathbf{j}_m(\mathbf{r}, t) = \hbar|N_l|^2 \left(\frac{l}{\rho}\hat{\boldsymbol{\phi}} + k_z\hat{\mathbf{z}} \right) |J_l(k_\perp \rho)|^2. \tag{27}$$

where $\hat{\boldsymbol{\phi}}$ and $\hat{\mathbf{z}}$ form, with $\hat{\boldsymbol{\rho}}$, the standard unit vector set for cylindrical coordinates. The unit vector $\hat{\mathbf{z}}$ is along the beam axis.

The evaluation of the global inertial linear momentum of the vortex follows from the realisation that the (local) mass current density ($\mathbf{j}_m$) is the same as the (local) linear momentum density ($\boldsymbol{\mathcal{P}}_m$, i.e. (local) linear momentum per unit volume). The (global) inertial linear momentum vector of the Bessel electron vortex beam ($\mathbf{P}_m$) then follows by volume integration. We have

$$\mathbf{P}_m = \int \boldsymbol{\mathcal{P}}_m(\mathbf{r}, t) dV = \int \mathbf{j}_m(\mathbf{r}, t) dV. \tag{28}$$

We find

$$\mathbf{P}_m = \hbar|N_l|^2 D \times \int_0^\infty \int_0^{2\pi} d\phi \left\{ k_z\hat{\mathbf{z}} + \frac{l}{\rho}\hat{\boldsymbol{\phi}} \right\} |J_l(k_\perp \rho)|^2 \rho \, d\rho. \tag{29}$$

It is easy to see that the azimuthal component in the integrand of $\mathbf{P}_m$ when integrated over the volume leads to a zero value because of a vanishing angular integral. By contrast the z-component leads to a finite result. Direct integration of the z-component in Eq. 29 gives

$$\mathbf{P}_m = 2\pi\hbar k_z D \mathcal{I}_l^{(1)} |N_l|^2 \hat{\mathbf{z}}$$
$$= \hbar k_z \hat{\mathbf{z}}. \tag{30}$$

where we have made use of Eq. 22. The result $\mathbf{P}_m = \hbar k_z \hat{\mathbf{z}}$ is the inertial linear momentum of the Bessel electron vortex beam. Note that the inertial linear momentum is axial, involving only the axial component k_z of the

wavevector component. There are no in-plane components, neither as azimuthal, nor radial, and there is no dependence on $k_\perp$. Note also that the azimuthal linear momentum density is non-zero, but, as we have shown above, its volume integral vanishes. This is consistent with the cylindrical symmetry of the vortex beam.

The (local) inertial orbital angular momentum density ($\mathcal{L}_m$) is defined as the moment of the (local) inertial linear momentum density. We have

$$
\begin{aligned}
\mathcal{L}_m &= \mathbf{r} \times \boldsymbol{\mathcal{P}}_m(\mathbf{r},t) \\
&= \hbar |N_l|^2 \left(\rho \hat{\boldsymbol{\rho}} + z\hat{\mathbf{z}} \right) \times \left\{ \frac{l}{\rho}\hat{\boldsymbol{\phi}} + k_z \hat{\mathbf{z}} \right\} |J_l(k_\perp \rho)|^2.
\end{aligned}
\tag{31}
$$

Integration of this over the volume leads us to the (global) inertial orbital angular momentum vector ($\mathbf{L}_m$). We find

$$
\begin{aligned}
\mathbf{L}_m &= \int \mathcal{L}_m dV, \\
&= \hbar |N_l|^2 \int_{-D/2}^{D/2} \int_0^{2\pi} \int_0^\infty \left\{ l\hat{\mathbf{z}} - \rho k_z \hat{\boldsymbol{\phi}} - \frac{l}{\rho} z\hat{\boldsymbol{\rho}} \right\} \\
&\quad \times |J_l(k_\perp \rho)|^2 \rho d\rho d\phi dz.
\end{aligned}
\tag{32}
$$

It is easy to verify that the angular and radial integrals lead to vanishing results and only the axial component survives. Using Eq. 22 the inertial angular momentum can be written in the form

$$
\mathbf{L}_m = 2\pi l \hbar D \mathcal{I}_l^{(1)} |N_l|^2 \hat{\mathbf{z}} = \hbar l \hat{\mathbf{z}}.
\tag{33}
$$

Equation 33 shows that, in general, the electron vortex beam carries only an axial inertial orbital angular momentum equal to $\hbar l$ and that, as is the case with the inertial linear momentum of the vortex, there are no transverse components. The components of the inertial angular momentum L_x and L_y are both zero as well as the inertial linear momentum components P_x and P_y. It turns out that this feature is not a preserve of electron vortex beams alone and holds for all pure vortex beams including the Bessel- and Laguerre-Gaussian-optical vortex beams.

2. Electromagnetic mechanical properties

We have so far concentrated on the inertial mechanical properties of the electron vortex i.e. those due to

the finite electron mass and such a theory applies to any electrically neutral particle vortex. However, an electron vortex also carries electric and magnetic fields $\mathbf{E}(\mathbf{r})$ and $\mathbf{B}(\mathbf{r})$ by virtue of the finite electric charge and magnetic moment. These fields have been evaluated in Lloyd *et al.* (2012b) for a Bessel electron vortex beam generated under a condition that would be found in an electron microscope. The outlines are as follows.

Direct use of Maxwell's equations with the charge and current distributions of the electron vortex beam considered as sources enables the the evaluation of the specific electric and magnetic fields of the electron vortex. The Bessel electron vortex defined in Eq. 14 possesses cylindrically symmetric charge and current density distributions, each varying only as a function of the radial coordinate ρ, so that the electric and magnetic fields also have such a cylindrical symmetry. Respectively, the charge and current densities for the electron Bessel beam are found to be

$$
\rho_e(\rho) = -e|N_l|^2 J_l^2(k_\perp \rho);
\tag{34}
$$

$$
\mathbf{j}_e(\rho) = -\frac{e\hbar |N_l|^2}{m_e} J_l(k_\perp \rho) \left(\frac{l}{\rho}\hat{\boldsymbol{\phi}} + k_z \hat{\mathbf{z}} \right).
\tag{35}
$$

As with a linear charge and current source, the electron vortex beam possesses an electric field in the radial direction and a magnetic field in the azimuthal direction. In addition, due to the helical (solenoid-like) nature of the charged current density distribution, the Bessel vortex beam is characterised by an axial magnetic field component (Lloyd *et al.*, 2012b). The electric field for the Bessel beam of order l is found to be

$$
\begin{aligned}
\mathbf{E}(\rho) = -\hat{\boldsymbol{\rho}} \frac{e|N_l|^2}{2\varepsilon_0} \times \\
\rho \left(J_l^2(k_\perp \rho) - J_{l-1}(k_\perp \rho) J_{l+1}(k_\perp \rho) \right).
\end{aligned}
\tag{36}
$$

This is valid for any l, including the non-vortex Bessel beam of $l = 0$. Similarly, the azimuthal component of the magnetic field of the same electron vortex beam is found to take the form

$$
\begin{aligned}
B_\phi(\rho) = e\mu_0 \hbar \frac{k_z |N_l|^2}{2m_e} \times \\
\rho \left(J_l^2(k_\perp \rho) - J_{l-1}(k_\perp \rho) J_{l+1}(k_\perp \rho) \right).
\end{aligned}
\tag{37}
$$

Finally, the axial component of the magnetic field is given by the following expression

$$
B_z(\rho) = e\mu_0 \hbar \frac{|N_l|^2}{2m_e} \left(1 - \frac{4^{-l}\rho^{2l} {}_2F_3 \left[\{l, l+\frac{1}{2}\}; \{l+1, l+1, 2l+1\}; -\rho^2 \right]}{l^2 [\Gamma(l)]^2} \right)
\tag{38}
$$

where ${}_pF_q[\{a_1 \ldots a_p\}; \{b_1 \ldots b_q\}; z]$ is the generalised hypergeometric function, and $\Gamma(x)$ the gamma function.

This general form reduces to a series of products of Bessel functions for particular values of l (Abramowitz and Stegun, 1972). The above expressions Eq. 36, Eq. 37 and Eq. 38 are valid for the Bessel beam of infinite radial extent. In order to estimate the field strengths for vortices such as would typically be generated in an electron microscope, the wavefunction Eq. 14 may be truncated after a finite number of rings, i.e.

$$\psi_l^t(\mathbf{r}) = \psi_l(\mathbf{r})\Theta(\rho - \rho_{l,n}) \tag{39}$$

where $\Theta(x)$ is the Heaviside step function, and $\rho_{l,n} = \frac{\alpha_{ln}}{k_\perp}$ is the radius corresponding to the nth zero of the Bessel function of order l, such that $J_l(\alpha_{ln}) = 0$. This wavefunction may then be applied to generate the charge and current densities of the truncated beam, $(\rho_e)_l^t$ and $\mathbf{j}_l^t$, which are the sources for the electric and magnetic fields associated with the truncated vortex beam. We now consider a typical electron vortex beam created in a typical electron microscope. We choose a truncated Bessel beam with a single ring and the following parameters, which are typical for contemporary electron microscopes

Beam energy:	$\mathcal{E} = 200$ keV;
Beam current:	$I = 1$nA;
Axial wavevector:	$k_z = 2.29104 \times 10^{12}$ m^{-1};
Radial wavevector:	$k_\perp = 2.29104 \times 10^{10}$ m^{-1},

the normalisation factor N_l can be expressed in terms of the beam current I, which is a measurable quantity. We have

$$N_l^2 = \frac{Ik_\perp^2 m}{2\pi e\hbar k_z \int_0^{\alpha_{1l}} J_l^2(x)x\,dx}. \tag{40}$$

Figures 8 and 9 show the spatial distributions of the field components for the truncated Bessel vortex beams having $l = 1$ and $l = 10$. The field strengths are seen to be rather small for the parameters chosen. However, the field strengths scale linearly with the electric current (I), so that, in principle, electron vortices with larger field strengths could be produced experimentally. The z-component is particularly interesting, as it arises due to the vortex nature of the beam, and is highly localised in a region of the order of an Å. We also note that although the field strengths are particularly small, their gradients are rather large within the core region and the axial magnetic field gradient is of the order of hundreds of Tm^{-1}. This suggests that the electron vortex can impart a large force on a magnetic particle. Thus the electron vortex beam could potentially find applications in investigation of quantum mechanical phase effects due to localised magnetic systems and has implications for the possibility of observing the Aharonov-Bohm effect (Aharonov and Bohm, 1959) at small scales.

In general the vortex electric field is radial and is a function of the radial coordinate ρ only. It can be written

FIG. 8: (Color online) The electric fields of the Bessel beams of finite radial extent, for (a) $l = 1$ and (b) $l = 10$ respectively. Adapted from Lloyd et al. (2012b)

succinctly as:

$$\mathbf{E}(\rho) = \hat{\rho}E_\rho(\rho), \tag{41}$$

while the vortex magnetic field has two orthogonal components, one axial and another azimuthal

$$\mathbf{B}(\rho) = \hat{\mathbf{z}}B_z(\rho) + \hat{\boldsymbol{\phi}}B_\phi(\rho). \tag{42}$$

The (local) electromagnetic linear momentum density emerges straightforwardly as follows

$$\begin{aligned}\mathcal{P}_{\text{em}} &= \epsilon_0 \mathbf{E} \times \mathbf{B}, \\ &= \epsilon_0 \left\{ \hat{\mathbf{z}}E_\rho B_\phi - \hat{\boldsymbol{\phi}}E_\rho B_z \right\}. \end{aligned} \tag{43}$$

and the corresponding (globle) electromagnetic linear momentum of the vortex beam follows by volume integration. Evaluating the z-integral yields

$$\mathbf{P}_{\text{em}} = \epsilon_0 D \int_0^\infty \rho\,d\rho \int_0^{2\pi} d\phi \left\{ \hat{\mathbf{z}}E_\rho B_\phi - \hat{\boldsymbol{\phi}}E_\rho B_z \right\}. \tag{44}$$

Since the fields are functions only of ρ (Lloyd et al., 2012b), once again we note that the ϕ component gives a vanishing integral and we are left only with the axial component. We have

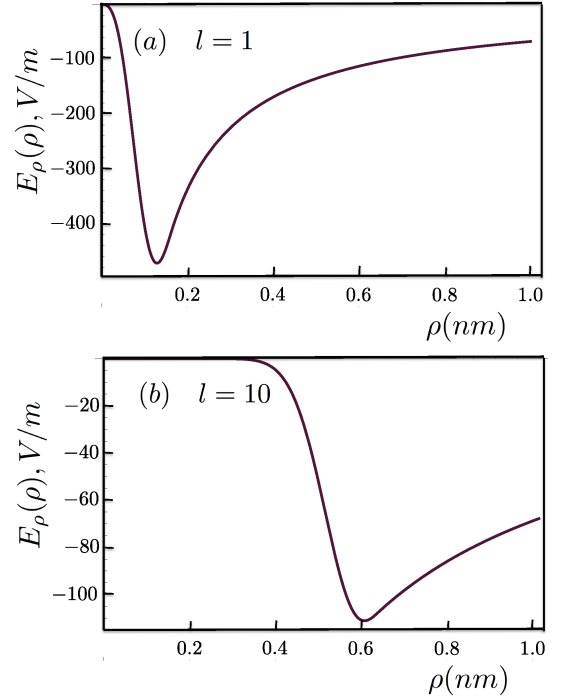$$\mathbf{P}_{\text{em}} = \hat{\mathbf{z}}2\pi\epsilon_0 D \int_0^\infty E_\rho B_\phi \rho\,d\rho. \tag{45}$$
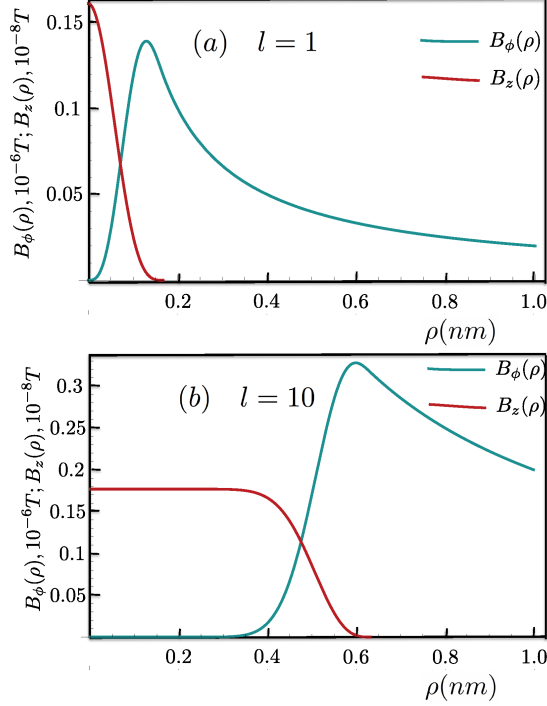
FIG. 9: (Color online) The magnetic fields of the Bessel beam of finite radial extent, for (a) $l = 1$ and (b) 10 respectively. Note that the z-components of the magnetic fields are two orders of magnitude smaller than the ϕ-component. We have assumed that the vortex beam is sufficiently long, as for a current carrying solenoid, allowing us to ignore beam ending effects. Adapted from Lloyd *et al.* (2012b)

The radial integral can be done numerically using expressions for the fields as functions of ρ.

Next we evaluate the electromagnetic angular momentum contributions as the integrals of the moment of the electromagnetic linear momentum density. We have

$$\mathbf{L}_{\text{em}} = \int dV \mathbf{r} \times \boldsymbol{\mathcal{P}}_{\text{em}},$$

$$= \epsilon_0 \int dV \left\{ \hat{\boldsymbol{\rho}} z E_\rho B_z - \hat{\boldsymbol{\phi}} \rho E_\rho B_\phi - \hat{\mathbf{z}} \rho E_\rho B_z \right\}, \quad (46)$$

and it is easy to verify that we have a vanishing ϕ integral. The integral of the ρ component also vanishes and only an axial component remains. We then have

$$\mathbf{L}_{\text{em}} = -\hat{\mathbf{z}} 2\pi \epsilon_0 D \int_0^\infty E_\rho B_z \rho^2 d\rho. \quad (47)$$

Equations 45 and 47 are two further contributions to the mechanical properties of the electron vortex due to the vortex electromagnetic nature to be added to Eqs. 30 and 33 arising from the inertial properties.

Lloyd *et al.* (2013) considered orders of magnitude that could arise in a feasible experimental arrangement as-

suming electron vortices created inside a 1 nA electron microscope of energy 200 keV and transverse wavevector component $k_\perp = 0.01 k_z$. Estimates for the electromagnetic linear and orbital angular momenta in this scenario are found to be as follows

$$P_{\text{em}} \approx 10^{-34} \text{kg m s}^{-1} \quad (48)$$

$$L_{\text{em}} \approx 10^{-48} \text{J s} \quad (49)$$

These are both extremely small compared to the inertial counterparts. The ratios are as follows

$$\frac{P_{\text{em}}}{P_{\text{m}}} \approx 10^{-12}; \quad (50)$$

$$\frac{L_{\text{em}}}{L_{\text{m}}} \approx 10^{-14}, \quad (51)$$

so for practical purposes the electromagnetic linear and orbital angular momenta in such an electron microscope vortex beam are very small. However, in other contexts the electromagnetic contributions could be non-negligible as for example when the vortex beam is created in a linear accelerator.

Lloyd *et al.* (2013) also speculated on the orders of magnitude when electron vortex beams are used to rotate nano-particles. They focused on the effects of the vortex beam on a nano-particle in the form of a small cylinder of radius R and length $d = R$ whose axis is assumed to coincide with that of the vortex beam. A laser beam acts to first levitate the nanoparticle against gravity as well as the axial force of the vortex beam so that we only have rotational dynamics. For orientation as to orders of magnitude we assume that a minimum angular momentum of $\hbar$ is transferred to the nanoparticle. We can estimate a value for the angular frequency of a nanoparticle of fused silica of mass density of approximately $2.2 \times 10^3 \text{kg m}^{-3}$ and radius of 10^{-8} m and we find using $\hbar = I\Omega$ is

$$\Omega \approx 87.6 \text{Hz} \quad (52)$$

where I is the moment of inertia of the particle about its axis. This is much higher than the angular frequency reported by Gnanavel *et al.* (2012) and Verbeeck *et al.* (2013) for a gold nanoparticle on a support. The experiments seem to indicate that the rotation is damped due to friction between the nanoparticle and the support. The set-up described in Lloyd *et al.* (2013) in which the nanoparticle is optically levitated would eliminate the effects of friction due to a support. Nanoparticles of fused silica would be easier to rotate as a controlled optical levitation of a metallic nano-particle would be more difficult to achieve.

D. Intrinsic spin-orbit interaction (SOI)

The spin-orbit interaction arising in the non-relativistic limit is well understood for electrons with orbital angular momentum bound within atomic orbitals; a

similar phenomenon can be described for a vortex propagating in a radially inhomogeneous, but axially invariant field (Leary *et al.*, 2009, 2008; Lloyd *et al.*, 2012b). The source of this coupling is well-known in the case of an external field, however in the case of relativistic electron vortices, an intrinsic spin-orbit interaction is also shown to arise (Bliokh *et al.*, 2011). The origin of the interaction is different in the two cases - the extrinsic, non-relativistic coupling compared to the intrinsic coupling within the relativistic beams - however the coupling mechanisms are similar, and may be viewed as the electron travelling in an effective magnetic field, or alternatively as a manifestation of geometric phase (Bliokh *et al.*, 2011; Leary *et al.*, 2008). The geometrical origins of the spin-orbit coupling have also been invoked to explain the origin of spin-orbit interaction in optical vortices, which of course are unaffected by a magnetic field (Allen *et al.*, 1996b; Bérard and Mohrbach, 2006; Bliokh, 2006; Leary *et al.*, 2009). In this section the effects and basis of the spin-orbit interaction in electron vortex beams are discussed.

In the relativistic and non-paraxial limits, the electron vortex beam exhibits an intrinsic spin-orbit interaction (Bliokh *et al.*, 2011), in which the orbital angular momentum depends upon the spin polarisation of the beam. Setting $c = 1$, the relativistic and non-paraxial electron vortex eigenstates are found to be (Bliokh *et al.*, 2011)

$$\Psi_l = \frac{e^{ik_z z - i\omega t}}{\sqrt{2}} \left[\begin{pmatrix} \sqrt{1 + \frac{m}{E}} \mathbf{w} \\ \kappa \sigma_z \cos\theta \mathbf{w} \end{pmatrix} e^{il\phi} J_l(k_\perp \rho) \right.$$
$$+ i \begin{pmatrix} 0 \\ 0 \\ -\beta\kappa\sin\theta \\ 0 \end{pmatrix} e^{i(l-1)\phi} J_{l-1}(k_\perp \rho)$$
$$\left. + i \begin{pmatrix} 0 \\ 0 \\ 0 \\ \alpha\kappa\sin\theta \end{pmatrix} e^{i(l+1)\phi} J_{l+1}(k_\perp \rho) \right].$$
$$(53)$$

where $\mathbf{w}$, the two component spinor characterizing the electron polarization in the rest frame with $\mathcal{E} = m$, is given by:

$$\mathbf{w} = \begin{pmatrix} \alpha \\ \beta \end{pmatrix}, \qquad (54)$$

with α and β are projections of the spin polarization state in the basic eigenstates of S_z in the electron rest frame and $|\alpha|^2 + |\beta|^2 = 1$. $\kappa = \sqrt{1 - \frac{m}{\mathcal{E}}}$ and the angle θ describing the angle of the cone of Bessel plane waves, as shown in Fig. 5.

It can be seen that two 'extra' modes arise in the relativistic electron vortex solutions, making the relativistic electron vortex a mixed state of l and $l \pm 1$ Bessel modes for spin $s = \pm 1/2$. These modes represent contributions of the small components of the Dirac spinor, and vanish

in both the non-relativistic and paraxial limits. In the non-relativistic limit $\kappa \to 0$, and in the paraxial limit we have $\sin\theta \to 0$ so that the pure l mode is recovered. Such solutions demonstrate that spin and orbital angular momentum are not always separately well-defined except within the paraxial limit, with the relativistic electron vortex solutions showing similarities to the non-paraxial optical vortex solutions which also demonstrate an intrinsic spin-orbit interaction (Barnett and Allen, 1994; Bliokh *et al.*, 2010; Jáuregui, 2004). Such an SOI is described as intrinsic as it does not require the influence of an external field or propagation medium; the non-paraxial or relativistic solutions are eigenmodes of the total angular momentum operator, but not separately of the spin and orbital angular momentum operators (Barnett and Allen, 1994; Bliokh *et al.*, 2010, 2011).

The origin of the intrinsic spin-orbit interaction is geometric in nature, arising from the momentum dependence of the modified spin and orbital angular momentum operators required to maintain the invariance of the total orbital angular momentum $\mathbf{J}$. This leads to a Berry gauge field $\frac{\mathbf{k} \times \mathbf{S}}{k^2}$, with corresponding curvature $\frac{\mathbf{k}}{k^3}$ having a monopole structure (Bliokh *et al.*, 2010, 2011). This monopole curvature leads to the accumulation of Berry phase about the momentum spectrum of the Bessel beam (see Fig. 5), shifting the relative phase of the plane waves and modifying the orbital angular momentum of the beam. The solid angle of the curvature field subtended by the Bessel beam spectrum determines the magnitude of the coupling; a larger range of $k_\perp$ - i.e. a larger cone opening angle θ - increases the Berry phase shift across the spectrum. Thus, in the paraxial approximation the spin-orbit interaction disappears, and spin and orbital angular momentum are fully separable. The geometrical arguments discussed here are also applicable to the extrinsic spin-orbit interactions mentioned above, with the gauge and curvature in such cases originating from a gross orbital trajectory of the beam, such as in the photonic spin and orbital Hall effects (Bliokh *et al.*, 2008; Bliokh, 2006) and the motion of electrons in an inhomogeneous effective magnetic field (Bérard and Mohrbach, 2006; Karimi *et al.*, 2012; Leary *et al.*, 2008) or the propagation of photons in an inhomogeneous medium (Bérard and Mohrbach, 2006; Leary *et al.*, 2009).

Bliokh and Nori (2012b) extended the treatment of the electron vortex to polychromatic beams and showed that such beam can carry intrinsic OAM at an arbitrary angle to the mean momentum of the beam.

III. DYNAMICS OF THE ELECTRON VORTEX IN EXTERNAL FIELD

Electrons subject to an external magnetic field obey a Schrödinger equation in the form

$$\mathcal{H}\psi = \frac{(\mathbf{p} - e\mathbf{A})^2}{2m}\psi. \tag{55}$$

where $\mathbf{p}^{kin} = \mathbf{p} - e\mathbf{A}$ is the kinetic linear momentum operator with $\mathbf{A}$ the magnetic vector potential. For example, for a magnetic field $\mathbf{B}$ in the axial, i.e. z-, direction, the magnetic vector potential is azimuthal in direction:

$$\mathbf{A} = \frac{B\rho}{2}\hat{\boldsymbol{\phi}}. \tag{56}$$

Solutions of the Schrödinger equation in the presence of several different field configurations have been investigated (Bliokh *et al.*, 2012; van Boxem *et al.*, 2013; Gallatin and McMorran, 2012; Greenshields *et al.*, 2012, 2014; Schattschneider *et al.*, 2017; Velasco-Martínez *et al.*, 2016). The Landau configuration involves a constant magnetic field in a fixed direction (Bliokh and Nori, 2012a; Gallatin and McMorran, 2012; Greenshields *et al.*, 2012; Landau and Lifshitz, 1977), whilst the Aharanov-Bohm configuration can involve a single line of flux (Bliokh and Nori, 2012a). The vortex propagation direction may be transverse (Gallatin and McMorran, 2012), parallel (Bliokh *et al.*, 2012; Greenshields *et al.*, 2012) to the direction of the field or in an arbitrary orientation (Greenshields *et al.*, 2014), and the interaction between the magnetic moment with the external field leads to interesting dynamics, as we now explain.

A. Parallel propagation

For the case when the electron vortex is propagating in the same direction as the magnetic field ($\mathbf{B} = B_z\hat{\mathbf{z}}$) the non-relativistic Hamiltonian of the system takes the form (Greenshields *et al.*, 2012)

$$\mathcal{H} = \frac{p_z^2}{2m} + \frac{p_\perp^2}{2m} + \frac{1}{2}m\omega_L^2\rho^2 + \omega_L\left(L_z\hat{\mathbf{z}} + g_s\mathbf{S}\right) \tag{57}$$

where L_z is the axial component of the orbital angular momentum operator, $\mathbf{S}$ the spin vector operator, g_s the gyromagnetic ratio and $\omega_L = \frac{eB_z}{2m}$ the Larmor frequency. Here the subscripts z and $\perp$ stand for axial and transverse vector components respectively.

In the Aharonov-Bohm configuration, with a single line of flux, the solutions to Eq. 55 take the form of Bessel beams, with current density winding around the flux line (Bliokh and Nori, 2012a). Similarly, the coaxially propagating eigenstates of Eq. 55 for a vector potential as in Eq. 56 have the form of non-diffracting Laguerre-Gaussian modes, with a fixed 'magnetic' width (w_B) and magnetic Rayleigh range (z_B) given by the strength of the field (Bliokh and Nori, 2012a; Greenshields *et al.*, 2012).

$$w_B = 2\sqrt{\frac{\hbar}{|e\mathbf{B}|}}; \qquad z_B = 2\frac{\sqrt{2\mathcal{E}m}}{|e\mathbf{B}|}. \tag{58}$$

The presence of the field alters the probability current density (Bliokh and Nori, 2012a); $\mathbf{j} \to \frac{1}{m}\langle\psi|\hat{\mathbf{p}} - e\mathbf{A}|\psi\rangle$, so that the z-component of the observable *kinetic* OAM may be written as

$$\langle L_z\rangle = \frac{m\int\rho j_\phi dV}{\langle\psi|\psi\rangle} \tag{59}$$

The Bessel beam eigenstates of the single flux line take the form

$$\psi^{\mathrm{AB}} = NJ_{|l-\bar{\alpha}|}(k_\perp)e^{i(l\phi+k_z z)}, \tag{60}$$

which are clearly still eigenstates of $\hat{L}_z$, with eigenvalue $\hbar l$, but the observable OAM is now different. Bliokh *et al.* (Bliokh and Nori, 2012a) introduced a parameter $\bar{\alpha} = e\varphi/2\pi\hbar$ where φ is the magnetic flux. The expectation value of the observable *kinetic* OAM is then given by:

$$\langle L_z\rangle = \hbar(l - \bar{\alpha}); \tag{61}$$

while the charge density distribution is also altered - so that Bessel beams with $l = \pm1$ do not have symmetric charge distributions in the presence of an external field. This is due to a Zeeman interaction between the magnetic moment of the beam and the field. Here, though, due to the infinitesimal localisation of the flux line along a node of the Bessel beam, there is no energy or phase shift within the beam.

If the vector potential $\mathbf{A}$ relates to a constant magnetic field $\mathbf{B}$, the beam then undergoes phase and energy shifts. In this case, the eigenfunctions of Eq. 55 take the form of non-diffracting Laguerre-Gaussian modes, being described radially by the Laguerre-Gaussian functions, but having no width variation (Bliokh and Nori, 2012a; Greenshields *et al.*, 2012):

$$\psi^{\mathrm{L}} = N_{l,p}\frac{1}{w_B}\left(\frac{\sqrt{2}\rho}{w_B}\right)^{|l|}L_p^{|l|}\left(\frac{2\rho^2}{w_B^2}\right) \times$$
$$e^{-\rho^2/w_B^2}e^{il\phi}e^{ik_{l,p}z} \tag{62}$$

with w_B given by Eq. 58, and the longitudinal (axial) momentum now depends on the OAM and radial quantum numbers. Since the beam propagates parallel to the field, there is no transverse deflection, and the gross trajectory is unchanged, however the circulation within the vector potential alters the beam phase as well as the observable orbital angular momentum, depending on the relative direction of the circulation of the field and the

electron vortex. The energy eigenvalues take the form

$$\mathcal{E} = \frac{\hbar^2 k_z^2}{2m} - \hbar\omega_L l + \hbar|\omega_L|\left(2p + |l| + 1\right)$$
$$= \frac{\hbar^2 k_z^2}{2m} + \hbar|\omega_L|\left(2n + 1\right); \tag{63}$$

i.e. the dynamics is that of free motion with superposed quantised Landau levels of index n_L, such that

$$n_L = p + \frac{|l|}{2}\left(1 + \mathrm{sgn}(Bl)\right). \tag{64}$$

The second term in the first line of Eq.63 has the form of a Zeeman interaction between the field and the orbital angular momentum, while the third has the same form as the Gouy phase term in the diffracting Laguerre-Gaussian beam, relating to the transverse confinement of the mode (Feng and Winful, 2001). The Landau levels described by Eq. 64 are due to the combined effects of the Zeeman and Gouy phase shifts (Bliokh and Nori, 2012a; Greenshields *et al.*, 2012), where the Zeeman energy shift may be written in terms of the observable orbital angular momentum

$$\mathcal{E} = \frac{\hbar^2 k_z^2}{2m} - \omega_L \langle L_z \rangle; \tag{65}$$

with $\langle L_z \rangle$ incorporating the Gouy phase shift

$$\langle L_z \rangle = \hbar\left(l + \mathrm{sgn}(B)\langle\frac{2\rho^2}{w_B^2}\rangle\right)$$
$$= \hbar\left[l + \mathrm{sgn}(B)\left(2p + |l| + 1\right)\right]. \tag{66}$$

The Gouy and Zeeman energy shifts lead to additional phase accumulation on the propagation of the vortex mode, described by the phase factor of $e^{-i\Delta(z/z_B)}$, with

$$\Delta = \left[l + \mathrm{sgn}(B)\left(2p + |l| + 1\right)\right]. \tag{67}$$

Unlike the Bessel beam eigenfunctions of the single flux line, the charge density distribution of the Landau Laguerre-Gaussian beams are not affected by the external field. On the other hand, the current density is altered in a surprising way, as shown in Fig. 10. If the beam orbital angular momentum vector is parallel to the field direction then the current density flow is in the same direction as that of the free-space Laguerre-Gaussian mode, and the observable OAM is enhanced. For those modes with $l \leq 0$ the observable orbital angular momentum turns out to be independent of the orbital angular momentum of the mode, and is always greater than zero (Bliokh and Nori, 2012a; Greenshields *et al.*, 2012), so that there is now circulation in the current density of those modes with $l = 0$. Additionally, the current density of the modes with $l < 0$ changes direction at the radius of maximum intensity, $\rho_m = w_B\sqrt{\frac{|l|}{2}}$, due to competition between the negative intrinsic vortex current, which dominates at $\rho < \rho_m$, and
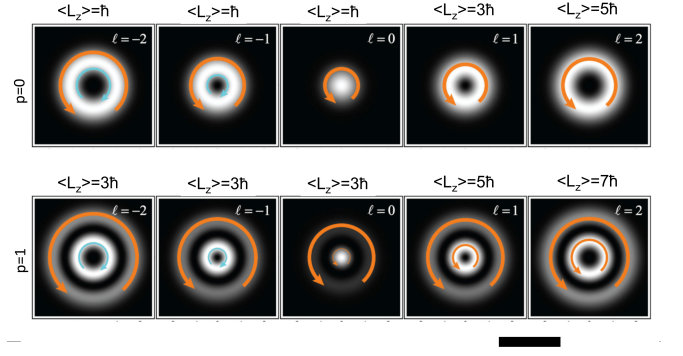

FIG. 10: (Color online) The effect of the magnetic field on the circulating current of the non-diffracting Laguerre-Gaussian vortex modes, for a magnetic field directed in the positive z-direction, such that the vector potential has the same sense of circulation as the $l > 1$ vortex modes. The local character of the azimuthal current is indicated with arrows - it can be seen that the presence of the field induces circulation, even in the modes for which $l = 0$. For those modes with $l > 0$ the observable OAM (listed at the top of each figure) is increased from that of the bare mode, while those beams with $l \leq 0$ have a fixed observable OAM, determined by the field strength and the radial quantum number p. For those beams with $l < 0$ the azimuthal current changes direction at the point of maximum intensity. The top (bottom) panel is for the non-diffracting LG vortex modes with radial index $p = 0$ ($p = 1$). The scale bar length is 2 w_B. Image adapted from Bliokh *et al.* (2012).

the positive circulation induced by the external potential (Bliokh and Nori, 2012a).

Greenshields *et al.* (2014) explored the conceptual issue of conservation of orbital angular momentum for an electron beam in a uniform colinear magnetic field. They showed that the electric field associated with an electron beam with an extended probability distribution, such as that discussed by Lloyd *et al.* (2012b) for electron Bessel beam, when coupled to the external magnetic field, contribute an angular momentum which precisely ensures the conservation of the canonical orbital angular momentum of the electron beam in a magnetic field.

B. Transverse propagation

Substituting Eq.56 into Eq.55 and choosing Laguerre-Gaussian solutions propagating perpendicular to the magnetic field reveals interesting dynamics relating to the orientation of the OAM vector projected onto the electron trajectory - or the helicity of the beam (Gallatin and McMorran, 2012)

$$\Sigma = \mathbf{L} \cdot \mathbf{p}/|\mathbf{p}| \tag{68}$$

In such a field, an electron wavepacket with orbital angular momentum follows the gross circular trajectory expected from classical electrodynamics, orbiting around
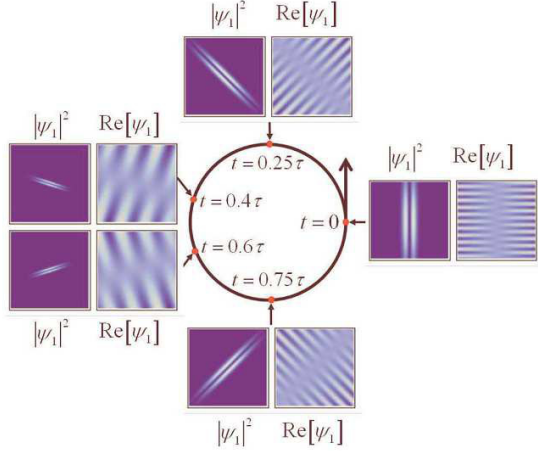
FIG. 11: (Color online) Phase and intensity of the electron wavepacket around the circular cyclotron trajectory. The wavepacket can be seen to rotate at $\omega_L = \omega_c/2$, such that after one rotation the OAM vector points opposite to the original direction. The length and width of the wavepacket also oscillates on rotation, with the cyclotron frequency. Note that the scale of the plots of $\Re(\Psi_1)$ is roughly five orders of magnitude smaller than that of the $|\Psi_1|^2$ plots, so that the phase can be seen. Image from Gallatin and McMorran (2012).

the z-axis at the cyclotron frequency $\omega_c = e|\mathbf{B}|/m$, with the expected quantised Landau levels. The spin helicity is conserved, however the orbital angular momentum vector is found to precess with the Larmor frequency (equal to half the cyclotron frequency), $\omega_L = \omega_c/2$. Thus, on traversing a cyclotron orbit, the resulting orbital angular momentum vector now points in the direction opposite to the initial orientation, as shown in Fig. 11 (Gallatin and McMorran, 2012).

In addition to the rotation of the angular momentum vector, the physical extent of the wavepacket is also found to be oscillatory when the propagating states are not exact eigenstates of the Hamiltonian Eq.55 (Gallatin and McMorran, 2012). Competition between diffractive effects arising from the propagation of the beam and focusing effects arising due to the confinement of the harmonic potential of the gross circular motion cause the length and width of the wavepacket to oscillate, as can be seen in Fig. 11. These effects can be balanced to avoid such oscillations for wavepackets having the characteristic width and the Rayleigh range determined by the strength of the field (Bliokh and Nori, 2012a; Gallatin and McMorran, 2012; Greenshields et al., 2012):

The rotation of the orbital angular momentum helicity has important implications for electron vortex beams subject to transverse external fields. In particular, the transverse field components of the magnetic electron lenses may cause some reorientation of the orbital angular momentum vector as the beam spirals about the focal point. In particular this effect will have consequences for the orientation of the beam orbital angular momentum when the sample is inside the lens field, as the change in orientation will not be reversed by the transverse fields of the opposite direction, at the exit of the lens. On the other hand, these transverse components are small, so that the dominant effect is expected to come from the vortex propagating coaxially with the vector potential.

C. Rotational dynamics of vortex beams

By rotation dynamics, we mean the rotation of the transverse structure of the vortex beams as a function of the distance along the beam axis. As the beams are travelling waves, this can also be considered as time-evolution of the wavefronts. This is to be distinguished from the time-dependent changes in the transverse structure of the vortex beams at a given plane perpendicular to the beam axis. Such time-dependent changes are due to the coherent interference of electron waves with different energies, a process which is more challenging to investigate experimentally.

The phase change due to the influence of a constant magnetic field parallel to the beam axis may be observed in the form of rotations of asymmetric superposition of vortex states (Bliokh and Nori, 2012a; Greenshields et al., 2012; Guzzinati et al., 2013). This effect is very similar to the Faraday effect in optics causing rotation of spin polarisation (Faraday, 1936; Nienhuis et al., 1992). The orientation of linearly polarised optical beams rotates on propagation through a magnetic field, due to circular birefringence acting oppositely on the two spin components. This effect is not observed for optical orbital angular momentum, although a 'mechanical Faraday effect' can be induced with the rotation of the medium though which the optical vortex superposition propagates (Franke-Arnold et al., 2011). In electron beams such an orbital Faraday effect arises due to the Zeeman interaction between the field and the vortex magnetic moment, with apparent rotation due to the difference in the action of the field on the phase of the vortices counter- and co-propagating with the field (Bliokh and Nori, 2012a; Greenshields et al., 2012). Whilst observable in the electron microscope as an image rotation, it is quite distinct from the Lorentz force rotation that is well known in electron lens systems, with the Faraday rotation occurring even when there is no transverse motion of the beam axis with respect to the field.

Although the presence of the field causes a change in the phase as described above, the rotation effect is observable only in the superposition of vortex states, due to the rotational symmetry of the single vortex mode. The superposition may have a zero or an non-zero net angu-

lar momentum, to be referred to as 'balanced' or 'unbalanced' superposition, respectively. In each case the rotation is independent of l, depending instead on the energy of the beam and the strength of the field. For the balanced superposition given by

$$\psi_b = \psi_{l,p}^{LG} + \psi_{-l,p'}^{LG} \tag{69}$$

the intensity distribution is that of a 'petal' pattern with $2l$ lobes. As discussed above, the change in phase on propagation is given as $\Delta z/z_B$. For superposition with fixed energy, the change in phase due to the presence of the field will necessarily be different for each vortex component, with the deviation from the kinetic phase factor given as $k = k_z \mp \mathrm{sgn}(B)\Delta/z_B$ for the $\pm l$ modes respectively. The Gouy phase shift affects both components in the same way, whereas the Zeeman term leads to an l dependent phase of $\mp \mathrm{sgn}(B)lz/z_B$ for the $\pm l$ components. The phase difference between the two beams is observable as a rotation of the interference pattern by an angle (Bliokh and Nori, 2012a; Greenshields *et al.*, 2012)

$$\delta\phi_{l,-l} = \mathrm{sgn}(B)z/z_B. \tag{70}$$

This is independent of l, varying with the strength of the field and the energy of the beam through the characteristic length $z_B = \hbar k_z/m\omega_L$, so the characteristic frequency of the image rotation is the Larmor frequency.

Unbalanced superposition of two or more vortex states are those for which the net angular momentum of the beam is non-zero. For example:

$$\psi_{ub} = \psi_{0,p}^{LG} + \psi_{l,p'}^{LG}. \tag{71}$$

Such a superposition has an intensity profile characterised by l off-axis vortices. In the case of the unbalanced superposition under the influence of the magnetic field, existence of image rotations depends on the relative direction of the field and the beam propagation (Bliokh and Nori, 2012a). For the case when the beam is propagating along the field direction with a net positive OAM, i.e. $l\,\mathrm{sgn}(B) > 0$ the mode rotates on propagation, with the rotation angle given by

$$\delta\phi_{0,l} = 2\,\mathrm{sgn}(B)z/z_B, \tag{72}$$

which is, once again, independent of the value of the orbital angular momentum. On the other hand, for those situations having $l\,\mathrm{sgn}(B) < 0$ there is no image rotation at all, due to the additional Gouy phase terms cancelling with the Zeeman phase acquired from the counter-circulating field (Bliokh and Nori, 2012a).

D. Extrinsic spin-orbit interaction

The extrinsic spin-orbit interaction (SOI) for electron vortex beams arises from the magnetic moment of the electron interacting with an effective magnetic field due to its motion within an inhomogeneous external potential. In order to facilitate SOI in the vortex beam, the external field must be radially inhomogeneous and axially invariant. In the non-relativistic limit, the appropriate SOI may be derived by performing a Foldy-Wouthuysen transformation of the Dirac equation in the presence of fields (Bjorken and Drell, 1964). The Foldy-Wouthuysen transformation is a unitary transformation $U = e^{iS(t)}$, where S(t) is an odd, self-adjoint operator. The Foldy-Wouthuysen transformation diagonalises the Dirac Hamiltonian such that the particle and antiparticle solutions are not mixed, allowing the small components of the spinor wavefunctions to be systematically incorporated and their residual effects ultimately neglected (Foldy and Wouthuysen, 1950). The transformation takes the form

$$\mathcal{H}_{\mathrm{FW}} = e^{iS(t)}\left(\mathcal{H} - i\hbar\frac{\partial}{\partial t}\right)e^{-iS(t)} \tag{73}$$

where H is the Dirac Hamiltonian. Applying the transformation, and expanding in powers of $(mc^2)^{-1}$ yields a series expansion of the Dirac Hamiltonian for particle solutions. The first few terms give the Pauli equation, the non-relativistic Schrödinger equation with relativistic corrections, including the spin-orbit interaction term

$$\begin{aligned}\mathcal{H}_{\mathrm{FW}} =\,&mc^2 + e\Phi + \frac{\mathbf{p}^2}{2m} - \frac{\mathbf{p}^4}{8m^3c^2} \\ &- \frac{e\hbar}{2m}\boldsymbol{\sigma}\cdot\mathbf{B} - \frac{e\hbar^2}{8m^2c^2}\nabla\cdot\mathbf{E} \\ &- \frac{e\hbar}{4m^2c^2}\boldsymbol{\sigma}\cdot\left(\mathbf{E}\times\mathbf{p} - \mathbf{p}\times\mathbf{E}\right).\end{aligned} \tag{74}$$

where Φ is the Coulomb potential. The last term is relevant for the spin-orbit interaction - since we deal with external electrostatic field we have $\nabla\times\mathbf{E} = 0$; additionally $\mathbf{E} = -\nabla\Phi$, so that the SOI may be written as (Leary *et al.*, 2008; Lloyd *et al.*, 2012b)

$$\begin{aligned}\mathcal{H}_{\mathrm{SO}} &= -\frac{e\hbar}{4m^2c^2}\left(\frac{1}{\rho}\frac{\partial\Phi}{\partial\rho}\right)\boldsymbol{\sigma}\cdot(\hat{\boldsymbol{\rho}}\times\mathbf{p}) \\ &= -\frac{e}{2m^2c^2}\left(\frac{1}{\rho}\frac{\partial\Phi}{\partial\rho}\right)\mathbf{S}\cdot\mathbf{L}.\end{aligned} \tag{75}$$

It can be seen that, in contrast to the atomic SOI, only the z-components of the spin and orbital angular momenta are relevant. This SOI Hamiltonian may now be applied perturbatively to the non-relativistic vortex solutions, to find the energy shift for the parallel or antiparallel spin and orbital angular momenta:

$$\delta_{(l,s)} = -\hbar^2 ls\,\langle\psi\,|\,\xi\,|\,\psi\rangle \tag{76}$$

where

$$\xi = \frac{e}{2m^2c^2}\left(\frac{1}{\rho}\frac{\partial\Phi}{\partial\rho}\right). \tag{77}$$

For a positive Coulomb potential, with electric field pointing radially outwards, the parallel (anti-parallel) states shift upward (downward) in energy (Leary *et al.*, 2008; Lloyd *et al.*, 2012b). This causes a splitting of the parallel and anti-parallel states, which can be observed in the rotation of superposition of parallel and anti-parallel states having the same s but opposite l. The interference between such states gives rise to a characteristic 'petal'-like interference pattern. If the parallel and anti-parallel states have slightly different beam energies then the petal-pattern will rotate as a function of time. On the other hand, if the energy is kept fixed then the two states will have different axial momenta, and the pattern will rotate as a function of position (Leary *et al.*, 2008). This allows for the possibility of observation of the relative splitting between the parallel and anti-parallel angular momentum vortex states.

Consider again the electron vortex of section III. The extrinsic spin-orbit coupling results may be used to find the approximate energy splitting of an electron in a vortex beam, travelling within the mean field generated by the beam current. For an electron vortex with $l = 1$, the electric field is of the order of a few hundred Vm^{-1}, giving a splitting of $\mathcal{E}$ of the following magnitude:

$$\Delta_{l=1} \approx 3 \times 10^{-13} \text{ eV} \tag{78}$$

This is very small - too small for direct measurement within the electron microscope, however indirect measurement might be a possibility, such as those involving spin-flip processes of a spin-polarised beam.

In the optical vortex case, the role of the external field is played by the refractive index of an inhomogeneous, anisotropic medium (Marrucci *et al.*, 2006). The coupling between the spin and orbital angular momentum of light has been exploited in the generation of polarised optical vortices, using specially structured liquid crystal cells, known as q-plates (Marrucci *et al.*, 2006; Marrucci, 2013). Particular choices of the liquid crystal structure allow for the complete conversion of spin angular momentum into orbital angular momentum, controlling the sign of the resulting OAM through the polarisation of the input mode. A similar conversion process for electron vortex beams, involving q-plates, involving a specially structured magnetic field configuration, has also been proposed (Grillo *et al.*, 2013; Karimi *et al.*, 2012).

E. Electron vortex in the presence of laser fields

The Schrödinger equation of a quasi-relativistic electron vortex beam in the presence of electromagnetic field has been set out in Lloyd *et al.* (2012a). For relativistic electron beams, a second order Dirac equation incorporating a transverse electromagnetic field **A** is given by

$(c = 1)$:

$$\left[(\hat{\mathbf{p}} - e\mathbf{A})^2 - m^2 - \frac{ie}{2} F_{\mu\nu} \sigma^{\mu\nu} \right] \Psi = 0 \tag{79}$$

where $\hat{\mathbf{p}}^\mu = (i\partial_t, -i\triangledown)$ is the electron four momentum operator, $F_{\mu\nu} = \partial_\mu A_\nu - \partial_\nu A_\mu$ is the electromagnetic field tensor. $\sigma^{\mu\nu}$ is the spin tensor defined by $2\sigma^{\mu\nu} = \gamma^\mu\gamma^\nu - \gamma^\nu\gamma^\mu$, with γ^μ the 4x4 Dirac matrices. Bialynicki-Birula and Radożycki (2006) have shown that classical (cyclotron) and quantum (Landau) orbits of a charged particle in a constant magnetic field can be controlled by electromagnetic waves with embedded vortex lines.

One area of interest is in the interaction of electron vortex beam in the presence of strong field generated by an ultrashort light pulse. Hayrapetyan *et al.* (Hayrapetyan *et al.*, 2014) examined the case of a head-on collision of a relativistic electron vortex beam and a short laser pulse and have shown that the orbital angular momentum components of the laser field couple to the total angular momentum of the electrons, causing the centre of the beam to be shifted with respect to the centre of the field-free electron vortex beam. Theoretical estimates suggest that a shift of 0.02 nm may be induced in a 300 kV electron vortex beams using a moderately strong laser pulse, so experimental observation is challenging but feasible.

Ivanov (2012b) considered the case for electron-photon interactions and demonstrated the entanglement arising from conservation of the sum of the helicity shown in Eq.(80) below for particle-particle collisions also applies in the case of electron-photon interactions. There are also plans to use inverse Compton scattering of laser light by electron vortex beams to generate structured X-ray beams (Seipt *et al.*, 2014)

In addition to the dynamics of the interactions of freely propagating vortices and anti-vortices, collisions between electrons and other particles carrying orbital angular momentum may also be considered (Ivanov and Serbo, 2011; Ivanov, 2012b; Jentschura and Serbo, 2011; Seipt *et al.*, 2014), with implications for generating high energy vortices of various species. In such two-particle scattering situations, there are several possible outcomes - the particles may be scattered to a range of final states, including plane-plane or vortex-plane wave states (Ivanov and Serbo, 2011; Jentschura and Serbo, 2011), or vortex-vortex entangled states (Ivanov, 2012b). In high energy electron-particle scattering, due to the scattering geometry, such collision processes are suitably described by consideration of the orbital helicity of each particle, i.e. the projection of the orbital angular momentum onto the particles momentum. When both particles are allowed to scatter into a final vortex state from an initial plane-vortex collision it is found that there are two degrees of entanglement between the two states - the transverse momentum $k_\perp$ and the orbital helicity, Σ. It is found that

the sum of the helicities of the two final states is approximately the same as the helicity of the incident vortex state, i.e.

$$\Sigma_{f,1} + \Sigma_{f,2} \approx \Sigma_i, \tag{80}$$

the larger helicity tending to accompany the larger transverse momentum, which may fall within a range determined by the transverse momentum of the incident vortex (Ivanov, 2012b). This result may be applied to generate vortex-entangled particles or different species by collision, or additionally opens up the possibility of applying vortex states to high energy particle physics through colliding high energy vortex electrons with protons or other particles.

IV. GENERATION OF ELECTRON VORTEX BEAMS

Due to the similarities between the wave equations for electron and optical vortices, it has in many cases been relatively straightforward to adapt successful ideas from optical vortex research to similar ends in electron vortex applications. For the particulars of optical vortex generation, we refer the reader to the recent reviews (Molina-Terriza et al., 2007; Yao and Padgett, 2011). Broadly, the methods by which electron vortex beams may be generated may be classified into three main categories involving phase plates, diffractive optics and electron optics; with those based on phase plates and diffractive optics being analogues of optical vortex technologies, and electron optics methods forming an entirely new area. Initial success in electron vortex beam production involved materials-based diffractive elements and phase plates, however the electron optics approach appears promising in terms of versatility and overcoming the efficiency limitations of the holographic plates (Yuan, 2014). In addition, photoemission has been considered to be a possible source of electron vortex beams (Takahashi and Nagaosa, 2015).

A. Phase plate technology

The concept of the phase plate for an electron beam is not new (Nagayama, 2011), with early examples such as the Zernike phase plate designed for enhancing phase contrast of biological materials (Kanaya et al., 1958). In the absence of any external fields, the effective refractive index for an electron travelling within a solid is given by (Reimer and Kohl, 2008)

$$n_{\text{eff}} = 1 - \frac{eU}{\mathcal{E}} \frac{\mathcal{E}_0 + \mathcal{E}}{2\mathcal{E}_0 + \mathcal{E}} \tag{81}$$

where $\mathcal{E}_0$ is the electron rest mass energy, $\mathcal{E}$ the kinetic energy of the incident electron, U the material specific mean inner potential. For example, n_{eff} is approximately

1.00082 in silicon nitride for 100 keV electrons. The relative phase shift for a material of thickness Δt is then give by

$$\Delta\phi = 2\pi(n_{\text{eff}} - 1)\frac{\Delta t}{\lambda} \tag{82}$$

For example, to achieve a relative phase delay of π for a 200 keV beam, which has a wavelength of 2.5 pm, a thickness difference in a silicon nitride film of 42 nm is required (Shiloh et al., 2014) (the precise thickness may vary (Bhattacharyya et al., 2006; Grillo et al., 2014a; Harvey et al., 2014), depending on many experimental factors such as the crystallinity of the film, the surface coating both intended and incidental such as carbon contamination).

Spiral phase plates are well known in optical vortex beam generation (Sueda et al., 2004; Turnbull, 1996; Yao and Padgett, 2011), and consist of a thin film plate of a refractive material whose thickness changes continuously about the axis. The helical shaped thickness profiles of the plates impart angular momenta to a transmitting laser beam. Phase plates may be produced for millimetre wavelengths down to optical wavelengths (Sueda et al., 2004; Turnbull, 1996; Yao and Padgett, 2011).

The first experimental demonstration of an electron vortex beam by Uchida and Tonomura (2010) involved the use of a stepped spiral phase plate constructed of stacked graphite flakes. Their stepped phase plate was made of spontaneously stacked flakes of graphite, leading to a discrete - rather than a continuous change of its thickness profile. The edges of the steps cause extra phase jumps, to appear at different points in the beam cross-section - in addition to the discrete 2π phase change of the desired vortex structure. This was observed in Uchida and Tonomura's experimental results via interference patterns and in-plane phase profile. The transmitted beam thus did not demonstrate the required characteristics of a pure vortex state with integer orbital angular momentum, but was nevertheless the first experimental demonstration of a freely propagating mixed vortex state. However, the particular arrangement of the graphite flakes cannot be properly controlled and they lead to phase defects. In addition, being made of carbon, under the influence of the high energy electron beam the flakes are subject to damage and deformation, and the phase plate loses its integrity. As such, the stepped graphite phase plate is not suitable for long-term, reproducible vortex generation.

The production of continuous spiral phase plates has recently been attempted using focused ion beam etching of a silicon nitride membrane (Shiloh et al., 2014). However, the resulting doughnut-shaped beam profile has an opening, indicating a non-integer vortex beam has been produced (Berry, 2004), probably because of the difficulty of achieving precise refractive index and wavelength matching requirements. It has been estimated that 1 nm

thickness error results in $2 - 3\%$ unwanted variation in phase. On the other hand, a similar phase variation can be obtained by a change of 1 kV in the electron energy, indicating that there is some room for adjustment after the phase plate has been made. Thus the challenge of fabricating the spiral phase plate for electron vortex beam is to produce a thickness profile to the required smoothness and precision. Another inherent problem of using matter-based electron-optical elements is the unavoidable scattering of the transmitted electrons other than those arising from mean inner potential. This can cause undesired effects such as additional phase shift or loss of coherence.

B. Holographic diffractive optics

Holographic reconstruction is a well known technique in both optical and electron microscopy (Gabor, 1948; Saleh and Teich, 1991; Tonomura, 1987). It has been used to increase image resolution by reconstructing the image from the interference pattern between the diffracted and non-diffracted components of the incident wave. The same principles of holography may be used to reconstruct an image or a wavefunction. The method involves passing an input wave though a computer generated hologram (CGH) generated via the interference between a reference wave and the required output mode. Most of the holographic diffractive optical masks produced to date are constructed out of thin membrane films of materials such as silicon nitride. This can either be of varying thicknesses for phase grating structures or can be of a uniform thickness with additional heavy metal coating, forming a binary amplitude grating structure. There has also been a proposal to use the Kapitza-Dirac effect to produce electron vortex beams by the formation of optical dislocated gratings (Handali *et al.*, 2015). When a pulsed laser source is used this method enables pulsed electron vortex beams to be produced for use in time-resolved studies.

The holograms employed in vortex optics are constructed from the interference pattern between the vortex mode and a non-vortex reference wave:

$$I_{holo}^2(\mathbf{r}) = |\psi_{vortex} + \psi_{ref}|^2 \qquad (83)$$

where the choice is often for the reference wave to be a tilted plane wave, although other waves such as spherical reference waves (Saitoh *et al.*, 2012; Verbeeck *et al.*, 2012) can also be used.

The holographic masks for vortex beam generation are versatile and are relatively easy to produce; however, they also have their drawbacks. Most of the masks reported to date are based on binary amplitude modulation holography (Clark *et al.*, 2012; McMorran *et al.*, 2011; Verbeeck *et al.*, 2010), and as such produce very

low intensity in the desired diffraction orders, of approximately 6% of the incident beam intensity. This is because most of the beam intensity incident on the mask is blocked, although improvements have recently been reported with the use of phase modulation holograms (see section IV.B.3). Furthermore, since multiple diffraction modes are produced in the binary holographic mask, the isolation of a mode of interest for specific applications can be tricky (Idrobo and Pennycook, 2011; Krivanek *et al.*, 2014; Pohl *et al.*, 2016) and this feature limits the practical use of holographic masks as a vortex beam generator.

1. Binarised amplitude mask

Direct interference of a vortex beam with a plane reference wave produces a characteristic pattern of fringes with smoothly varying intensity. The reproduction of this continuous variation, either in terms of varying film thickness or some other properties of the materials, is as, or even more, technically demanding as the fabrication of a smoothly varying spiral phase plate. A more practical alternative is to replace the continuous intensity variation by a discrete variation, such as the selective total removal of material in order to mask the beam, such that empty spaces correspond to fringe maxima, and material regions of beam blocking thickness correspond to minima of the interference pattern. Such a mask is known as a binary amplitude hologram, and is well known in optics (Lee, 1979). For electron beams, binary holographic masks may be relatively simply fabricated by focused ion beam (FIB) etching or electron lithography. Using such a binarised CGH mask, Verbeeck *et al.* (2010) produced the first pure electron vortex beam. The principles behind

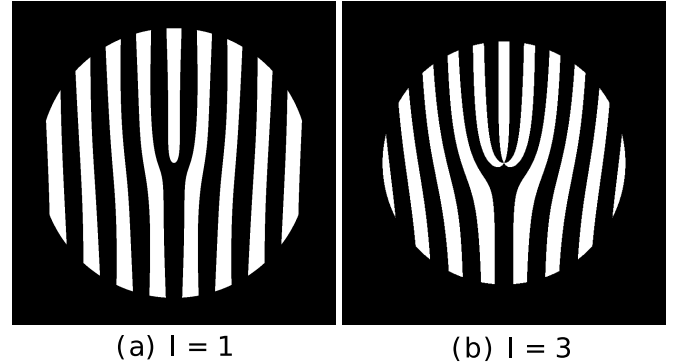(a) l = 1   (b) l = 3

FIG. 12: The typical forked mask pattern produced by binarisation of the interference pattern between a Bessel vortex wave and a plane reference wave for (a) $l = 1$ beam, and (b) $l = 3$ beam.

generating a suitable binarised transmission grating can be demonstrated using the case of a simple vortex mode travelling in the z direction (neglecting any normalisation

factors, see section II.B.3) given by

$$\psi_{vortex}(\mathbf{r}) \equiv \psi_l(\mathbf{r}) = e^{il\phi}e^{ik_z z} \qquad (84)$$

The hologram pattern is generated by the interference of this mode with a reference plane wave travelling at an angle such that k_x is the component of the plane wave momentum orthogonal to the z direction:

$$\psi_{ref}(\mathbf{r}) \equiv \psi_p(\mathbf{r}) = e^{ik_x x}e^{ik_z z} \qquad (85)$$

Any component of the plane wave momentum in the z direction does not contribute to the interference pattern. The interference is constructed by evaluating the superposition of the two waves at $z = 0$:

$$I_{holo} = \frac{1}{4}|\psi_l + \psi_p|^2, \qquad (86)$$

which is particular to the beam of interest. The prefactor is chosen to produce a pattern which oscillates between 0 and 1. For the phase vortex, the characteristic pattern is an edge dislocation, with $l + 1$ edges - also known as a fork dislocation. The interference pattern may then be binarised by clipping the pattern, for example

$$I_{\text{holo}}^{bi}(\rho, \phi) = \begin{cases} 1 & I_{holo} \geq 0.5, \quad \rho \leq R_{\max} \\ 0 & I_{holo} < 0.5, \quad \rho > R_{\max} \end{cases} \qquad (87)$$

for a maximum aperture radius $R_{\max}$. A similar process has been followed to produce holographic masks using Bessel or Laguerre-Gaussian vortex functions (Clark *et al.*, 2012). Despite the very different radial structures of the Bessel, Laguerre-Gaussian or the simple vortex beam of Eq. 84, the resulting binarised holographic masks are very similar (Clark *et al.*, 2012), indicating the binarisation primary picks out the strong intensity variation due to the phase variation and 'irons out' the more subtle amplitude variation of the different types of vortex modes.

The binary masks for an $l = 1$ and an $l = 3$ Bessel beam are displayed in Fig. 12, showing the corresponding $l + 1$ edge dislocations. Such a mask pattern is then embedded into something opaque to the radiation of interest - a printed film (Heckenberg *et al.*, 1992a,b) or a spatial light modulator (Yao and Padgett, 2011) for optical beams, or, in the case of electron beams, a FIB etched metal or silicon nitride film (McMorran *et al.*, 2011; Verbeeck *et al.*, 2010) - and placed into the path of the incident beam. Diffraction of the beam through the mask produces the desired vortex beams.

The far-field diffraction pattern resulting from the transmission of a plane wave through a CGH mask is given by the Fourier transform of the mask. This produces a non-diffracted zero-order beam, along with a series of vortex beams and their complex conjugates. From ordinary diffraction grating theory, we know that even
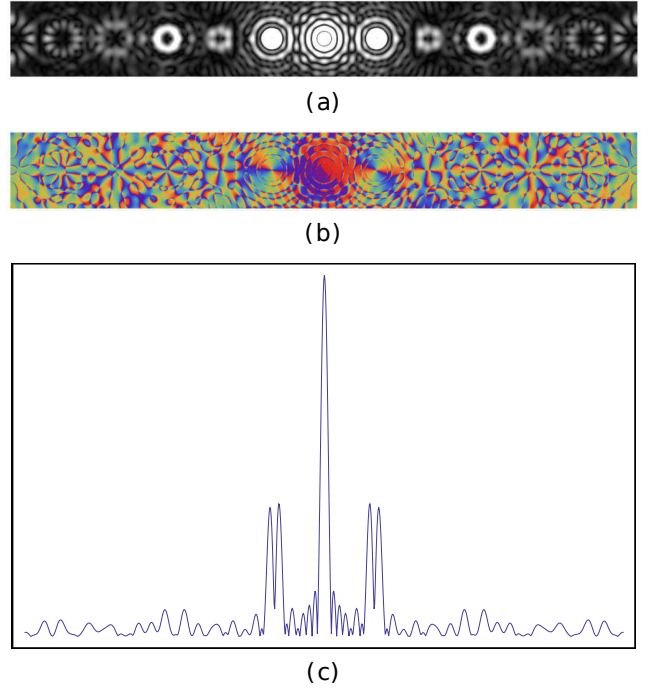

(a)

(b)

(c)

FIG. 13: (Color online) The far field diffraction pattern and phase distribution of the binary CGH amplitude mask to produce ($l = 1$, $p = 1$) FT-TBB beams shown in Fig. 7. (a) shows the diffracted beams, with several diffraction orders present; high intensity is indicated by white, zero by black. The phase of the beams is shown in (b), the opposite phase of the two sets of sidebands can be seen, with the nth order beams displaying a phase change of $2\pi n$. The rainbow scale indicates phase change from 0 (red) to 2π (purple). (c) shows the intensity of the various vortex beams. The central minima of all the diffracting beams are clear in the intensity patterns.

harmonics will be absent if the widths of the masked grating elements is half of their spacing (Born *et al.*, 1997). When this condition is only approximately satisfied, a common occurrence for many binary amplitude masks, the odd order diffraction beams are usually more intense than the even order beams, an example for the diffraction of a binary amplitude CGH mask is shown in Fig. 13.

A characteristic feature of the binarisation process is to introduce higher diffraction orders, generated from the step edge approximation to the sinusoidal transmission variation expected from the straightforward superposition of the vortex and the reference waves. This allows for the generation of higher order vortex beams than those encoding the original interference pattern, due to the inclusion of the high order harmonics of the original superposition in the binary holographic mask. Taking advantage of this mechanism, very high orders of orbital angular momentum have been demonstrated in electron beams - using a CGH mask designed for $l = 25$ beams, vortices having $l = 100$ have been demonstrated (McMorran *et al.*, 2011). Naturally, these higher order diffracted

beams are significantly less intense than the first order beams. Recently, it has been shown that an electron vortex beam of winding number $l = 200$ can be generated from the first order diffraction peak (Grillo *et al.*, 2015).

The CGH mask itself is not chiral, and so, unlike a phase plate, cannot impart orbital angular momentum to the transmitted beam by directly modulating the phase of the wavefront. Instead, the mask decomposes the input plane wave into a set of left- and right-handed vortices, so that the vanishing total orbital angular momentum of the incident wave is conserved (and so the mask may also act as a mode analyser (Saitoh *et al.*, 2012)). The various diffraction orders propagate from the mask at some angle ϕ_s to the optical axis of the incident beam, so that in the far-field different vortex beams are angularly separated. The magnitude of the transverse wave-vector of the reference wave, k_x, relative to the longitudinal wave-vector, k_z, determines the angles at which the diffracted beams exit the hologram, such that a large k_x increases the angular separation between the different diffracted orders (Heckenberg *et al.*, 1992a; McMorran *et al.*, 2011). The angle of the first order diffracted beam, for a Bessel vortex beam, is

$$\phi_s = \frac{\lambda}{d} = \frac{k_x}{k_z} \tag{88}$$

for grating separation d, which is related inversely to k_x. The nth order diffracted beam emerges at an angle $n\phi_s$ while the zero-order beam propagates along the original direction of the incident wave. A particular diffraction order of interest may be realigned to this optical axis by illuminating the hologram with a beam with transverse momentum nk_x (Schattschneider *et al.*, 2012b). The transverse momentum of the vortex beam itself $k_\perp$ is determined by the size of the mask aperture; for the Bessel beam we have

$$k_\perp = \frac{\lambda_{1l}}{R_{\max}} \tag{89}$$

with $\lambda_{1l} \approx 3.81$ the first zero of the Bessel function $J_l(x)$. A similar relationship applies for other vortex beams. For example, in the case of the Laguerre-Gaussian modes, λ_{1l} is replaced by the relevant radius of the Laguerre-Gaussian mode at $z = 0$.

In a binary hologram, the phase information is encoded as a lateral shift of the interference fringes, suggesting that the phase structure of the vortex beam can be recovered whatever the shape of the fringe (Clark *et al.*, 2012).

CGH masks are much more versatile and controllable than spiral phase plates as described in section IV.A. Each diffraction order is a pure phase vortex of strength nl as each is a unique vortex 'harmonic' of the incident vortex beam with orbital angular momentum of integer order $l\hbar$. The CGH masks may be constructed out of materials that are resistant to beam damage, and will have a longer useful lifetime than a spiral phase plate constructed of graphite thin films - in addition the results are directly reproducible, and in principle any order of orbital angular momentum may be specified, as demonstrated by the production of electron vortex beams with high values of orbital angular momentum (McMorran *et al.*, 2011). On the other hand, it should be noted that the binary CGH mask itself will block much of the incoming beam, so that only $\sim 50\%$ of the incident intensity is transmitted. Approximately 25% of the incident intensity is channeled into the zero order beam, with the higher order beam decreasing in intensity. The first order diffracted beams share $\sim 12\%$ of the incident intensity, which is not sufficient for many experimental applications.

Forked apertures as described above have been used to generate electron vortices in transmission electron microscopes (TEM) (McMorran *et al.*, 2011; Schattschneider *et al.*, 2012b; Verbeeck *et al.*, 2011a, 2010), and are now a standard technique in experimental electron vortex physics. The first proof-of-principle demonstration involved a 5 μm diameter CGH mask cut from platinum foil, with a single fork dislocation generating left and right handed vortex beams. The second instance of this holographic vortex generation involved silicon nitride films milled with very high resolution features (McMorran *et al.*, 2011); the high resolution milling allowed for the cutting of a narrowly spaced grating-like linear patterns, so that the diffracting beams produced had a large angular separation. The high resolution milling also enabled the fine features of holographic masks for generating vortex beams of higher order to be accurately reproduced. A forked mask encoding a vortex beam with a topological charge $l = 25$ was demonstrated. For structural stability of this fine featured CGH mask, the edge dislocation is not reproduced within the central region. However, leaving a solid block at the very centre of the mask did not seem to significantly impair the function of the mask, and vortices with clear central dark cores were produced with the fourth order diffracted beam carrying $100\hbar$ orbital angular momentum (McMorran *et al.*, 2011), demonstrating the versatility of the uses of binary CGH masks over spiral phase plates.

The phase structure and vorticity of the resulting beams were confirmed by observation of the forked interference fringes (McMorran *et al.*, 2011; Verbeeck *et al.*, 2010), and by the persistence of the axial dark core of the vortex on propagation and diffraction (McMorran *et al.*, 2011). A beam that simply has an annular profile will spread radially both inwards and outwards, obliterating the central zero intensity away from the focal point, whereas a beam with a phase singularity must preserve this singularity, as the orbital angular momentum must be conserved.
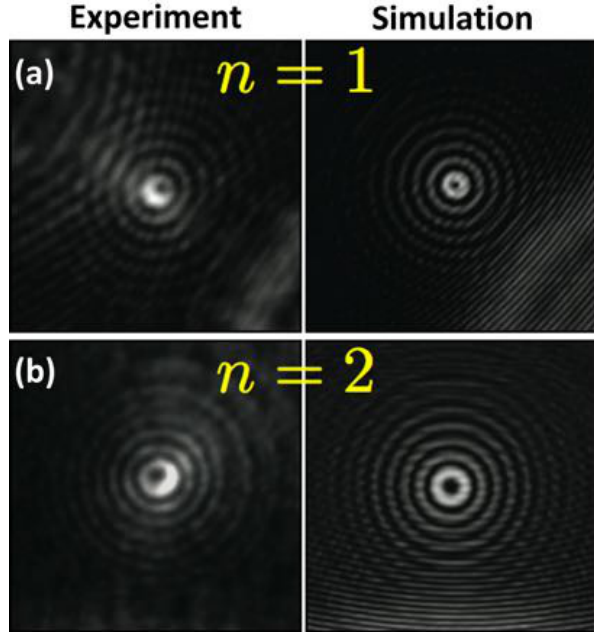
FIG. 14: (Color online) Comparison of the theory and the simulation of the non-zero order approximate Bessel type electron vortex beam. The topological order of the beams are denoted by n, which is identical to the l defined in this review. Image adapted from Fig. 4 of Grillo *et al.* (2014b).

2. Binary phase mask

The binarised CGH masks discussed above rely on the amplitude modulation of the transmitted wave in order to separate the orbital angular momentum components. Diffraction can also occur through a phase modulating CGH grating (Grillo *et al.*, 2014b; Harvey *et al.*, 2014) and offers an alternative method for the generation of vortex beams.

As in the case of the phase plate technology, a phase CGH mask can be produced by imprinting the desired phase change into a silicon nitride film with the thickness variation given by:

$$\Delta\phi(\rho,\phi) = CU\Delta t(\rho,\phi) \tag{90}$$

where C is a coefficient determined by the energy of the electron beam and U is the mean inner potential as defined in the context of Eq.81. The advantages of the phase grating technique are the increased control over the radial structure of the vortex beam and that it could potentially enable higher intensities to be transmitted into desired orders.

As a demonstration of the control of the radial structure of the vortex beams, Grillo *et al.* (2014b) were able to demonstrate approximate non-diffracting and self-healing electron Bessel beams over a range of 0.4 m (compared with 0.16 m for a conventional electron beam with the same spot size). This was done by encoding the fol-

lowing phase modulation into a phase mask:

$$\Delta\phi_l(\rho,\phi) = \Delta\phi_0 \mathrm{sgn}\left[\cos\left(k_\perp\rho + l\phi + \frac{2\pi}{d}\rho\cos\phi\right)\right] \tag{91}$$

where $\Delta\phi_0$ and d are the maximum size of the phase modulation and the wavelength of the reference plane wave used respectively and other symbols have the meaning defined in Eq.14 . Fig. 14 shows two kinds of non-zero order beams representing approximate vortex Bessel beams. The multiple ring structure seen is a characteristic of the electron probability distribution of the Bessel beam. The non-diffracting nature of the Bessel beam has been observed both in the optical (McGloin and Dholakia, 2005) and now also in the electron Bessel beams (Grillo *et al.*, 2014b).

The non-diffractive nature of the Electron Bessel beams might be particularly useful in electron tomography (Midgley and Dunin-Borkowski, 2009), where it can enable different planes within a material to be imaged with the same resolution, without the need to correct for the focus.

As almost all the electrons are transmitted through the phase holographic mask, the efficiency of vortex beam generation is expected to be higher than that of the amplitude holographic mask. For an ideal binary phase holographic mask, the power of diffracted electrons at the first order of diffraction can reach up to approximately 40% of the incident beam (Magnusson and Gaylord, 1978), which is about 4 times higher than that generated by the amplitude holograms. However, the pattern generated in the FIB turns into an approximate sinusoidal form, and thus the efficiency of the generated beam is approximately 17% smaller than an ideal binary profile (40%) with the same size of the thickness variation (Grillo *et al.*, 2014b; Harvey *et al.*, 2014).

3. Blazed phase mask

The increase in efficiency is an important goal for electron vortex beam generation (Yuan, 2014), since significant improvements in vortex beam brightness are required for the various applications currently being pursued. Using a blazed grating approach, Grillo *et al.* demonstrated increased transmission of 25% intensity into the $l = 1$ vortex mode. As before, the specific pattern to be milled is the characteristic forked pattern - however with the introduction of blazing to the grating pattern, a higher intensity may be projected into the desired mode. As can be seen in Fig. 15 the mask fabricated by Grillo *et al.* (2014a) was a good approximation to a perfectly blazed grating, and as such the results show a significant intensity decrease in the zero-order $l = 0$ vortex, with substantial increase in the first order beam with
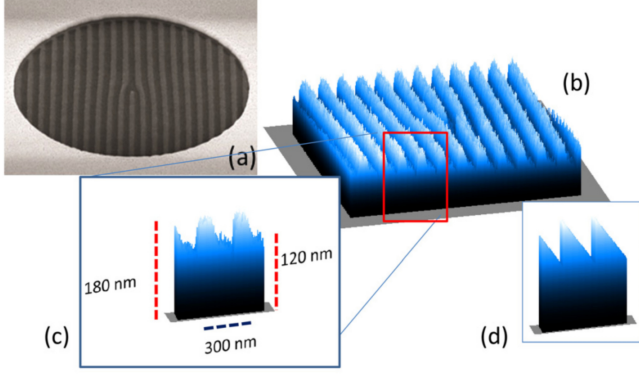
FIG. 15: (Color online) The blazed phase grating as demonstrated in (Grillo *et al.*, 2014a). (a) shows an SEM image of the mask, with electron-energy-loss measured thickness profile in (b). (c) shows typical heights of the grating maxima and minima, with an ideal blazed profile in (d) for comparison. Image adapted from Grillo *et al.* (2014a).

$l = 1$; the intensity distribution of the diffraction orders is now strongly asymmetric.

Nevertheless, one fundamental issue with this phase hologram approach is the inevitable energy spread that will arise within the beam, due to the inelastic scattering of electrons as they pass through the mask. For certain applications this will not be a problem as the inelastically scattered components of the electron beam can be removed by energy filtering. However, for applications such as spectroscopy, this may result in unacceptable loss of intensity and the presence of inelastically scattered components. In such instances, the use of a purely phase shifting device - such as those using electron optics alone - will be required.

It is worth noting that the theoretical maximum efficiency for an ideal blazed phase holograms is 100% in optics. As no absorption and scattering are involved, this value refers both to absolute efficiency and relative transmitted efficiency in optics (Grillo *et al.*, 2014a). In the context of refractive-material-based blazed gratings for electron vortex beam generation, the absolute generation efficiency will be limited by the inevitable large angle elastic scattering and incoherence due to inelastic scattering processes. As a result, the absolute efficiency is much lower than the relative transmission efficiency for the electron vortex case. At the time of writing of this review, the best transmission efficiency reported by Grillo et al (Grillo *et al.*, 2016) is 37% out of a theoretical limit of 38% for their partially blazed phase mask. On the other hand, McMorran's group (McMorran *et al.*, 2017) reported a much larger value of 70% for the absolute transmission efficiency for their blazed mask. Clearly more work is needed to investigate the practical limits to the generation efficiencies using optimized blazed phase masks.

4. Choice of reference waves

The holographic mask production techniques outlined above may also be applied with different reference waves. Another common choice in optics is a wave with a spherical wavefront (Heckenberg *et al.*, 1992a; Kotlyar *et al.*, 2006), sharing an axis with the desired mode. This also produces a characteristic interference pattern, a spiral with l arms, as shown for the $l = 1$ and $l = 3$ vortices in Fig. 16, alongside the corresponding binarised mask. The action of these holographic masks on an incident plane wave is very similar to that described above for the forked mask, however instead of the beams being separated by an angle, they are separated along the propagation direction. For the $l = 0$ non-vortex beam, the use of a spherical reference wave of curvature $1/f$ results in the familiar Fresnel zone plate, as shown in Fig. 16a and Fig. 16d. The vortex and zero-order modes transmitted through the spiral hologram produced using this reference spherical wave focuses at different points separated by a distance f (Heckenberg *et al.*, 1992b; Verbeeck *et al.*, 2012) - when the beam as a whole is properly focused by an electron lens, the zero-order beam will be in the focal plane of the electron lens, while the first order diffracted beams are focused at a distance f in front and behind the focal plane of the electron lens. For electron microscopy, this has the advantage that over- or under-focusing the beam enables the different vortices to be brought into focus onto the focal plane, where they may then be utilised with minimum involvement from the other orders in the beam (Verbeeck *et al.*, 2012). Unlike the forked masks, these under- or over-focused vortex beams should be useful for scanning electron microscopy; although the additional vortex modes will lead to a background contribution, reducing the signal to noise ratio of the vortex mode in focus.

The use of a spiral holographic mask has been demonstrated for electron vortices of various topological charges (Saitoh *et al.*, 2012; Verbeeck *et al.*, 2012). As with the high order forked mask of Ref. (McMorran *et al.*, 2011), the stability of the mask structure requires a reinforced (Saitoh *et al.*, 2012) centre or supporting struts (Verbeeck *et al.*, 2012); it was found in both simulations and experiments that the supporting struts did not significantly impair the integrity of the vortices produced (Verbeeck *et al.*, 2012). However, one issue with the application of a spiral mask is that the coaxial presence of the different diffraction orders leads to a relatively large background signal, causing the intensity of the centre of the vortex to be increased from zero (Verbeeck *et al.*, 2012). In order to reduce this overlapping effect as much as possible, the focal length of the corresponding Fresnel zone plate must be very long. A long focal length f means the arms of the spiral would decrease in separation rapidly towards the edge of the aperture. This requires very fine features in the holographic mask, a requirement similar to the
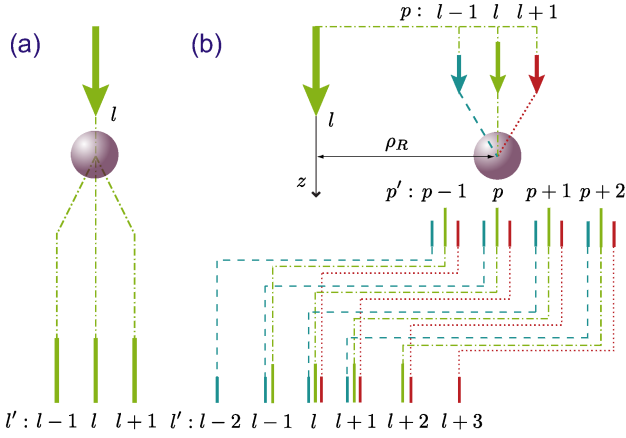
FIG. 16: Spiral interference patterns and masks of vortices interfering with spherical waves. (a) The in-plane intensity pattern for a non-vortex beam interfering with an outward propagating spherical wave; binarisation of this intensity pattern, forming a Fresnel zone plate, is shown in (d). (b) and (e) show the continuous and binarised interference patterns respectively for an $l = 1$ vortex beam interfering with the spherical wave. (c) and (f) show the same for the $l = 3$ vortex beam.

case involving a large k_x giving a high diffraction angle ϕ_s and decreasing the grating separation Eq. 89 in the dislocated grating mask. Additionally a highly coherent beam with a large convergence angle is required, stretching the limits of current microscope and FIB technology.

C. Electron optics methods

Material based electron optics is not flexible, requiring a specific mask for a single type of beam generation, and is also highly inefficient, as noted above. In general, modern electron microscopy avoids the use of such elements, instead relying almost exclusively on carefully controlled electrostatic and magnetic interactions to control the trajectory of the electron beams. With the exception of apertures, the shaping of the electron beam is in general accomplished by purely phase-transforming devices.

Modern aberration-corrected electron microscopy already has many multiple lenses in addition to the standard round lens (Rose, 2008). These existing multiple lens systems have been exploited to generate a structured phase shift to covert a non-vortex beam into a beam containing electron vortices, with the promise of high efficiency (Clark *et al.*, 2013). In addition, the lens aberration itself has also been used by Petersen et al., (Petersen *et al.*, 2013) to show that electron diffraction catastrophes can be created in this way, containing arrays of intensity zeros threading vortex cores.

1. Spin to orbital angular momentum conversion

One possibility is the generation of electron vortices from spin-polarised electron beams using q-filters, in analogy with the q-plates of optics. So called 'q-plates' have been available in optics since 2006 and have found applications in quantum information - these devices are based on patterned liquid crystal (LC) filters which allow conversion of spin polarised optical beams to oppositely spin-polarised vortex beams (Marrucci *et al.*, 2012, 2006). The action of the q-plate is based on the birefringent action of the LC which is also inhomogeneously patterned, such that spin and orbital angular momenta are exchanged between the beam and the LC. The LC thickness and patterning may be tuned in such a way as to facilitate the transfer of the spin and angular momentum of the beam, such that changes of spin angular momentum (SAM) by 2 are accompanied by a change in OAM of $-2q$, where q refers to the order of the singular defect of the patterning of LC optic axis. Other, more complex LC patterning may also be utilised to produce vector beams with specific polarisation profiles (Cardano *et al.*, 2012).

In an electron spin-to-orbital angular momentum conversion device the conversion effect is produced by the action of a spatially varying magnetic field on the beam over a specifically matched length, inducing a spatially dependent geometric (Berry) phase (Karimi *et al.*, 2012). Such a device takes the form of a spatially inhomogeneous Wien filter, with the trajectory altering action of the magnetic field balanced by the presence of an orthogonal electric field with the same spatial inhomogeneity. As with the LC filter, the multipolar fields of the electron q-filters also contain a topological defect (a field zero) at the centre, the order of which determines the value of q. Quadrupole fields give a q value of -1, for hexapole fields $q = -2$, and so forth. The filter is most effective for annular beams, so that it is more efficient to add or subtract q units of orbital angular momentum from a vortex beam (for example, for discrimination between different vortex modes) rather than create a vortex beam from a Gaussian or other non-vortex beam.

On transmission through the q-filter a precession of the electron spin is induced by the magnetic field. This is accompanied by a position-dependent geometric (Berry) phase shift, which is the source of the orbital angular momentum of the resulting beam (Karimi *et al.*, 2012). The two spin components of the electron beams are oppositely affected, so that the resulting beam is in a mixed states having orbital angular momentum $l \pm q$ and spin angular momentum $\mp 1/2$ (Schattschneider *et al.*, 2017). Since high brightness spin-polarised electron beams are not currently available, the q-filter is not viable as a method of generating useful electron vortices - however, conversely the q-filter may be used with $l = \pm 1$ vortex beam and appropriate apertures and OAM sorters to

obtain non-vortex spin-polarised electron probes for various applications (Grillo *et al.*, 2013; Karimi *et al.*, 2012, 2014).

2. Magnetic monopole field

The field distribution of a magnetic monopole would provide the ideal phase shift to convert a plane wave into a vortex beam (Wu and Yang, 1976). Such a monopole field has been considered for use in electron microscopy as early as 1992 (Kruit and Lenc, 1992). In the absence of such monopoles, the edge fields of a suitable thin wire magnetised along its long axis have been shown to induce a phase ramp around the beam that approaches 2π (Béché *et al.*, 2013; Blackburn and Loudon, 2014), opening the possibility of producing high-intensity vortex beams, in addition to improvements in phase contrast imaging. This method is potentially versatile, since the phase change of the beam depends on the magnetic flux contained within the needle, so that higher and non-integer vortex states may also be created (Blackburn and Loudon, 2014). When such a needle is placed in the middle of the aperture for the vortex forming lens, over 90% incident beam can be converted (Béché *et al.*, 2016). This high efficiency is a very useful property for many applications. This method also has the distinct feature to be independent of the energy of the electron beam, making it a potential avenue for producing ultrashort pulsed electron vortex beams. The main challenges in the use of monopole-like fields to create vortices will be the control of the fields themselves - the field geometry and strength are significantly affected by the thickness, width and magnetisation of the needle. Slight artifacts of the fabrication process may substantially affect the shape of the fields, as discussed in detail in (Blackburn and Loudon, 2014), resulting in some mixing of different vortex states (Béché *et al.*, 2016).

3. Vortex lattices

Vortices were originally described as screw-type dislocations in wave fields produced by the interference of three or more plane waves (Nye and Berry, 1974). In electron holography (Tonomura, 1987), electrostatic biprisms have been used to split the wavefront of a plane wave into two tilted plane waves which are deflected towards each other to produce standing wave patterns in the overlap region. By using two electrostatic prisms, we can obtain two overlapping standing waves. The crossings of the nodal lines in the standing waves are locations of vortices which form a regular array. Both square and triangular arrays of vortices are produced in this manner by adjusting the relative angles of the two sets of standing waves (Dwyer *et al.*, 2015; Niermann *et al.*, 2014). Such

lattices will have a pattern of vortices and anti-vortices regularly arranged, with locally varying orbital angular momentum density. In the square lattice, the resulting wavefront contains an array of dark spots; phase singularities of topological strength $|l| = 1$ with phase circulation alternately left- or right-handed about adjacent cores. In practice, due to position dependent phase shifting aberrations within the electron lenses or that caused by the sample, there is an overall shift in the position of the vortex cores across the array. This effect can be used to map out the phase shift in the electron-optical systems or that caused by the sample. Regular vortex arrays may also find applications in spectroscopy, so that the analysis might be performed simultaneously over a larger region of the sample, while reducing the average distance between the vortex lines and the atoms, and thus the off-axis contributions (see section VI.A below) (Niermann *et al.*, 2014).

A more complex form of interference of waves is that which causes diffraction catastrophes and caustics, which can also lead to formation of vortex arrays (Nye, 2006; Petersen *et al.*, 2013). A lattice of vortex-antivortex pairs has been shown to surround the caustics formed from both astigmatic and coma induced diffraction catastrophes in the electron microscope, along with the existence of additional vortices inside the caustic. The wave fields of such caustics present the opportunity to study complex vortex behaviors, with twisted vortex trajectories and loops being apparent (Petersen *et al.*, 2013).

D. Hybrid method

1. Lens aberrations

Clark *et al.* used electron optical aberration to generate an azimuthal phase ramp at the back-focal plane to produce an isolated electron vortex beam (Clark *et al.*, 2013). Comparison of the aberration correction series and the Fourier series of the vortex phase shows that a good approximation to the vortex phase ramp can be made by minimising all aberrations except for the various orders of astigmatism. Matching the astigmatism to the desired phase shifts and applying an annular aperture to ensure beam passage through the relevant regions of the lens and corrector allow for the appropriate phase ramp to be created (Clark *et al.*, 2013). The beam generated experimentally using such a set up was demonstrated to be a good approximation to the $l = 1$ vortex mode, exhibiting the axial minimum and the 0 to 2π phase variation. The modal decomposition showed that only 32% of the transmitted beam was in the $l = 1$ vortex mode. However, the presence of other vortex modes, and the clear spatial asymmetry of the beam demonstrate that the beam produced is not as pure as that created with holographic masks (Clark *et al.*, 2013). On the other

hand, the intensity of the vortex generated is approximately twice that achieved using the amplitude binary holographic mask technique; this method is more efficient for the generation of the $|l| = 1$ vortex mode, however the generation of higher order vortices may prove to be much more challenging due to the significantly steeper phase ramp required.

2. Electron vortex mode converter

A mode converter for electron beams has been described (Schattschneider *et al.*, 2012a), acting in an analogous way to laser mode converters in optics (Beijersbergen *et al.*, 1993). The electron vortex implementation involves making use of astigmatic correctors specific to the electron microscope, as well as the use of a Hilbert phase plate. This is therefore a hybrid technique encompassing the phase plate and electron optics approaches discussed above.

The Laguerre-Gaussian vortex mode may be described as a linear superposition of two Hermite-Gaussian modes with a phase difference of $\pi/2$. The Hermite-Gaussian modes do not themselves carry orbital angular momentum, however by exploiting the difference in Gouy phase for astigmatic Hermite-Gaussian modes, such a superposition can be produced, resulting in a Laguerre-Gaussian mode with well defined orbital angular momentum and phase singularity (Beijersbergen *et al.*, 1993). The experimental procedure for electron vortices described by Schattschneider *et al.* (2012a) relies on a lens with variable astigmatism, so that the focal points of the x and y transverse parameters may be set independently. This may then be used to generate a Laguerre-Gaussian mode from a Hermite-Gaussian mode. An approximation to a Hermite-Gaussian mode has been generated using a Hilbert phase plate (Danev *et al.*, 2002), which imparts a phase-shift of π between the two halves of the beam, similar to the phase difference of π between the two lobes of the Hermite-Gaussian mode. The Hermite-Gaussian mode is then passed through the astigmatic converter, oriented at $45°$ to the transverse axes of the astigmatic converter, so that the astigmatism acts on the two x and y components. The foci of the astigmatic lens are set so that a relative Gouy phase difference are created between the two transverse profiles in the back focal plane to obtain a Laguerre-Gaussian beam profile (Schattschneider *et al.*, 2012a).

A proof-of-principle experimental result has been demonstrated, however although a phase singularity is apparent at the centre of the back focal plane, the resulting profile does not have rotational symmetry, and so is not a pure Laguerre-Gaussian mode. The discrepancy from the simulated results arises due to defocus and, importantly, strong beam absorption in transmission through the Hilbert phase plate (Schattschneider *et al.*, 2012a). Nevertheless, the electron vortex mode converter is an attractive prospect if these effects can be overcome, as it enables the generation of electron vortices of high intensity, of up to 90% of the incident plane wave intensity, as opposed to $\approx 6\%$ using the holographic masks.

V. VORTEX BEAM ANALYSIS

Any study of the electron vortex beam will inevitably involve some characterisation of its properties. This will also be useful in, for example, examining transfer of orbital angular momentum in experiments involving interactions with various forms of matter and light. We now briefly review the techniques that have been developed for electron vortex beam analysis.

A. Interferometry

The simplest approach is to examine the intensity profile of the beam cross-section. For a given point in the wavefront in a vortex beam, the existence of the conjugate point with antisymmetry in phase ensures that their coherent superposition on the beam axis will always lead to destructive interference. This is responsible for the persistence of the central dark spot in the vortex beam. Thus the observation of the doughnut ring in the beam cross-section is taken to be a signature of a non-zero topological charge. However we also need to know the sign and the magnitude of the topological charge and the radial structure. For example, the radial structure of the Laguerre-Gaussian beam is specified by the radial index p in Eq. 9. As for the identification of the pure OAM states, some progress has been made, as we summarise below.

1. Electron holography

The interference of a pure vortex beam with a plane reference wave results in a forked interference fringe, a property that is fundamental to the holographic mask technology introduced in section IV.B. The interference experiment can be performed in an electron microscope equipped with an electron biprism (Tonomura, 1987). A biprism is usually a positively charged wire. Two half of the wavefront on either sides of the charged wire will experience transverse shear because the negatively charged electrons will be attracted towards the positively charged wire. The resulting overlap of the wavefronts forms holographic fringes. If only a parallel beam falls onto the regions containing the charged wire, linear grating-like interference structure will be observed. In traditional electron holography, a sample is inserted in the path of one half of the split wavefront so that the extra phase

and amplitude modification can be recorded as the additional shift of the fringe as well as the modulation of the fringe contrast. In vortex beam analysis, the sample may be replaced by a vortex converter such as a spiral phase plate or an holographic diffraction mask. The vortex phase structure imprint on the interference fringes is a dislocation or a fork structure, such that the number of the forks in the interference pattern is equal to the magnitude of the topological charge and the orientation of the fork can be related to the sign of the topological charge of the beam. This electron holographic method was used by Uchida and Tonomura (2010) to demonstrate for the first time the phase structure of an electron vortex beam.

2. Knife-edge and triangle aperture diffractive interferometry

Electron holography using the electron biprisim technique is only available in specialised microscopes, so alternative methods had to be developed. The simplest holography method without the use of electronic biprism is the knife-edge holography method. This creates a reference waves by utilising the beam-bending effect associated with the Fresnel-diffraction of electrons from the edge of an aperture. Verbeeck et al. (2010) used this to demonstrate the production of vortex beams by a holographic mask.

A useful variation of this method is the use of a triangular aperture. The interference of the Fresnel fringes from three neighbouring edges of the triangle results in a triangular lattice structure which depends strongly on the topological charge of the vortex beam (Hickmann et al., 2010). It is then a simple matter to count the number of spots in the resulting interference pattern to determine the topological charge.

It is to be noted that the above-mentioned methods only work in out-of-focus conditions.

3. Diffraction

The phase structure of the vortex beam can also be studied by the diffraction method. A hologram mask can be used to determine the topological charge of the beam (Guzzinati et al., 2014; Saitoh et al., 2013). In this method, a forked grating structure, formed from the interference of a plane wave and a vortex wave of topological charge of $l_{grating}$, is used as a beam analyser. The vortex beam is diffracted by the grating structure and far field diffraction pattern is examined. The diffraction of the dislocated grating adds $n * l_{grating}$ to the topological charge of the resulting diffracted beams, where n is the order of the diffraction and takes the values of $0, \pm 1, \pm 2$, etc. The total topological charge of the diffracted beams is now given by:

$$m = nl_{grating} + l \qquad (92)$$

In particular, the diffracted beam with $m = 0$ has an intense central spot and so can be easily identified. This allows the OAM content of the incident beam to be easily determined using Eq. 92, if gratings with different topological charges are employed. Other methods such as the simple multiple pinhole plates have also been suggested, with the mixed results due to possible effects such as aliasing effects (Clark et al., 2014).

In general, the identification of the vortex beams of mixed orders is difficult. But Saitoh et al. (Saitoh et al., 2013) suggested that if a pin-hole aperture is also used on the diffracted beam, the vortex beam can be sorted into different components according to their topological charge.

B. Mode conversion analysis

One of the simplest methods is based on the mode conversion of Hermite-Gaussian modes to generate Laguerre-Gaussian ones (Allen et al., 1992; Courtial and Padgett, 1999). Here, the mode conversion is run in reverse and the vortex beam is decomposed into Hermite-Gaussian beams with characteristic modes. In optics this is achieved using cylindrical lens while in electron optics (Guzzinati et al., 2014; Shiloh et al., 2015) use is made of a astigmatism corrector which is readily available in a typical electron microscope. Obviously for higher order vortex beams, we might have mixed radial modes sharing the same OAM quantum number. This may result in a complex superposition of the pattern. Thus the method is probably more useful for vortex beams of small topological charges. The sign of the topological charge can be read out through the sense of the rotation of the resulting Hermite-Gaussian pattern because of the l-dependent Gouy rotation.

The approaches adopted so far can all be traced to original methods developed for characterising optical vortex beams and they work well for single pure OAM states. The challenge occurs when one has to deal with mixed OAM states. Optical approaches such as multipoint interferometers (Berkhout and Beijersbergen, 2008), geometric transformations by phase manipulation (Berkhout et al., 2010), and the use of multiple interferometers in a cascade set-up (Leach et al., 2004) are currently difficult to implement in the existing electron microscope set-up, so a new approach is required, especially for the characterisation in the single electron region. For practical reasons, the holographic diffraction mask and the aperture masking methods are difficult to implement for atomic size vortex beams, making the astigmatism transformation method currently the most realistic method for atomic scale pure vortex beams. For efficient sorting of electron vortex beams in general, electron optical are preferred and a refractive device has recently been proposed by McMorran et al. (2017).

C. Image rotation

Because of the azimuthal dependence of a pure vortex beam is encoded in the phase factor $e^{il\phi}$ independent of z, the cross-sectional image of any pure vortex beams is circularly symmetric so any potential rotation is not detectable. This method is therefore not suitable for the characterisation of the rotation of the pure states. On the other hand, the circular symmetry will be broken in a mixed state vortex beam, resulting in an asymmetrical cross-sectional beam intensity. This can be achieved by different methods, ranging from simply cutting a pure vortex beam by a knife-edge-like mask to create an asymmetrical cross-sectional distribution (Guzzinati *et al.*, 2014), to the careful preparation of a superposition of pure vortex beams (Greenshields *et al.*, 2012) or a vortex-endowed C-shaped beam (Mousley *et al.*, 2015). The rotation of the transverse image of the electron vortex beam can be measured as a function of the propagation distance or as a function of the magnetic field strength. In that way, measurements of the image rotation along the z-direction can be used to study the Zeeman or Gouy effects of the electron vortex beam (Schachinger *et al.*, 2015).

1. Gouy rotation

The Gouy phase is due to spatial confinement of the vortex beams near focus (Feng and Winful, 2001; Petersen *et al.*, 2014). In the absence of an external magnetic field or when the field strength is so small that the magnetic effect can be ignored to the first order, the main contribution to the image rotation is due to the variation of the Gouy phase difference between OAM beams with different topological charges. The Gouy phase difference changes rapidly near the beam waist, so that the Gouy rotation is most easily observed around the focus plane, as shown by Guzzinati *et al.* (2013).

2. Zeeman rotation

One of the consequence of using magnetic lens to focus electron beams is that all electron beam trajectories with transverse velocity components undergo Larmor precession. In electron microscopy, this results in the well known image rotation phenomenon (Reimer and Kohl, 2008). Early microscopists had to take this into account when comparing microscope images taken at different magnifications as the excitation of the magnetic field in the lens changes. In modern transmission microscopy, lens design is such that the rotation effect due to different lenses cancels out, so electron microscopists need not be concerned with such effect.

The presence of the external magnetic field also causes complex and interesting changes in the phase of the electron vortex beam as described in section III. However, for nanoscale vortex beams that are being generated inside electron microscopes where the saturated field strength is typically in the order of 2T, the effect of the magnetic field would be very weak (Babiker *et al.*, 2015). To see the magnetic field induced rotation, one has to go either to much stronger magnetic fields or vortex beams of large transverse structures. In general, such rotation should be accompanied by changes in the radial direction due to competition of the beam diffraction and the confining effects of the magnetic field (Greenshields *et al.*, 2012). In special cases, when the vortex beam has the characteristic beam width w_B given in Eq. 58, one can study the rotation of the Landau states given by Eq. 62.

These image rotations have been experimentally observed in the electron microscope, for both the balanced and unbalanced suppositions (Guzzinati *et al.*, 2013). The experimental situation differs from the theoretical treatments outlined above in that the fields are not uniform, and the beams have a well defined focal plane. As such, the action of the Zeeman and Gouy phase shifts both contribute, with the Gouy shifts dominating in the vicinity of the focus of the beam, due to the transverse confinement (Feng and Winful, 2001), and the Zeeman shift is more apparent at large radial distances from the beam axis, due to the magnetic fields of the lenses. For the unbalanced superposition, the difference between those states, with the net OAM aligned and anti-aligned with the direction of the magnetic field, is clearly shown in the net addition of the separated rotations due to the Zeeman and Gouy terms (Guzzinati *et al.*, 2013). Such Zeeman-Gouy phase effects may find applications in vortex beam analysis, since this offers a method by which oppositely oriented vortices may be differentiated, by the observation - or lack - of image rotations in known magnetic fields. For beams with a Landau state transverse mode given by Eq. 62, rotation either in Larmor, cyclotron (double-Larmor) or zero frequency have been observed (Schattschneider *et al.*, 2014b), consistent with the prediction of Bliokh and Nori (2012a). However, the use of the knife-edge resulted in the mode broadening due to an approximate uncertainty principle for angular position and angular momentum (Franke-Arnold *et al.*, 2004), so the measurement can not be taken for a vortex beam in a pure Landau state.

D. Vortex-vortex interactions and collisions

General considerations of vortex-vortex collisions have been discussed (Berry and Dennis, 2007, 2012; Bialynicki-Birula *et al.*, 2000, 2001) for the cases where there are two or more phase singularities present in the wave field. In such cases, the behavior of the vortices becomes somewhat complicated, with possible phenomena

including the creation, annihilation and crossing of vortex lines. For the electron vortex, experimental demonstrations of wavefields with two (Hasegawa *et al.*, 2013) or several (Niermann *et al.*, 2014) phase singularities have been achieved in the electron microscope. In the first case, a specially prepared holographic mask with two phase defects (edge dislocations) was used to embed two phase singularities into the resulting first order beams (Hasegawa *et al.*, 2013), while the second involved two orthogonally-acting biprisms arranged in such a manner as to generate a lattice of vortices through wave interference.

For the case when two vortices are present in the beam, the behaviour and interaction of the two vortices can be examined as the beam passes through focus. Holographic masks incorporating two edge defects were produced to generate two vortices of topological change $|l| = 1$ slightly displaced from one another - the two vortices may either be aligned or anti-aligned, in which case the behaviour as they propagate takes on a different character. For the case when the two vortices are aligned, they are found to precess about each other within the first order diffracted beams, whereas for the case when the vortices are anti-aligned the lines of phase singularity are attracted to each other, eventually annihilating. Both effects are attributed to the change in Gouy phase as the vortices pass through the focal point (Hasegawa *et al.*, 2013) - for the aligned beams the Gouy phase shift occurs in the same direction, so that the beam rotates in the same direction at the same rate, whereas the phase shift is opposite for the anti-aligned vortices, causing them to annihilate.

E. Factors affecting the size of the vortex beam

The possibility of using electron vortex beams to probe the properties of materials with atomic resolution requires the generation of atomic scale vortex beams with cross-sections in the Ångstrom scale. Sub-Ångstrom focused electron probes have been demonstrated and available more than a decade ago (Batson *et al.*, 2002). In a modern transmission electron microscope, a probe size as small as 0.5 Å can be achieved using a highly coherent source with a large convergence angle and corrective optics for the minimising of aberrations in the probe forming lens (Erni *et al.*, 2009). Can we replace the circular aperture with a top-hat like transmission function with azimuthal phase gradient to produce electron vortex beam, such as the beam defined in Section II.B.3, in the Ångstrom range? To answer this question, we need to first define what is meant by the size of non-vortex beams as well as that of vortex beams.

A simple estimate of the ring size of the single donut vortex beam can be obtained by considering the quantized orbital angular momentum of a circulating particle flux in a circle of radius ρ_l. We make use of the standard expression for the angular momentum $\mathbf{L} = \boldsymbol{\rho}_l \times \mathbf{p}$ and that the maximum size of the linear momentum transferred by the diffraction of electron beams passing through an aperture subtending a half angle α is equal to αk_0, where $\hbar k_0$ is the momentum of the electrons. The size of the donut ring is then approximately given by:

$$\rho_l \sim \frac{l\hbar}{\alpha \hbar k_0} = \frac{l\lambda}{2\pi\alpha} \tag{93}$$

For all the beams passing through such an aperture, the uncertainty principle also implies that the minimum beam size ($\Delta\rho$) due to diffractive broadening, is given by:

$$\Delta\rho \sim \frac{\hbar}{\Delta p} = \frac{\hbar}{\alpha \hbar k_0} \sim \frac{\lambda}{2\pi\alpha} \tag{94}$$

These order-of-magnitude estimates show that both ρ_l and $\Delta\rho$ are controlled by the convergence angle subtended by the lens aperture ($\alpha = R_{max}/f$) but for different physical reasons. To be more precise, one needs to know the exact electron wavefunctions because the spatial distributions of the electrons are known to be diffuse in space and vary for different types of vortex beams as reviewed in section II.B. For example, the size of the donut rings (ρ_l) in LG beams introduced in section II.B.1 scales with $\sqrt{l}$ (Lembessis and Babiker, 2016), but for bandwidth limited vortex beams produced by the Fraunhofer diffraction of a finite-radius plane waves impinging on a spiral phase plate (section II.B.3), the ring size scales with l (Curtis and Grier, 2003). For the FT-TBB discussed in section II.B.3, there is a non-linear dependence on l. On the other hand, the diffraction-limited width of an ideal non-vortex beam is given by the size of the Airy disk ($\Delta\rho = 1.22\lambda/\alpha$ (Airy, 1834)). Combining the two different effects an approximate empirical formula for the overall vortex beam size ($\tilde{\rho}_l$) emerges as (Curtis and Grier, 2003):

$$\tilde{\rho}_l = 2.585 \frac{\lambda f}{\pi R_{max}} \left(1 + \frac{l}{9.80}\right). \tag{95}$$

This suggests that the diffraction limited singly charged vortex beam size is only about 10% larger than the non-vortex beam. With a microscope capable of 0.5Å non-vortex beam, a singly charged vortex beam of sub-Ånstrom size should be possible.

Experimentally, most studied electron vortex beams can be effectively obtained as some forms of bandwidth-limited beams with wavefunction truncation by a hard aperture at the plane of the focusing lens (Béché *et al.*, 2016; Schattschneider *et al.*, 2012b; Verbeeck *et al.*, 2011a). The scalar diffraction theory of such a case has been thoroughly investigated in the course of optical vortex studies (Kotlyar *et al.*, 2005) and this compares favorably with the theoretical investigations when finite source size effects or even spherical aberration, is taken into account, where appropriate (Schattschneider *et al.*,
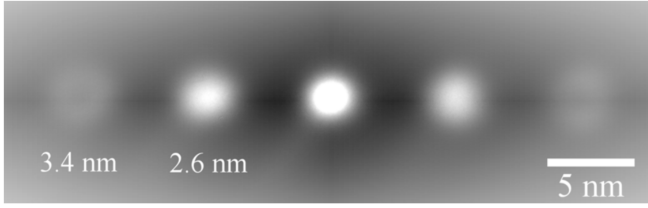
FIG. 17: Vortex probes at focus of the condenser lens of a JEOL 2200FS aberration corrected tranmission electron microscope operating at 200kV. The central spot is the image of the non-vortex beam, while the other spots are images of the diffracted vortex beams produced by a forked diffractive hologram with a binary pattern similar to that given in Fig. 12. Sizes of the 1st and 2nd vortex cores at FWHM are 2.6 nm and 3.4 nm, respectively. Due to incoherent effect, the intensity dip is only partially visible for the 2nd order vortex beam.

2012b). In situations where a small convergent beam is used (Schattschneider *et al.*, 2012b; Verbeeck *et al.*, 2011b), the ring diameter of the vortex beam can be accurately measured and the experimentally obtained values agree with those emerging from optical diffraction theory. For example, in a TEM with a round condenser aperture subtending a convergence angle of 21 mrad, the size of the Airy-pattern of the non-vortex beam is 1 Å using the Rayleigh resolution criterion for the case an electron vortex beam with $l = 1$ and a minimum full width at half maximum (FWHM) diameter of 1.2 Å. The reason that it is the FWHM that is used in this case instead of the ring size is the broadening effect of the spatial distribution due to the finite source size (incoherent broadening), estimated at 0.7 Å. Incoherent broadening effects, when these are significant, result in a less visible central dip of the vortex beam (for an example, see Fig. 17). Incoherent broadening plays an increasingly important role in atomic size electron vortex beam experiments as a size-limiting factor (Löfgren *et al.*, 2016), but its influence can be taken into account in the same manner as done routinely in describing focused non-vortex beams commonly used in scanning transmission electron microscopy (Kirkland, 2010). For an electron vortex beam generated inside a 300kV scanning transmission electron microscope a probe size of the order of 0.87 Å has been demonstrated (Béché *et al.*, 2016), invalidating the early too pessimistic prediction (Idrobo and Pennycook, 2011). As the current resolution of electron microscopes is not yet wavelength limited, there is still scope to reduce the vortex beam size further.

VI. INTERACTION WITH MATTER

The interaction of an electron vortex beam with single atoms has been considered (Lloyd *et al.*, 2012a,c; van Boxem *et al.*, 2015, 2014; Yuan *et al.*, 2013), as well as

Mott scattering (Serbo *et al.*, 2015) when the spin-orbit interaction is taken into account. The related radiative capture of a vortex electron by an ion has also been investigated (Matula *et al.*, 2014). We focus on chiral specific interactions in this section.

A. Chiral-specific spectroscopy

The practical generation of electron vortex beams was accompanied by the suggestion that such vortex probes might initiate, as a first application, a new type of electron energy loss spectroscopy (EELS) involving orbital angular momentum transfer (McMorran *et al.*, 2011; Uchida and Tonomura, 2010; Verbeeck *et al.*, 2010). The first experiment on EELS using electron vortex beams was reported by Verbeeck *et al.* (2010). In this experiment, a 50 nm thick Fe film was placed inside the field of the objective lens, such that it was magnetically saturated. A non-vortex beam was transmitted through the iron film and the transmitted beam then passed through a forked holographic mask at a slight defocus, such that the various orbital angular momentum components were separated into distinct vortex beams. Comparing the energy-loss spectra of the two first order transmitted vortex beams showed a dichroic effect in the iron L_2 and L_3 edges, understood to indicate a transfer of orbital angular momentum between the beam and the internal electronic states of the iron atoms. The electron vortex energy-loss spectrum corresponds well to similar X-ray magnetic circular dichroism (XMCD) spectra (Carra *et al.*, 1993; Thole *et al.*, 1992), so that the magnetisation of the sample is said to be clearly identified. However, since this 2010 result was reported there have been no further experimental reports of an observed magnetic dichroism, and there has been much discussion as to whether electron vortex beams could provide an advantage over existing methods in electron beam chiral dichroism spectroscopy. Nevertheless, a great deal of theoretical work has been carried out, uncovering the subtle physics involving orbital angular momentum transfer and the best conditions for its observation (Rusz and Bhowmick, 2013; Schattschneider *et al.*, 2014a; Yuan *et al.*, 2013).

Comparing the results of the iron dichroism experiment with the well known XMCD spectra of iron suggests that there is a similar transfer of orbital angular momentum between the beam electron and the internal atomic states, in contrast to the case of optical vortices, in which no orbital angular momentum transfer can arise in dipole transition (Andrews *et al.*, 2004; Babiker *et al.*, 2002; Jáuregui, 2004) (see also (Alexandrescu *et al.*, 2005)) nor any were observed (Araoka *et al.*, 2005; Giammanco *et al.*, 2017; Löffler *et al.*, 2011). The mechanisms of the atomic-vortex interactions are quite different in the optics and electron cases - in the optics case the interaction Hamiltonian arising from the minimal coupling prescrip-

tion does not exhibit the required chirality to mediate orbital angular momentum transfer, in contrast to the long-range Coulomb interaction between the atomic and vortex electrons (Lloyd et al., 2012a,c).

1. Matrix elements for OAM transfer

Writing the interaction Hamiltonian as the sum of the Coulomb interactions between the atomic constituents and the vortex electron, we have,

$$\mathcal{H}_{\text{int}} = -\frac{e^2}{4\pi\epsilon_0}\left(\frac{1}{|\mathbf{r}_v - \mathbf{R} + \frac{m_e}{M}\mathbf{q}|} - \frac{1}{|\mathbf{r}_v - \mathbf{R} + \frac{m_p}{M}\mathbf{q}|}\right) \tag{96}$$

where $M = m_p + m_e$ is the mass of the atom, and the relevant position vectors are shown in Fig. 18. This interaction Hamiltonian may now be expanded as a multipolar series and applied as a scattering perturbation to a set of initial and final states of the well-known hydrogenic wavefunctions and vortex wavefunctions to yield the selection rules of the interaction (Lloyd et al., 2012a,c). In the leading (dipole) order the transition matrix element is found to reduce to the following

$$\begin{aligned}\mathcal{M}_{fi} =\ & \frac{e^2}{4\pi\epsilon_0}\Big(\mathcal{C}_l^{+1}\delta_{[(L+l),(L'+l'+1)]}\delta_{m,m'-1}\ + \\ & \mathcal{C}_l^{-1}\delta_{[(L+l),(L'+l'-1)]}\delta_{m,m'+1}\ + \\ & \mathcal{C}_l^{0}\delta_{[(L+l),(L'+l')]}\delta_{m,m'}\Big).\end{aligned} \tag{97}$$

where the C_l's are complex functions of the internal coordinate $\mathbf{q}$ to the first order. The selection rules deducible from the matrix element show that in the dipole approximation a single unit of orbital angular momentum may be absorbed (released) by the atomic electron from (to) the combined orbital angular momentum of the electron vortex and atomic centre of mass. The combination of the vortex and centre of mass orbital angular momenta allows for the possibility of the rotation of the centre of mass, provided the atom is not fixed; which lays the foundations for the manipulation of larger particles though OAM exchange (Gnanavel et al., 2012; Verbeeck et al., 2013). Further analysis of the quadrupole and higher order interaction terms demonstrate similar selection rules in which zero, one or two units of orbital angular momentum may be transferred - higher order multipole terms of order n mediate the transfer of zero or n units of orbital angular momentum.

2. The effect of off-axis vortex beam excitation

In expanding the interaction Hamiltonian about the atomic centre of mass, the above analysis does not fully demonstrate the complications arising from the extrinsic nature of the vortex orbital angular momentum. It
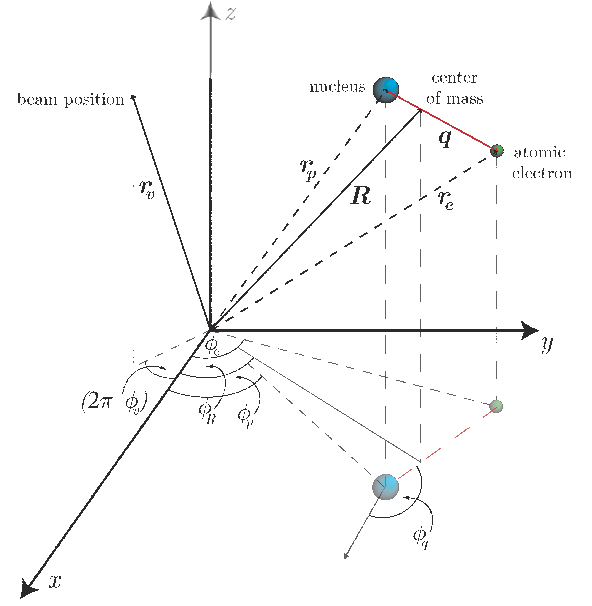

FIG. 18: (Color online) The atomic model system interacting with a vortex beam whose cylindrical axis is along the z-direction of the laboratory frame of reference. The vectors $\mathbf{r}_e, \mathbf{r}_p, \mathbf{R}$ and $\mathbf{q}$ refer, respectively, to the position vectors of the atomic electron, the nucleus, the centre of mass, the internal position relative to the centre of mass and the position variable of the vortex electron. The corresponding ϕ's represent the azimuthal angles and these are important for the description of the phase factors.

is illuminating to determine the modal expansion of the beam from the perspective of the atomic nucleus, and compute the weighted scattering amplitudes to the various possible transfer channels. The interaction Hamiltonian remains the same as that of Eq. 96, but now the initial and final vortex states have to be written as expansions about the centre of mass frame, rather than being given in the laboratory frame, as before. This is accomplished by use of the Bessel function addition theorem (Abramowitz and Stegun, 1972) (see the figure for the relevant notation)

$$\begin{aligned}J_l(k_\perp) =\ & e^{-il(\phi_v - \phi_n)}\times \\ & \sum_{p=-\infty}^{\infty} J_{l-p}(k_\perp\rho_n)J_p(k_\perp\rho_v')e^{i(l-p)\phi_n}e^{ip\phi_v'}.\end{aligned} \tag{98}$$

This results in the original vortex beam of topological charge l being described with respect to a new axis - the origin of which is common with the the atomic nucleus - in terms of an infinite series of Bessel functions $J_p(k_\perp\rho_v')$, with weighting functions given by $J_{l+p}(k_\perp\rho_n)$. Thus, the relative location of the atom with respect to the axis of the incident vortex beam determines the precise modes that the atomic electron 'sees' to interact with. For an atom situated directly on the beam axis, the original $p =$

l mode is the only contribution, since in this case only the weighting term $J_0(k_\perp \rho_n)$ is non-zero (also see the left panel of Fig.19). However, for an atom displaced from the beam axis, the next atom-centred vortex modes $p = l \pm 1$ become significant even at small distances, of the order of a fraction of the radius corresponding to the first Bessel function zero $\lambda_{11}/k_\perp \approx 0.1$ nm for $l = 1$, i.e. within the first ring of the Bessel beam. It is clear that slight displacement from the beam axis leads to the contributions of vortex modes with winding numbers different from the overall angular momentum quantum number of the beam l (also see the right panel of Fig.19). The expanded Bessel function may then be used to define an effective operator

$$\mathcal{O} = \langle \Psi'_f | \mathcal{H}_{\text{int}} | \Psi'_i \rangle \tag{99}$$

which determines the selection rules when applied to the atomic states, where $\Psi'_{i(f)}$ refers to the initial (final) wavefunction involving the expanded Bessel function of Eq. 98. Applying the Bessel addition theorem a second time allows for the expansion in terms of the in-plane dipole moment of the atom, making apparent the specific multipolar character of the transfer interaction (Yuan $et\ al.$, 2013).

When the atom is off axis, there are several available channels for atomic excitation, both in view of the multipolar nature and the specific Bessel mode of the expansion, as is illustrated in Fig. 19. It can be seen that, in contrast to the straightforward on-axis case, for an atom localised at an off-axis position the change in the orbital angular momentum of the beam does not necessarily indicate a corresponding change in the OAM of the internal dynamics of the atom. At first sight this would seem to present a large obstacle to the use of vortex beams to probe chiral information. However, after taking into account the relative intensities of the various interaction channels, one can show that for the dipole excitation case, the off-axis contributions are an order of magnitude smaller than the on-axis contribution, with intensity decaying rapidly further away from the axis, so that the principal transitions in any such chiral spectroscopy experiment are those having the XMCD-like selection rules of Eq. 97. Additionally, higher order multipole transitions will contribute to the background signal, but these are also found to be much smaller in magnitude compared to the dipole contribution, due to the much smaller overlap of the Bessel functions involved (Yuan $et\ al.$, 2013).

The off-axis contributions to an experimental electron-energy loss spectrum may be further reduced to produce an acceptable signal-to-noise ratio, by making use of a confocal TEM set-up, ensuring that the signal contributions come from those atoms lying on or very close to the microscope axis, and reducing the non-chiral signal from atoms displaced from the axis (Schattschneider $et\ al.$,
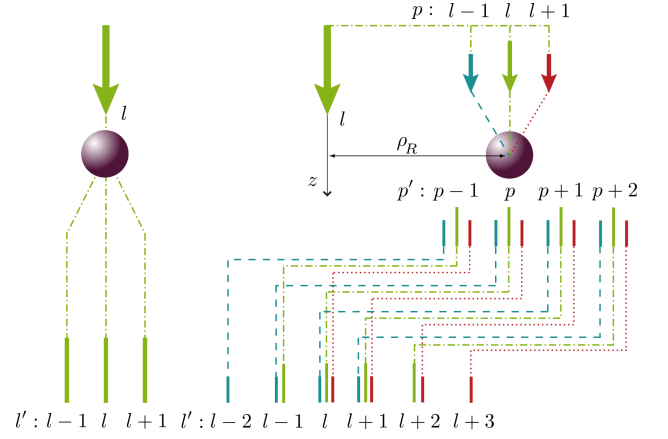

FIG. 19: (Color online) Illustration of the various interaction channels available in (a) the case in which the atom is situated on-axis; and (b) the off-axis case. In (a), any change in OAM of the atomic electron is immediately apparent as a change in OAM of the transmitted beam, $\Delta l = l' - l$. The case in (b) is more complicated due to the expansion modes having various OAM p, which may each transfer any number of units of OAM to the atomic electron. The resulting changes Δl values may correspond to a variety of combinations of expansion modes and multipolar transitions, as shown. However, due to the relative strengths of the expansion modes and multipolar atomic transitions, the dominant interaction channels arise from the dipole interaction with the $p = l$ mode. Notice that p is used here only to indicate the OAM modes involved in an off-axis vortex beam, not as a radial index as in the rest of the text. Image from Yuan $et\ al.$ (2013).

2014a). As pointed out above, interactions in these regions are most likely to involve the $p = l$ modes, and thus the change in orbital angular momentum of the vortex in the laboratory frame is indicative of the atomic change in magnetic quantum number. A schematic of such an experiment is shown in Fig. 20 - a vortex beam is incident on a sample, with the resulting transmitted beam split into the the various orbital angular momentum components by a vorticity analyser. After the passing through the sample, the transmitted beam contains several different OAM component l' from the various interactions, along with the original value l from electrons passing though unscattered. Analysis of the various OAM components will allow the determination of the change in the OAM of the atom - it has been shown that a suitable analyser may take the form of a forked holographic mask in conjunction with a pinhole (Saitoh $et\ al.$, 2013). The pinhole will enable the isolation of specific OAM components for measurement of EELS spectra for that channel, allowing detection of only those transmitted electrons having $l' = 0$; for example, those that have suffered a loss (gain) of one unit of orbital angular momentum in the interaction with an $l = +1(-1)$ incident vortex. The pinhole acts to select only those transitions that have both $p = l$ contributions and that are scattered to $l' = p' = 0$ states.
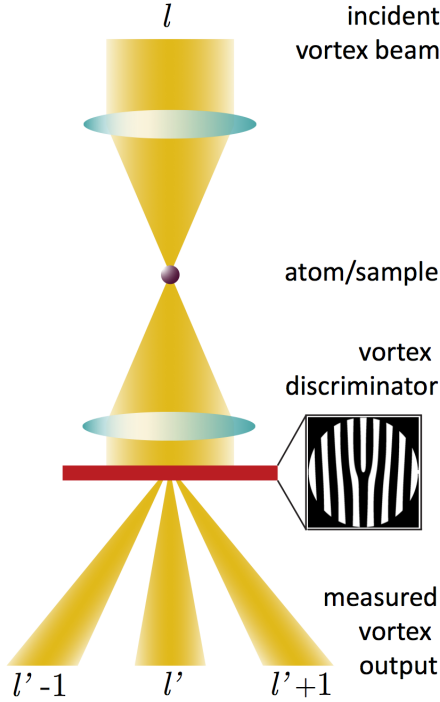
FIG. 20: (Color online) Schematic of suggested experimental set up for OAM based spectroscopy using electron vortices. A vortex beam, produced by a holographic mask or other suitable method (not shown) is incident onto a thin sample in the specimen plane. After interaction with the sample, the transmitted beam is then passed though a forked mask in order to separate the various vortex components. A pinhole placed in the diffraction plane allows isolation of those modes that have an OAM of 0 after passing though the mask - these can then be detected to obtain EELS.

Repeating the experiment using a vortex beam of opposite OAM, i.e. $-l$ will enable a dichroism spectrum to be obtained.

The advantage of this method over the experiment demonstrated in (Verbeeck *et al.*, 2010) should be an increase in signal to noise ratio, since the forward and reverse interactions are treated separately (the additional off-axis features and higher-multipole excitations also contribute to a background noise with a non-vortex incident beam). In this way, probing specific atomic transitions is feasible with varying incident vortices, including higher order multipole transitions using incident vortices with orbital angular momentum greater than $\pm\hbar$. On the other hand, since the transmitted intensities in these cases are expected to be small, the experimental conditions must be optimised so that long collection times may be utilised. Experimental feasibility study is encouraging (Schachinger *et al.*, 2017), especially for amorphous magnetic materials.

Since they were first reported, it has been suggested that electron vortex beams may be combined with the atomic resolution microscope probes to enable chiral spectroscopy with atomic resolution (Idrobo and Pennycook, 2011; Lloyd *et al.*, 2012c; Rusz and Bhowmick, 2013; Verbeeck *et al.*, 2011a, 2010; Yuan *et al.*, 2013). However, there is currently some debate as to the conditions under which such high resolution will be achievable, and the limits of application of the vortex beam (Pohl *et al.*, 2015). Specifically, are the sub-nanometre scale vortex beams described in Verbeeck *et al.* (2011a) suitable for atomic resolution dichroism experiments? It has been argued that the sub-nanometre FWHM of such beams is not sufficient due to the inherent incoherence in the microscope. On the other hand, it has also been argued that it is only in the atomic resolution limit that vortex chiral dichroism experiments will give any improvement over the intrinsic EMCD effect due to the crystal structure acting to diffract the vortex modes (Rusz and Bhowmick, 2013). Simulations of inelastic scattering of vortex beams through iron crystals up to 20 nm thick shows that magnetic information is available only when the radius of the vortex beam is of the order of the atomic radius. In this case, the energy filtered diffraction signal shows a magnetic component of approximately 10% of the background, non-magnetic signal, and is strongly dependent on the position of incidence within the unit cell, so displaying atomic resolution (Rusz and Bhowmick, 2013).

The inelastic scattering of an electron vortex beam by atoms has also been further investigated for hydrogen by (van Boxem *et al.*, 2015), by including the explicit radial distribution functions.

3. Plasmon spectroscopy

In addition to the research into chiral excitation of core electron transitions which is relevant to the excitation of magnetic sublevels in the inner shell of the atoms. Asenjo-Garcia *et al.* have calculated the chiral plasmon response (Asenjo-Garcia and García de Abajo, 2014) which is due to the coupling of the charges in the vortex beam with the electric field of the collective motion of the valence electrons.

The application of vortex beams to EELS may also have potential in mapping the magnetic response of materials in the form of magnetic plasmon resonances (Mohammadi *et al.*, 2012). Magnetic plasmon resonances in nanoparticle arrays are expected to lead to the production of metamaterials, exhibiting negative permittivity and permeability in the optical range (Podolskiy *et al.*, 2002; Sarychev *et al.*, 2006), such that vortex based magnetic plasmon EELS (vortex-EELS) would provide an invaluable tool for the characterisation of metamaterial response. EELS is already well applied in the de-

termination of electric plasmon resonances of nanoparticles (Bosman *et al.*, 2007; Hörl *et al.*, 2013; Nelayah *et al.*, 2007), vortex-EELS should provide a complementary technique, with the additional possibility of gathering information on both the electric and magnetic responses of nanoparticles simultaneously in a single experiment, since the electron vortex will also induce electron plasmon resonances in addition to magnetic plasmon resonances.

A theoretical treatment of the magnetic response of an array of split ring resonators has been demonstrated (Mohammadi *et al.*, 2012), allowing direct comparison of the electric and magnetic plasmon resonance spectra and spatial distribution. Making use of the duality of the electric and magnetic fields allows the relationships between the induced resonance field and the beam current - related by Green's functions - to be recast into an induced magnetic field, regulated by a magnetic Green's function, and induced by the effective magnetic current of the vortex beam (Mohammadi *et al.*, 2012). From here, the magnetic EELS spectra can be calculated using standard finite-difference time-domain techniques. For a split-ring resonator the results of such simulations show a strong magnetic response on the inside of the ring, contrasting with the electric response at the ends of the arms, as shown in Fig. 21. The calculated spatial profiles are consistent with previous theoretical work on electric and magnetic resonances of nanoparticles of similar sizes and shapes (Enkrich *et al.*, 2005; Sarychev *et al.*, 2006). Critically, the intensity of the magnetic response is within an order of magnitude of the electric response, indicating that measurement of magnetic plasmon resonances should be experimentally accessible (Mohammadi *et al.*, 2012). Naturally, in an experimental situation, the vortex beam will induce electric plasmon resonances at the same time as the magnetic resonances, which for metamaterial development will necessarily be within similar energy ranges - notably within the visible light spectrum. Energy filtering is therefore insufficient to fully isolate the magnetic component of the EELS spectrum. For nanostructures for which the electric response is well understood, separating the magnetic signal may be possible by subtracting a separately measured non-vortex-EELS signal from the vortex-EELS map, or by filtering the transmitted signal by its OAM content (Mohammadi *et al.*, 2012). This latter method requires further investigation into the role of orbital angular momentum transfer in magnetic resonances, as it is not immediately apparent that OAM transfer is a requirement for vortex-induced magnetic plasmon resonance.

B. Propagation in crystalline materials

In order that experiments involving vortex beams travelling in real materials to be appropriately interpreted, it
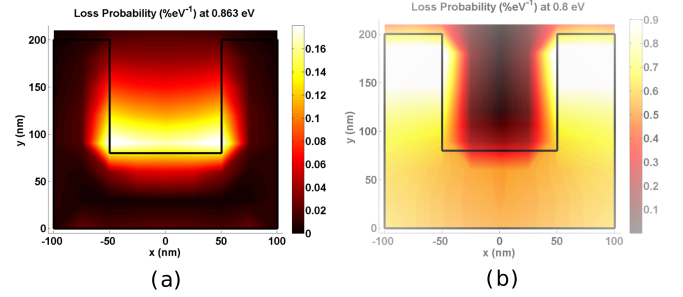

FIG. 21: (Color online) Spatial maps of electron energy loss probability for (a) magnetic resonance at 0.863 eV, with an $l = 1$ beam, and (b) electric resonance at 0.8 eV with a plane wave beam, both at 100 keV beam energy. The two plasmon resonance maps show markedly different spatial profiles, as well as the magnetic resonance response being approximately an order of magnitude less than the electric response. Images from Mohammadi *et al.* (2012)

is necessary that the way such beam propagates through crystalline structures is well understood. Any electron probe propagating through a crystal will experience strong elastic scattering from Coulomb interaction with the atomic nuclei, proportional to the thickness of the sample and tilt relative to the beam axis, as well as channeling along the atomic columns (Reimer and Kohl, 2008; Williams and Carter, 2009). Due to this scattering potential, the trajectory of the vortex and the local orbital angular momentum density of the beam will be altered, since the crystal potential breaks the cylindrical symmetry of the beam, leading to coherent superposition of OAM eigenstates that change in composition through the crystal (Löffler *et al.*, 2012). Because of the exchange of orbital angular momentum between the lattice and the beam the local values of orbital angular momentum within the crystal may be quite different from those of the original, incident vortex beam (Löffler *et al.*, 2012; Lubk *et al.*, 2013a,b); additionally the trajectories of the vortex lines are no longer simple, involving oscillatory motions, looping and the generation of vortex-anti-vortex pairs (Lubk *et al.*, 2013a,b). It is worth mentioning that vortex structure can also be produced by dynamical scattering of crystals by a non-vortex incident electron beam (Allen *et al.*, 2001) because of multiple scattering (Nye and Berry, 1974).

Multislice simulations of the propagation of vortex beams through iron (Löffler *et al.*, 2012) and strontium titanate (Lubk *et al.*, 2013a) crystals have been carried out to explore the complex dynamics arising from the interaction. Both the Fe and $SrTiO_3$ materials are relevant since Fe is a simple and widely available material and is of specific interest in understanding the chiral spectroscopy EELS results reported in (Verbeeck *et al.*, 2010), while the more complex $SrTiO_3$ crystal consists of atomic species of varying mass, allowing for more complex dy-

namics. In both cases, investigations of the phase and amplitude of the wavefunction within the crystal demonstrate that the resulting exit wave depends strongly not only on the thickness of the crystal, but also the position of the incident beam in the unit cell, as well as the topological charge of the vortex.

For an incident vortex beam with $l = 1$ the expectation value of orbital angular momentum within the iron crystal is found to oscillate with propagation, and may take values significantly different to the original, including non-integer values and even reversing in sign (Löffler et $al.$, 2012). For the $SrTiO_3$ crystal, the vortex is found to channel strongly along the atomic columns, and is protected from delocalisation compared to a non-vortex beam, remaining in an approximate angular momentum eigenstate within a certain radius, beyond which the wavefunction exhibits Rankine-like vortex behaviour (Lubk et $al.$, 2013a; Swartzlander and Hernandez-Aranda, 2007). Additionally, vortex-anti-vortex loops are spontaneously generated about the surrounding atomic columns. They manifest themselves as vortex-anti-vortex pairs in the x-y plane as the vortex forming the loop propagates in the z-direction and then turns back on itself (Lubk et $al.$, 2013a). When the vortex beam is incident off centre on an atomic column the core of the vortex is found to circulate around the atomic column, while the centre of mass line remains stationary.

For higher order vortex beams with $l > 1$ interesting dynamics arise that are dependent on the the specific symmetry considerations about the point of incidence. The $l > 1$ vortex beam splits into a number of vortex beams of various orders, the specific order and arrangement of which depend on the specific symmetry. As a result, the local values of orbital angular momentum have a complicated dependence on the strength of the incident vortex state and the specific symmetry of the material as well as the propagation length and position within the unit cell. This is related to the extrinsic nature of the orbital angular momentum as discussed above (see section VI.A.2), and indicates that atoms at different positions within the sample will be subject to modes with vastly different orbital angular momenta. This introduces complications in, for example, electron energy loss spectroscopy, as the atoms within the sample interact with vortices of various strengths. For relatively thick samples then, particular care must be taken in analysis requiring direct observation of phase and intensity contrast; however filtering the separated scattered vortex states will go some way to ameliorating the phase complications.

It has been shown that an electron vortex beam can propagate through atomic columns to a considerable distance by coupling to the 2p columnar orbital with the same angular momentum about the propagation axis. This shows that the divergence of the electron vortex beam can be counteracted by interacting with an atomic column (Xin and Zheng, 2012). The interaction of an electron vortex beam with an atomic column has also been studied by Xie et $al.$ (2014).

One application of electron vortex beams to crystalline materials is in the determination of the chirality of enantiomorphic crystals through diffraction pattern analysis (Juchtmans et $al.$, 2015, 2016). The other predicted application of the electron vortex beam is to make use of the interplay between the elastic and inelastic scattering to determine the magnetic dichroism spectroscopy (Rusz and Bhowmick, 2013; Rusz et $al.$, 2014). Here, as discussed earlier, the small size of the electron vortex beam is important in highlighting the advantage of using electron vortex beams over conventional non-vortex beams.

C. Mechanical transfer of orbital angular momentum

The electron vortex beam carries both linear momentum and orbital angular momentum of $\hbar k_z$ and $\hbar l$ respectively, each along the axial direction. As for optical vortices, the total linear and angular momentum of the electron vortex beam have components which are non-zero only in the axial direction, while both the linear and angular momentum density vectors (defined in Eq. 27 and 31) have additional components in the radial and azimuthal directions (Lloyd et $al.$, 2013; Speirits and Barnett, 2013). These local densities contribute to the diffractive effects within the beam, and the azimuthal momentum density provides the requisite angular motion contributing to the total angular momentum; however components of the total orbital angular momentum do not exist neither radially nor azimuthally.

For the electron vortex, in addition to the mechanical momentum due to the electron mass current, the electric and magnetic fields may also contribute to the total beam momentum and angular momentum. As with mechanical momenta, the contributions to the total linear and angular momentum vectors are found to exist only in the axial directions, despite the field momentum densities having additional radial and azimuthal components (Lloyd et $al.$, 2013). The contributions from the electric and magnetic fields of the electron vortex beam are small; for the typical beam generated within an electron microscope, as described above, the linear and angular momentum contributions due to the electromagnetic fields are approximately 10^{-12} and 10^{-14} that of the mechanical momenta respectively.

As in the case of optical vortices being used to trap and rotate objects from atoms to particles of micron size (Andersen et $al.$, 2006; Barreiro and Tabosa, 2003; Emile et $al.$, 2014; Franke-Arnold et $al.$, 2008; He et $al.$, 1995; Ruffner and Grier, 2012), the influence of an electron vortex beam has been shown to induce rotation in nanoparticles (Gnanavel et $al.$, 2012; Verbeeck et $al.$, 2013). Using the forked holographic mask technique to generate elec-

tron vortex beams within a JEOL 2200FS double aberration corrected scanning transmission electron microscope operated at 200 keV, gold nanoparticles on carbon support were observed to rotate under the influence of the vortex beams (Gnanavel *et al.*, 2012). The nanometre scale vortex beams produced are shown in the focal plane in Fig. 17, having FWHM of 2.6 nm and 3.4 nm respectively for the first and second order beams. No central nodes are observed in the first order beams due to partial coherence effects. In order to minimise these effects, the experiment was performed at a slight defocus such that the beam profile fully covers the 5 nm diameter gold nanoparticle.

The effects of the vortex beam on the nanoparticle were observed using a video capture, with a rate of 0.83 frames per second. Initially, the structural changes, translation and rotation of the particle are minimal; however it was found that after approximately 5 minutes of illumination significant damage had occurred to the carbon substrate with the particle essentially detached, and having also undergone some structural damage. At this point, the particle is relatively free of the van der Waals interaction and effects due viscous trapping potentials, and rotation is observed to occur at an average rate of 3.75° per minute, significantly faster than previous reports involving beams with no orbital angular momentum. Selected frames indicating the nanoparticle rotation are shown in Fig. 22. Although the precise mechanism of the rotation is rather complicated, the existence of the azimuthal component of the linear momentum density is necessary to effect rotation about the beam axis. This rotation is clearly shown to occur due to the vortex nature of the beam by the relatively high rotation rate, and the change of the direction of rotation when the particle is illuminated with a similar beam carrying an opposite OAM (Gnanavel *et al.*, 2012). A similar rotation of gold nanoparticles has been observed on silicon nitride support (Verbeeck *et al.*, 2013).

It has been proposed that the angular momentum transfer between the beam and the particle leading to rotation arises due to the breaking of the cylindrical symmetry of the beam (Verbeeck *et al.*, 2013) by the particle. The exact mechanism of orbital angular momentum transfer between the beam and the nanoparticle depends on a number of variables, notably the relative size of the nanoparticle and the beam, as well as the material properties of the particle, which affect the beam scattering dynamics within the crystal potential, in addition to the experimental parameters (Verbeeck *et al.*, 2013). Furthermore, the requirement that the sample support be damaged before any rotation is observed suggests that friction between the nanoparticle and the support is the limiting factor in this case. Indeed, after prolonged illumination under the beam, the nanoparticle eventually becomes coated with carbon from the support and ceases to rotate.
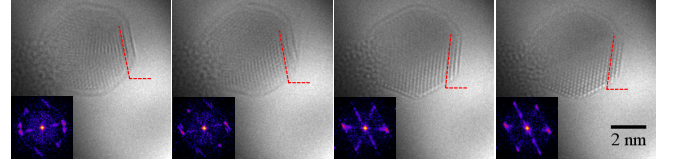

FIG. 22: (Color online) Four snapshots of Au nanoparticles rotated by 2nd order vortex beams selected from a video at 1.2 sec. intervals. The centre dark core surrounded by the bright ring of the 1st order vortex beams is partially visible at the bottom right corner. The angles of lattice fringes noted in figure correspond to 99.5, 99.0, 87.0 and 84.5 degrees respectively. Insets show the corresponding FFT.

This suggests that the electron vortex beam may become a useful tool in the investigation of friction at the nanoscale, which is still not well understood (Mo *et al.*, 2009). Experiments involving the rotation of various species of nanoparticle on a range of supports may thus be considered useful in the characterisation of nanoscale friction. Additionally, a friction-free control environment could be provided by rotation of particles whilst they are levitated by an optical beam (Lloyd *et al.*, 2013). Similar experiments may also be considered to explore viscous forces, for example by using nanoparticles suspended in liquids in a liquid-cell sample holder. The electron vortex provides a method by which particles may be moved transverse to a surface, so that the friction between various surfaces and particles may be investigated directly; this transverse motion may also find application in nano-manipulation for various uses (Falvo and Superfine, 2000), including molecular biophysics applications (Balzer *et al.*, 2013; Bormuth *et al.*, 2009).

D. Polarization radiation

The magnetic moments associated with the orbital angular momentum of the electron vortex beam can be arbitrarily large, in principle, as the axial orbital angular momentum can be very large. The polarisation radiation associated with the passing of a fast moving magnetic dipole moments can display some interesting effects not seen before (Ivanov and Karlovets, 2013a,b; Konkov *et al.*, 2014), such as the circular polarisation of the emitting radiation. The challenge, however is to to be able to produce coherent vortex beams of high topological charges, not in the form of a distribution of a number of vortices of lower order topological charges (Freund, 1999; Ricci *et al.*, 2012).

VII. APPLICATIONS, CHALLENGES AND CONCLUSIONS

We have outlined the various methods currently used for the realisation of electron vortices in the laboratory. We have also emphasised the quantum nature of electron vortices as freely propagating de-Broglie vortex waves endowed with the property of orbital angular momentum about their propagation axis, which also coincides with the vortex core. The intrinsic properties of electron vortices have been pointed out, specifically their mass and charge distributions and how these determine their momentum and orbital angular momentum contents, as well as their spin and its coupling to the orbital angular momentum. This is particularly illuminating in terms of revisiting some of the basics concepts involved. Progress in the study of their interaction with matter has been summarised, especially in connection with magnetic systems and the issue of transfer of orbital angular momentum to the internal dynamics of atomic systems. The possibility of using electron vortices to rotate nanoparticles and current experimental work on this has also been described.

The study of electron vortex beams and their interactions does clearly benefit from the highly advanced state of electron optics used to produce high resolution electron microscopy, electron spectroscopy and electron beam lithography. This sets electron beam technology apart from all other matter beam technologies, with the neutron, ion and atom beams being the distant competitors and it is clear currently that it is much easier to generate electron vortex beams than other matter vortex beams. The downside of the existing electron optics technology is that they are bulky and, unlike optical systems, not easily reconfigurable because of the connected vacuum system essential for the free passage of the electron beams. This means that most of the existing vortex beam research has to be conducted within the existing electron microscopes designed with the science of advanced materials in mind and time-shared with real-world applications as well. Nevertheless, where existing research facilities could be employed with little modification rapid progress has been made. In particular, this is evident in the development of electron vortex beam technology in electron microscopy and our understanding of its characteristics and there is some proof-of-principle demonstrations of its unique capabilities. Much more research is required to understand the intrinsic nature of some of its characteristics as well as the need for developing optimised set-ups for vortex beam experiments so that practical applications can be properly tested. Among the optimised set-ups to be realised would be an electron vortex beam source similar to that available for optical vortex beams (Cai *et al.*, 2012). This would be a useful alternative to the various beam conversion schemes that have been discovered so far. There are some encouraging experimental evidence for that (Schmidt *et al.*,

2014). The electron repulsion that would be expected in a high brightness (many-electron) beam needs to be taken into account. A feasibility study on shape-preserving many electron vortex beam design has been conducted by Mutzafi *et al.* (2014) and the result is promising, indicating that the generation of a high current electron vortex beam is possible.

It is probably too early to apply vortex beams routinely to study the physics of materials because although the existing electron beam set-ups are optimised for electron microscopy, a number of electron vortex beam experiments have already led to applications to be realised in principle. This fact allows us to contemplate on what possible developments in the future might be.

As pointed out at the outset, more applications of electron vortex beams are expected to follow, in which the orbital angular momentum of the beam is expected to provide new information about crystallographic, electronic and magnetic properties of the sample. Magnetic-dependent EELS has already been demonstrated, based on the principles of electron vortex beams, and it is predicted that the high resolution achievable in the electron microscope will lead to the ability to map magnetic information at atomic or near-atomic resolution. The determination of magnetic structure at the nanoscale has always placed a significant demand on electron microscopy. The linear and chiral dichroic spectroscopies (Schattschneider *et al.*, 2006; Yuan and Menon, 1997), based on non-vortex beams have been developed, with the linear dichroism being useful in the study of spin-orientation in antiferromagnetic materials and the chiral dichroism for spin orientation in ferromagnetic materials. Electron vortex spectroscopy offers an alternative method to access chiral-dependent electronic excitations (Yuan *et al.*, 2013).

The orbital angular momentum and magnetic properties of the electron vortex beams may also find potential uses in spintronic applications, either in the characterisation of spintronic devices, or in contexts employing spin-polarised current injection, through spin-to-orbital angular momentum conversion processes (Karimi *et al.*, 2012). The reverse process of spin-filter using spin-orbit coupling in electron Bessel beams has been investigated theoretically (Schattschneider *et al.*, 2017).

Additionally, the inherent phase structure of the vortex is considered ideal for applications in high resolution phase contrast imaging, as required for biological specimens with low absorption contrast (Jesacher *et al.*, 2005) or in revealing local orbital angular momentum density (Juchtmans and Verbeeck, 2016).

Applications of electron vortex beams are, however, not restricted to spectroscopy and imaging - the orbital angular momentum of the beam may also be used for the manipulation of nanoparticles (Gnanavel *et al.*, 2012; Verbeeck *et al.*, 2013), leading to electron spanners analogous to the widely used optical spanners. Electron vortex

states are also relevant in the context of quantum information processing and, in particular, low-energy electron vortex beams may potentially be used to impart angular momentum on Bose-Einstein condensates (Fetter, 2001).

It has also been predicted that the large magnetic moments associated with electron vortex beams of higher orbital angular momentum can be used to produce novel polarisation radiation when passing through materials (Ivanov and Karlovets, 2013a,b). This has led to a drive to produce electron beams with very large topological charges (Grillo *et al.*, 2015).

Both the kinematic and dynamical diffraction of electron vortex beams by chiral crystals have been shown to be sensitive to the helicity of the vortex beam, suggesting a useful characterising tool for the study of chiral crystals.

The study of an electron vortex beam with strong laser fields has also opened up the possibility of accelerating non-relativistic twisted electrons using focused electromagnetic fields (Karlovets, 2012) or beam steering using the high electric fields due to an ultrashort pulsed beam (Bandyopadhyay *et al.*, 2015; Hayrapetyan *et al.*, 2014). Research into laser-electron beam interaction also allows coherent optical vortex beams to be produced (Hemsing *et al.*, 2013). The inverse photoemission process involving an electron vortex beam is another interesting problem for further investigation (Matula *et al.*, 2014; Zaytsev *et al.*, 2017).

In particle physics experiments, the use of vortex beams instead of approximate plane waves would permit a direct measurement to be made as to how the overall phase of the plane wave scattering amplitude changes with the scattering angle (Ivanov *et al.*, 2016; Ivanov, 2012b; Karlovets, 2016). This may be important for many high energy experiments in hadron physics. It is therefore highly desirable to introduce electron vortex beams into high energy particle accelerators.

Vortex beam-beam interactions also open up the possibility of the creation of two vortex-entangled beams, with implications for quantum information processing (Ivanov, 2012a,b).

In conclusion, our review of the area of electron vortex beams has indicated that much progress has already been made in a relatively short period of time, particularly over the last few years. The emphasis so far has been primarily on the fundamental aspects of the electron vortex beams. However, there are still many unexplored topics, ranging from novel vortex beams (Wang and Li, 2011), to image contrast enhancement and to exploring applications of vortex beams in quantum information processing, just to mention a few. The range and complexity of the phenomena involving electron vortex beams point to a brighter future for further developments in this field.

Recent papers

As a sign of growing interest in the vortex beam physics, interesting development is still continuing during the refereeing process of this review. In particular, we highlight the recent proposal to perform a measurement of the OAM content of an electron vortex beam (Larocque *et al.*, 2016) using the microscopic version of the magnetic braking experiment (Donoso, 2009; Donoso *et al.*, 2011; Saslow, 1992) or by weak measurement (Qiu *et al.*, 2016), the possible detection of magnetic contrast in magnetic crystal using Zeeman effect (Edström *et al.*, 2016a,b) as well as the recent debate about the existence of vortex structure in relativistic electron beams (Barnett, 2017; Bialynicki-Birula and Bialynicka-Birula, 2017).

ACKNOWLEDGMENTS

LIST OF SYMBOLS AND ABBREVIATIONS

$\mathbf{A}$	vector potential of externally applied axial magnetic field
α	convergence angle of a focused electron beam
$\bar{\alpha}$	a parameter characterizing the magnetic correction to the effective vortex beam topological charge
D	effective length of the vortex beam
$\delta\phi$	rotation angle
$\delta_{l,s}$	spin-orbit energy
$\Delta\phi$	phase change
Δt	film thickness of phase masks for electron beams
$\mathcal{E}$	energy eigenvalue of the electron vortex beam
$\mathbf{E}$ and $\mathbf{B}$	electric and magnetic vector fields associated with the electron vortex beam
$F_{\mu\nu}$	electromagnetic field tensor
${}_pF_q$	generalised hypergeometric function
g_s	gyromagnetic ratio
$\Gamma(x)$	gamma function
$\mathcal{H}$	Hamiltonian
I	beam electric current
$\mathcal{I}^n$	n^{th} moment integral of the Bessel function
$J_l(x)$	Bessel function of the first kind of order l
$\mathbf{j}(\mathbf{r},t)$	probability current density
$\mathbf{j}_m(\mathbf{r},t)$	mass current density, equivalent to inertia linear momentum density $\mathcal{P}_m$

Symbol	Definition
$\mathbf{J}$	total angular momentum of the electron vortex beam
$\mathbf{k}$	wavevector of the electron wave.
κ	$\sqrt{1 - \frac{m}{E}}$
k_z	axial wavenumber of the electron vortex beam.
$k_\perp$	transverse wavenumber of the electron vortex beam.
l	winding number; also referred to as topological charge or azimuthal index
I_{holo}	hologram intensity
$L_p^l(x)$	generalised Laguerre polynomial with azimuthal index l and radial index p
$\mathcal{L}_m$	inertial angular momentum density of the electron vortex beam
$\mathbf{L}_m$	inertial angular momentum of the electron vortex beam
$\mathcal{L}_{em}$	electromagnetic angular momentum density of the electron vortex beam
$\mathbf{L}_{em}$	global electromagnetic angular momentum of the electron vortex beam
L_z	axial component of the orbital angular momentum operator
$\lambda_{p,l}$	pth zeros of Bessel function of order l
$\lambda_{p,l}$	wavelength
$\mathcal{M}_{fi}$	matrix element of interaction Hamiltonian H_{int} between quantum states i and f
$n(\mathbf{r},t)$	probability density $(= \psi^*\psi)$
n_L	quantised Landau level index
n_{eff}	effective refractive index
n	order of diffraction order
N_l	normalization constant for Bessel beam wavefunction of order l
ω_L	Larmor frequency
ω_c	cyclotron frequency
ω	angular frequency of the vortex beam
Ω	angular frequency of nanoparticles
$\mathcal{P}_m$	inertia linear momentum density of the electron vortex beam
$\mathbf{P}_m$	global inertia linear momentum of the electron vortex beam
$\mathcal{P}_{em}$	linear momentum density associated with the fields of the electron vortex beam
$\mathbf{P}_{em}$	global electromagnetic linear momentum of the electron vortex beam
p	radial index
$\mathbf{p}$	(canonical) linear momentum vector or canonical linear momentum operator in quantum formalism
$\mathbf{p}^{kin}$	(kinetic) linear momentum vector operator $(= \mathbf{p} - e\mathbf{A})$
$\hat{\mathbf{p}}$	electron four momentum operator
ϕ	azimuthal variable in cylindrical polar coordinates
$\hat{\boldsymbol{\phi}}$	unit vector in the azimuthal direction
φ	magnetic flux
Φ	electrostatic potential
$\psi(\rho,\phi,z)$	electron vortex wavefunction in cylindrical coordinates
$\psi_{p,l}^{LG}$	wave-function of Laguerre-Gaussian electron vortex beam of winding number l and radial index p
ψ_l^B	wavefunction of Bessel electron vortex beam of winding number l
ψ_B^{LG}	wavefunction of electron vortex wavefunction in a constant magnetic field B
ψ^{AB}	wavefunction of electron vortex wavefunction threading a single magnetic flux
$\psi_{p,l}^{tB}$	wavefunction of truncated Bessel beam of winding number l and radial index p
Ψ	four-component relativistic wavefunction of an electron vortex beam
q	topological order of defects in liquid crystal
ρ	in-plane radial variable in cylindrical polar coordinates
$\rho_m(\mathbf{r},t)$	mass density $(= mn(\mathbf{r},t))$
$\rho_e(\mathbf{r},t)$	charge density $(= en(\mathbf{r},t))$
$\hat{\boldsymbol{\rho}}$	unit vector in the in-plane radial direction
$\mathbf{r}(\rho,\phi,z)$	position vector in cylindrical coordinates
ρ_m	radius of maximum intensity of the vortex beam
R_{max}	radius of the aperture/mask
$R(z)$	curvature of the wavefront of a gaussian beam
$\mathbf{S}$	spin half angular momentum vector operator
$S(t)$	an odd, self-adjoint operator used in Foldy and Wouthuysen transform
s	spin quantum number
Σ	helicity of the beam
σ_i	i^{th} component of Pauli matrix
$\sigma_{\mu\nu}$	Spin tensor
θ	angle of the cone of Bessel plane waves
$\Theta(x)$	Heaviside step function
$u(\rho,z)$	transverse mode function
$w(z)$	beam radius at coordinate z from focus plane
w_0	beam radius at focus;
w_B	beam width in the presence of magnetic field
$\mathbf{w}$	two component spinor characterizing the electron polarization in the rest frame with $E = m$.
ξ	spin-orbit coupling constant
z	z- variable in cylindrical polar coordinates
$\hat{\mathbf{z}}$	unit vector in the z- direction
z_R	Rayleigh range of the focused beam
z_B	magnetic Rayleigh range

REFERENCES

Abramowitz, M, and IA Stegun (1972), *Handbook of mathematical functions: with formulas, graphs, and mathematical tables*, Tech. Rep. (National Bureau of Standard).

Aharonov, Y, and D. Bohm (1959), "Significance of Electromagnetic Potentials in the Quantum Theory," Physical Review **115** (3), 485–491.

Airy, AM (1834), "Transactions of the Cambridge Philosophical Society, Volume XXII (1912-1923)," Transactions of the Cambridge Philosophical Society **V** (III), 283.

Alexandrescu, A, E Di Fabrizio, and D Cojoc (2005), "Electronic and centre of mass transitions driven by Laguerre-Gaussian beams," Journal of Optics B: Quantum and Semiclassical Optics **7** (4), 87–92.

Allen, L, M Babiker, W K Lai, and V E Lembessis (1996a), "Atom dynamics in multiple Laguerre-Gaussian beams," Physical Review A **54** (5), 4259–4270.

Allen, L, Stephen M Barnett, and Miles J Padgett (2003), *Optical Angular Momentum* (Institute of Physics Pub., Bristol).

Allen, L, M. W. Beijersbergen, R. J. C. Spreeuw, and J. P. Woerdman (1992), "Orbital angular momentum of light and the transformation of Laguerre-Gaussian laser modes," Physical Review A **45** (11), 8185–8189.

Allen, L, V. E. Lembessis, and M Babiker (1996b), "Spin-orbit coupling in free-space Laguerre-Gaussian light beams," Physical Review A **53** (5), R2937–R2939.

Allen, L, M.J. Padgett, and M. Babiker (1999), "IV The Orbital Angular Momentum of Light," in *Progress in Optics* (Insitutte of Physics) pp. 291–372.

Allen, L J, H M Faulkner, K a Nugent, M P Oxley, and D Paganin (2001), "Phase retrieval from images in the presence of first-order vortices." Physical review. E, Statistical, nonlinear, and soft matter physics **63** (September 2000), 037602.

Andersen, M, C. Ryu, Pierre Cladé, Vasant Natarajan, A. Vaziri, K. Helmerson, and W. Phillips (2006), "Quantized Rotation of Atoms from Photons with Orbital Angular Momentum," Physical Review Letters **97** (17), 170406.

Andrews, David L, and Mohamed Babiker (2012), *The Angular Momentum of Light*, edited by David L. Andrews and Mohamed Babiker (Cambridge University Press, Cambridge, U.K.).

Andrews, DL, L.C.Dávila Romero, and M Babiker (2004), "On optical vortex interactions with chiral matter," Optics Communications **237** (1-3), 133–139.

Araoka, F, T Verbiest, K Clays, and A Persoons (2005), "Interactions of twisted light with chiral molecules: An experimental investigation," Physical Review A **71** (5), 055401.

Asenjo-Garcia, A, and F. J. García de Abajo (2014), "Dichroism in the Interaction between Vortex Electron Beams, Plasmons, and Molecules," Physical Review Letters **113** (6), 066102.

Babiker, M, C. Bennett, D. Andrews, and L. Dávila Romero (2002), "Orbital Angular Momentum Exchange in the Interaction of Twisted Light with Molecules," Physical Review Letters **89** (14), 143601.

Babiker, M, W. L. Power, and L. Allen (1994), "Light-induced Torque on Moving Atoms," Physical Review Letters **73** (9), 1239–1242.

Babiker, M, J. Yuan, and V. E. Lembessis (2015), "Electron vortex beams subject to static magnetic fields," Physical Review A **91** (1), 013806.

Balzer, Bizan N, Markus Gallei, Moritz V Hauf, Markus Stallhofer, Lorenz Wiegleb, Alexander Holleitner, Matthias Rehahn, and Thorsten Hugel (2013), "Nanoscale Friction Mechanisms at Solid-Liquid Interfaces," Angewandte Chemie International Edition **52** (25), 6541–6544.

Bandyopadhyay, Pratul, Banasri Basu, and Debashree Chowdhury (2014), "The geometric phase and the geometrodynamics of relativistic electron vortex beams," Proceedings of the Royal Society A: Mathematical, Physical and Engineering Sciences **470** (2163), 20130525–20130525.

Bandyopadhyay, Pratul, Banasri Basu, and Debashree Chowdhury (2015), "Relativistic Electron Vortex Beams in a Laser Field," Physical Review Letters **115** (19), 194801.

Bandyopadhyay, Pratul, Banasri Basu, and Debashree Chowdhury (2016), "Unified Approach towards the Dynamics of Optical and Electron Vortex Beams," Physical Review Letters **116** (14), 1–5, arXiv:1603.03155.

Bandyopadhyay, Pratul, Banasri Basu, and Debashree Chowdhury (2017), "Geometric phase and fractional orbital-angular-momentum states in electron vortex beams," Physical Review A **95** (1), 013821, arXiv:1608.03562.

Baranek, M, and Z. Bouchal (2013), "Rotating vortex imaging implemented by a quantized spiral phase modulation," Journal of the European Optical Society: Rapid Publications **8**, 13017.

Barnett, Stephen M (2017), "Relativistic Electron Vortices," Physical Review Letters **118** (11), 114802.

Barnett, Stephen M, and L Allen (1994), "Orbital angular momentum and nonparaxial light beams," Optics Communications **110** (5-6), 670–678.

Barreiro, S, and J. W. R. Tabosa (2003), "Generation of Light Carrying Orbital Angular Momentum via Induced Coherence Grating in Cold Atoms," Physical Review Letters **90** (13), 133001.

Batson, P E, N Dellby, and O L Krivanek (2002), "Sub-ångstrom resolution using aberration corrected electron optics," Nature **418** (6898), 617–620.

Béché, A, R. Juchtmans, and J. Verbeeck (2016), "Efficient creation of electron vortex beams for high resolution STEM imaging," Ultramicroscopy , 1–8.

Béché, Armand, Ruben van Boxem, Gustaaf Van Tendeloo, and Jo Verbeeck (2013), "Magnetic monopole field exposed by electrons," Nature Physics **10** (1), 26–29.

Beijersbergen, MW, L Allen, H.E.L.O. van der Veen, and J.P. Woerdman (1993), "Astigmatic laser mode converters and transfer of orbital angular momentum," Optics Communications **96** (1-3), 123–132.

Bérard, Alain, and Hervé Mohrbach (2006), "Spin Hall effect and Berry phase of spinning particles," Physics Letters A **352** (3), 190–195.

Berkhout, Gregorius, Martin Lavery, Johannes Courtial, Marco Beijersbergen, and Miles Padgett (2010), "Efficient Sorting of Orbital Angular Momentum States of Light," Physical Review Letters **105** (15), 8–11.

Berkhout, Gregorius C G, and Marco W. Beijersbergen (2008), "Method for Probing the Orbital Angular Momentum of Optical Vortices in Electromagnetic Waves from Astronomical Objects," Physical Review Letters **101** (10), 100801.

Berry, M V (2004), "Optical vortices evolving from helicoidal integer and fractional phase steps," Journal of Optics A:

Pure and Applied Optics **6**, 259–268.

Berry, M V, and M R Dennis (2007), "Topological events on wave dislocation lines: birth and death of loops, and reconnection," Journal of Physics A: Mathematical and Theoretical **40** (1), 65–74.

Berry, M V, and M R Dennis (2012), "Reconnections of wave vortex lines," European Journal of Physics **33** (3), 723–731.

Bhattacharyya, Somnath, Christoph T. Koch, and Manfred Rühle (2006), "Projected potential profiles across interfaces obtained by reconstructing the exit face wave function from through focal series," Ultramicroscopy **106** (6), 525–538.

Bialynicki-Birula, Iwo, and Zofia Bialynicka-Birula (2001), "Motion of vortex lines in nonlinear wave mechanics," Physical Review A **65** (1), 014101.

Bialynicki-Birula, Iwo, and Zofia Bialynicka-Birula (2017), "Relativistic Electron Wave Packets Carrying Angular Momentum," Physical Review Letters **118** (11), 114801, arXiv:1611.04445.

Bialynicki-Birula, Iwo, Zofia Bialynicka-Birula, and Cezary Śliwa (2000), "Motion of vortex lines in quantum mechanics," Physical Review A **61** (3), 032110.

Bialynicki-Birula, Iwo, Tomasz Mloduchowski, Tomasz Radozycki, and Cezary Śliwa (2001), "Vortex Lines in Motion," Acta Physica Polonica A **100** (Supplement), 29–41.

Bialynicki-Birula, Iwo, and Tomasz Radożycki (2006), "Pinning and transport of cyclotron (Landau) orbits by electromagnetic vortices," Physical Review A **73** (5), 052114.

Bjorken, J D, and S D Drell (1964), *Relativistic Quantum Mechanics* (Mcgraw-Hill College, New York).

Blackburn, AM, and J.C. Loudon (2014), "Vortex beam production and contrast enhancement from a magnetic spiral phase plate," Ultramicroscopy **136**, 127–143.

Bliokh, Konstantin, Yury Bliokh, Sergey Savel'ev, and Franco Nori (2007), "Semiclassical Dynamics of Electron Wave Packet States with Phase Vortices," Physical Review Letters **99** (19), 190404.

Bliokh, Konstantin Y, Miguel Alonso, Elena Ostrovskaya, and Andrea Aiello (2010), "Angular momenta and spin-orbit interaction of nonparaxial light in free space," Physical Review A **82** (6), 63825.

Bliokh, Konstantin Y, Mark R. Dennis, and Franco Nori (2011), "Relativistic Electron Vortex Beams: Angular Momentum and Spin-Orbit Interaction," Physical Review Letters **107** (17), 174802.

Bliokh, Konstantin Y, Avi Niv, Vladimir Kleiner, and Erez Hasman (2008), "Geometrodynamics of spinning light," Nature Photonics **2** (12), 748–753.

Bliokh, Konstantin Y, and Franco Nori (2012a), "Relativistic Hall Effect," Physical Review Letters **108** (12), 120403.

Bliokh, Konstantin Y, and Franco Nori (2012b), "Spatiotemporal vortex beams and angular momentum," Physical Review A **86** (3), 033824.

Bliokh, Konstantin Y, Peter Schattschneider, Jo Verbeeck, and Franco Nori (2012), "Electron Vortex Beams in a Magnetic Field: A New Twist on Landau Levels and Aharonov-Bohm States," Physical Review X **2** (4), 041011.

Bliokh, Konstantin Yu (2006), "Geometrical Optics of Beams with Vortices: Berry Phase and Orbital Angular Momentum Hall Effect," Physical Review Letters **97** (4), 043901.

Bormuth, Volker, Vladimir Varga, Jonathon Howard, and E. Schaffer (2009), "Protein Friction Limits Diffusive and Directed Movements of Kinesin Motors on Microtubules," Science **325** (5942), 870–873.

Born, M, E. Wolf, M Borm, and E. Wolf (1997), *Optica Acta: International Journal of Optics* (Cambridge University Press, Cambridge, U.K.).

Bosman, Michel, Vicki J Keast, Masashi Watanabe, Abbas I Maaroof, and Michael B Cortie (2007), "Mapping surface plasmons at the nanometre scale with an electron beam," Nanotechnology **18** (16), 165505.

van Boxem, Ruben, Jo Verbeeck, and Bart Partoens (2013), "Spin effects in electron vortex states," EPL (Europhysics Letters) **102** (4), 40010.

Cai, Xinlun Xin-Lun, Jian-Wei (University of Bristol) Jianwei Wang, Michael J. Strain, Benjamin Johnson-Morris, Jiang-Bo Jiangbo Zhu, Marc Sorel, Jeremy L. O'Brien, Mark G. Thompson, and Siyuan Si-Yuan Yu (2012), "Integrated Compact Optical Vortex Beam Emitters," Science **338** (6105), 363–366.

Cardano, Filippo, Ebrahim Karimi, Sergei Slussarenko, Lorenzo Marrucci, Corrado de Lisio, and Enrico Santamato (2012), "Polarization pattern of vector vortex beams generated by q-plates with different topological charges," Applied Optics **51** (10), C1.

Carra, Paolo, B T Thole, Massimo Altarelli, and Xindong Wang (1993), "X-ray circular dichroism and local magnetic fields," Physical Review Letters **70** (5), 694–697.

Chowdhury, Debashree, Banasri Basu, and Pratul Bandyopadhyay (2015), "Electron vortex beams in a magnetic field and spin filter," Physical Review A **91** (3), 033812.

Clark, Charles W, Roman Barankov, Michael G. Huber, Muhammad Arif, D G Cory, and Dmitry a. Pushin (2015), "Controlling neutron orbital angular momentum," Nature **525** (7570), 504–506.

Clark, L, A. Béché, G. Guzzinati, A. Lubk, M. Mazilu, R. van Boxem, and J. Verbeeck (2013), "Exploiting Lens Aberrations to Create Electron-Vortex Beams," Physical Review Letters **111** (6), 064801.

Clark, L, a. Béché, G. Guzzinati, and J. Verbeeck (2014), "Quantitative measurement of orbital angular momentum in electron microscopy," Physical Review A **89** (5), 053818.

Clark, Laura, S Lloyd, Mohamed Babiker, and Jun Yuan (2012), "Electron Beams with a Twist," Journal of Physics: Conference Series **371**, 012005.

Coullet, P, L. Gil, and F. Rocca (1989), "Optical vortices," Optics Communications **73** (5), 403–408.

Courtial, J, and M Padgett (1999), "Performance of a cylindrical lens mode converter for producing LaguerreGaussian laser modes," Optics Communications **159** (1-3), 13–18.

Curtis, Jennifer E, and David G Grier (2003), "Structure of optical vortices." Physical review letters **90** (APRIL), 133901.

Danev, R, H. Okawara, N. Usuda, K. Kametani, and K. Nagayama (2002), "A Novel Phase-contrast Transmission Electron Microscopy Producing High-contrast Topographic Images of Weak objects," Journal of Biological Physics **28** (4), 627–635.

Dholakia, Kishan, Michael Macdonald, Gabriel Spalding, and Michael Macdonald (2002), "Optical tweezers : the next generation," Physics World **15** (October 2002), 31–35.

Donoso, G (2009), "Magnet fall inside a conductive pipe : motion and the role of the pipe wall," **855**, 10.1088/0143-0807/30/4/018.

Donoso, Guillermo, Celso L. Ladera, and Pablo Martin (2011), "Damped fall of magnets inside a conducting pipe," American Journal of Physics **79** (2), 193.

Durnin, J, JJ Miceli Jr, and JH Eberly (1987), "Diffraction-free beams," Physical Review Letters **58** (15), 1499–1501.

Dwyer, C, C.B. Boothroyd, S.L.Y. Chang, and R.E. Dunin-Borkowski (2015), "Three-wave electron vortex lattices for measuring nanofields," Ultramicroscopy **148**, 25–30.

Edström, Alexander, Axel Lubk, and Ján Rusz (2016a), "Elastic Scattering of Electron Vortex Beams in Magnetic Matter," Physical Review Letters **116** (12), 127203, arXiv:1509.00744.

Edström, Alexander, Axel Lubk, and Ján Rusz (2016b), "Magnetic effects in the paraxial regime of elastic electron scattering," Physical Review B **94** (17), 174414.

Emile, Olivier, Christian Brousseau, Janine Emile, Ronan Niemiec, Kouroch Madhjoubi, and Bo Thide (2014), "Electromagnetically Induced Torque on a Large Ring in the Microwave Range," Physical Review Letters **112** (5), 053902.

Enkrich, C, M Wegener, S Linden, S Burger, L Zschiedrich, F Schmidt, J Zhou, Th. Koschny, and C Soukoulis (2005), "Magnetic Metamaterials at Telecommunication and Visible Frequencies," Physical Review Letters **95** (20), 203901.

Erni, Rolf, Marta Rossell, Christian Kisielowski, and Ulrich Dahmen (2009), "Atomic-Resolution Imaging with a Sub-50-pm Electron Probe," Physical Review Letters **102** (9), 096101.

Falvo, Michael R, and Richard Superfine (2000), "Mechanics and friction at the nanometer scale," Journal of Nanoparticle Research **2**, 237–248.

Faraday, M (1936), *Faraday's Diary IV*, edited by T Martin (G. Bell and Sons, London).

Feng, Simin, and Herbert G Winful (2001), "Physical origin of the Gouy phase shift," Optics Letters **26** (8), 485–487.

Fetter, A L (2001), "Vortices in a trapped dilute Bose-Einstein condensate," Journal of Physics: Condensed Matter **13**, R135—-R194.

Foldy, Leslie L, and Siegfried a. Wouthuysen (1950), "On the Dirac Theory of Spin 1/2 Particles and Its Non-Relativistic Limit," Physical Review **78** (1), 29–36.

Franke-Arnold, Sonja, Les Allen, and Miles Padgett (2008), "Advances in optical angular momentum," Laser and Photonics Reviews **2** (4), 299–313.

Franke-Arnold, Sonja, Stephen M. Barnett, Eric Yao, Jonathan Leach, Johannes Courtial, and Miles Padgett (2004), "Uncertainty principle for angular position and angular momentum," New Journal of Physics **6**, 103–103.

Franke-Arnold, Sonja, Graham Gibson, Robert W. Boyd, and Miles J Padgett (2011), "Rotary photon drag enhanced by a slow-light medium." Science **333** (6038), 65–67.

Freund, Isaac (1999), "Critical point explosions in two-dimensional wave fields," Optics Communications **159** (1-3), 99–117.

Fürhapter, Severin, Alexander Jesacher, Stefan Bernet, and Monika Ritsch-Marte (2005), "Spiral phase contrast imaging in microscopy." Optics express **13** (3), 689–694.

Gabor, D (1948), "A new microscopic principle," Nature **161** (4098), 777.

Galajda, Péter, and Pál Ormos (2001), "Complex micromachines produced and driven by light," Applied Physics Letters **78** (2), 249–251.

Gallatin, Gregg M, and Ben McMorran (2012), "Propagation of vortex electron wave functions in a magnetic field," Physical Review A **86** (1), 012701.

Giammanco, F, A. Perona, P. Marsili, F. Conti, F. Fidecaro, S. Gozzini, and A. Lucchesini (2017), "Influence of the photon orbital angular momentum on electric dipole tran-

sitions: negative experimental evidence," Optics Letters **42** (2), 219.

Gnanavel, T, J Yuan, and M Babiker (2012), "Observation of gold nanoparticles movements under sub-10 nm vortex electron beams in an aberration corrected TEM," in *Proceedings of the 15th European Microscopy Congresss*, ii (Royal Microscopy Society, Manchester, UK).

Greenshields, Colin, Robert L Stamps, and Sonja Franke-Arnold (2012), "Vacuum Faraday effect for electrons," New Journal of Physics **14** (10), 103040.

Greenshields, Colin R, Robert L. Stamps, Sonja Franke-Arnold, and Stephen M. Barnett (2014), "Is the Angular Momentum of an Electron Conserved in a Uniform Magnetic Field?" Physical Review Letters **113** (24), 240404.

Grier, David G (2003), "A revolution in optical manipulation." Nature **424** (6950), 810–6.

Grillo, Vincenzo, Gian Carlo Gazzadi, Ebrahim Karimi, Erfan Mafakheri, Robert W. Boyd, and Stefano Frabboni (2014a), "Highly efficient electron vortex beams generated by nanofabricated phase holograms," Applied Physics Letters **104** (4), 043109.

Grillo, Vincenzo, Gian Carlo Gazzadi, Erfan Mafakheri, Stefano Frabboni, Ebrahim Karimi, and Robert W Boyd (2015), "Holographic Generation of Highly Twisted Electron Beams," Physical Review Letters **114** (3), 034801.

Grillo, Vincenzo, Jérémie Harris, Gian Carlo Gazzadi, Roberto Balboni, Erfan Mafakheri, Mark R Dennis, Stefano Frabboni, and Robert W Boyd (2016), "Generation and Application of Bessel Beams in Electron Microscopy," Ultramicroscopy **166**, 48–60.

Grillo, Vincenzo, Ebrahim Karimi, Gian Carlo Gazzadi, Stefano Frabboni, Mark R. Dennis, and Robert W. Boyd (2014b), "Generation of Nondiffracting Electron Bessel Beams," Physical Review X **4** (1), 011013.

Grillo, Vincenzo, Lorenzo Marrucci, Ebrahim Karimi, Riccardo Zanella, and Enrico Santamato (2013), "Quantum simulation of a spin polarization device in an electron microscope," New Journal of Physics **15** (9), 093026.

Guzzinati, Giulio, Laura Clark, Armand Béché, and Jo Verbeeck (2014), "Measuring the orbital angular momentum of electron beams," Physical Review A **89** (2), 025803.

Guzzinati, Giulio, Peter Schattschneider, Konstantin Y. Bliokh, Franco Nori, and Jo Verbeeck (2013), "Observation of the Larmor and Gouy Rotations with Electron Vortex Beams," Physical Review Letters **110** (9), 093601.

Handali, Jonathan, Pratistha Shakya, and Brett Barwick (2015), "Creating electron vortex beams with light," Optics Express **23** (4), 5236.

Harris, Jérémie, Vincenzo Grillo, Erfan Mafakheri, Gian Carlo Gazzadi, Stefano Frabboni, Robert W. Boyd, and Ebrahim Karimi (2015), "Structured quantum waves," Nature Physics **11** (8), 629–634.

Harvey, Tyler, Jordan Pierce, Amit Agrawal, Peter Ercius, Martin Linck, and Benjamin J McMorran (2014), "Efficient diffractive phase optics for electrons," New Journal of Physics **16** (9), 093039.

Hasegawa, Yuya, Koh Saitoh, Nobuo Tanaka, and Masaya Uchida (2013), "Propagation Dynamics of Electron Vortex Pairs," Journal of the Physical Society of Japan **82** (7), 073402.

Hayrapetyan, Armen G, Oliver Matula, Andrea Aiello, Andrey Surzhykov, and Stephan Fritzsche (2014), "Interaction of Relativistic Electron-Vortex Beams with Few-Cycle Laser Pulses," Physical Review Letters **112** (13), 134801.

Hayrapetyan, Armen G, Oliver Matula, Andrey Surzhykov, and Stephan Fritzsche (2013), "Bessel beams of two-level atoms driven by a linearly polarized laser field," The European Physical Journal D **67** (8), 167.

He, H, MEJ Friese, NR Heckenberg, and H. Rubinsztein-Dunlop (1995), "Direct observation of transfer of angular momentum to absorptive particles from a laser beam with a phase singularity," Physical Review Letters **75** (5), 826–829.

Heckenberg, N R, R. McDuff, C. P. Smith, H. Rubinsztein-Dunlop, and M. J. Wegener (1992a), "Laser beams with phase singularities," Optical and Quantum Electronics **24** (9), S951–S962.

Heckenberg, N R, R. McDuff, C. P. Smith, and a. G. White (1992b), "Generation of optical phase singularities by computer-generated holograms," Optics Letters **17** (3), 221.

Hemsing, Erik, Andrey Knyazik, Michael Dunning, Dao Xiang, Agostino Marinelli, Carsten Hast, and James B. Rosenzweig (2013), "Coherent optical vortices from relativistic electron beams," Nature Physics **9** (9), 549–553.

Herman, R M, and T a. Wiggins (1991), "Production and uses of diffractionless beams," Journal of the Optical Society of America A **8** (6), 932.

Hickmann, J M, E. J. S. Fonseca, W. C. Soares, and S. Chávez-Cerda (2010), "Unveiling a Truncated Optical Lattice Associated with a Triangular Aperture Using Light's Orbital Angular Momentum," Physical Review Letters **105** (5), 053904.

Hörl, Anton, Andreas Trügler, and Ulrich Hohenester (2013), "Tomography of Particle Plasmon Fields from Electron Energy Loss Spectroscopy," Physical Review Letters **111** (7), 76801.

Idrobo, Juan C, and Stephen J Pennycook (2011), "Vortex beams for atomic resolution dichroism." Journal of electron microscopy **60** (5), 295–300.

Ivanov, I P, D. Seipt, A. Surzhykov, and S. Fritzsche (2016), "Elastic scattering of vortex electrons provides direct access to the Coulomb phase," Physical Review D **94** (7), 076001, arXiv:1608.06551.

Ivanov, I P, and V G Serbo (2011), "Scattering of twisted particles: Extension to wave packets and orbital helicity," Physical Review A **84** (3), 033804.

Ivanov, Igor P (2012a), "Creation of two vortex-entangled beams in a vortex-beam collision with a plane wave," Physical Review A **85** (3), 033813.

Ivanov, Igor P (2012b), "Measuring the phase of the scattering amplitude with vortex beams," Physical Review D **85** (7), 076001.

Ivanov, Igor P, and Dmitry V. Karlovets (2013a), "Detecting Transition Radiation from a Magnetic Moment," Physical Review Letters **110** (26), 264801.

Ivanov, Igor P, and Dmitry V. Karlovets (2013b), "Polarization radiation of vortex electrons with large orbital angular momentum," Physical Review A **88** (4), 043840.

Jáuregui, R (2004), "Rotational effects of twisted light on atoms beyond the paraxial approximation," Physical Review A **70** (3), 033415.

Jentschura, U D, and V G Serbo (2011), "Compton upconversion of twisted photons: backscattering of particles with non-planar wave functions," The European Physical Journal C **71** (3), 1571.

Jesacher, Alexander, Severin Fürhapter, Stefan Bernet, and Monika Ritsch-Marte (2005), "Shadow Effects in Spiral Phase Contrast Microscopy," Physical Review Letters **94** (23), 233902.

Jordan, J A, P. M. Hirsch, L. B. Lesem, and D. L. Van Rooy (1970), "Kinoform Lenses," Applied Optics **9** (8), 1883.

Juchtmans, Roeland, Armand Béché, Artem Abakumov, Maria Batuk, and Jo Verbeeck (2015), "Using electron vortex beams to determine chirality of crystals in transmission electron microscopy," Physical Review B **91** (9), 094112.

Juchtmans, Roeland, Giulio Guzzinati, and Jo Verbeeck (2016), "Extension of Friedel's law to vortex-beam diffraction," Physical Review A **94** (3), 033858, arXiv:1608.06561.

Juchtmans, Roeland, and Jo Verbeeck (2016), "Local orbital angular momentum revealed by spiral-phase-plate imaging in transmission-electron microscopy," Physical Review A **93** (2), 023811, arXiv:1512.04789.

Kanaya, Koichi, Hisazo Kawakatsu, Kazuo Ito, and Haruo Yotsumoto (1958), "Experiment on the electron phase microscope," Journal of Applied Physics **29** (7), 1046–1049.

Karimi, Ebrahim, Lorenzo Marrucci, Vincenzo Grillo, and Enrico Santamato (2012), "Spin-to-Orbital Angular Momentum Conversion and Spin-Polarization Filtering in Electron Beams," Physical Review Letters **108** (4), 44801.

Karimi, Ebrahim, Sebastian A Schulz, Israel De Leon, Hammam Qassim, Jeremy Upham, and Robert W Boyd (2014), "Generating optical orbital angular momentum at visible wavelengths using a plasmonic metasurface," Light: Science & Applications **3** (5), e167.

Karimi, Ebrahim, Gianluigi Zito, Bruno Piccirillo, Lorenzo Marrucci, and Enrico Santamato (2007), "Hypergeometric-Gaussian modes." Optics Letters **32** (21), 3053–3055, arXiv:0712.0782.

Karlovets, Dmitry (2016), "Probing phase of a scattering amplitude beyond the plane-wave approximation," EPL (Europhysics Letters) **116** (3), 31001.

Karlovets, Dmitry V (2012), "Electron with orbital angular momentum in a strong laser wave," Physical Review A **86** (6), 062102.

Khoury, a Z, and P. Milman (2011), "Quantum teleportation in the spin-orbit variables of photon pairs," Physical Review A **83** (6), 60301.

Kirkland, Earl J (2010), *Advanced Computing in Electron Microscopy* (Springer US, Boston, MA).

Kogelnik, H, and T Li (1966), "Laser beams and resonators," Proceedings of the IEEE **54** (10), 1312–1329.

Konkov, a S, a. P. Potylitsyn, and M. S. Polonskaya (2014), "Transition radiation of electrons with a nonzero orbital angular momentum," JETP Letters **100** (7), 421–425.

Kotlyar, V V, S. N. Khonina, A. A. Kovalev, V. A. Soifer, H. Elfstrom, and J. Turunen (2006), "Diffraction of a plane, finite-radius wave by a spiral phase plate," Optics Letters **31** (11), 1597.

Kotlyar, Victor V, Anton a Almazov, Svetlana N Khonina, Victor a Soifer, Henna Elfstrom, and Jari Turunen (2005), "Generation of phase singularity through diffracting a plane or Gaussian beam by a spiral phase plate." Journal of the Optical Society of America. A, Optics, image science, and vision **22** (5), 849–861.

Kotlyar, Victor V, Alexey a Kovalev, Roman V Skidanov, Oleg Yu Moiseev, and Victor a Soifer (2007), "Diffraction of a finite-radius plane wave and a Gaussian beam by a helical axicon and a spiral phase plate." Journal of the Optical Society of America. A, Optics, image science, and vision **24** (7), 1955–1964.

Krivanek, Ondrej L, Jan Rusz, Juan-Carlos Idrobo, Tracy J. Lovejoy, and Niklas Dellby (2014), "Toward Single Mode, Atomic Size Electron Vortex Beams," Microscopy and Microanalysis **20** (03), 832–836.

Kruit, P, and M. Lenc (1992), "Optical properties of the magnetic monopole field applied to electron microscopy and spectroscopy," Journal of Applied Physics **72** (10), 4505–4513.

Ladavac, Kosta, and David G Grier (2004), "Microoptomechanical pumps assembled and driven by holographic optical vortex arrays," Optics Express **12** (6), 1144–9, arXiv:0402634 [cond-mat].

Landau, L D, and E M Lifshitz (1977), *Quantum Mechanics Non-Relativistic Theory*, 3rd ed. (Pergamon Press, Oxford).

Larocque, Hugo, Frédéric Bouchard, Vincenzo Grillo, Alicia Sit, Stefano Frabboni, Rafal E. Dunin-Borkowski, Miles J. Padgett, Robert W. Boyd, and Ebrahim Karimi (2016), "Nondestructive Measurement of Orbital Angular Momentum for an Electron Beam," Physical Review Letters **117** (15), 154801.

Lax, M, W H Louisell, and W B McKnight (1975), "From Maxwell to paraxial wave optics," Physical Review A **11** (4), 1365–1370.

Leach, Jonathan, Johannes Courtial, Kenneth Skeldon, Stephen M. Barnett, Sonja Franke-Arnold, and Miles J. Padgett (2004), "Interferometric Methods to Measure Orbital and Spin, or the Total Angular Momentum of a Single Photon," Physical Review Letters **92** (1), 013601.

Leary, C C, M. G. Raymer, and S. J. van Enk (2009), "Spin and orbital rotation of electrons and photons via spin-orbit interaction," Physical Review A **80** (6), 061804.

Leary, C C, D. Reeb, and M. G. Raymer (2008), "Self-spin-controlled rotation of spatial states of a Dirac electron in a cylindrical potential via spinorbit interaction," New Journal of Physics **10** (10), 103022.

Lee, Jae, Gregory Foo, Eric Johnson, and Grover Swartzlander (2006), "Experimental Verification of an Optical Vortex Coronagraph," Physical Review Letters **97** (5), 053901.

Lee, W-H (1979), "Binary Computer Generated Holograms," Applied Optics **18**, 3661.

Lembessis, V, D. Ellinas, and M. Babiker (2011), "Azimuthal Sisyphus effect for atoms in a toroidal all-optical trap," Physical Review A **84** (4), 43422.

Lembessis, V E, and M. Babiker (2013), "Enhanced Quadrupole Effects for Atoms in Optical Vortices," Physical Review Letters **110** (8), 83002.

Lembessis, V E, and M. Babiker (2016), "Mechanical effects on atoms interacting with highly twisted Laguerre-Gaussian light," Physical Review A - Atomic, Molecular, and Optical Physics **94** (4), 1–5.

Lembessis, V E, D. Ellinas, M. Babiker, and O. Al-Dossary (2014), "Atom vortex beams," Physical Review A **89** (5), 053616.

Lloyd, S M, M Babiker, and J Yuan (2012a), "Interaction of electron vortices and optical vortices with matter and processes of orbital angular momentum exchange," Physical Review A **86** (2), 023816.

Lloyd, S M, M. Babiker, and J. Yuan (2013), "Mechanical properties of electron vortices," Physical Review A **88** (3), 031802.

Lloyd, S M, M Babiker, J Yuan, and C. Kerr-Edwards (2012b), "Electromagnetic Vortex Fields, Spin, and Spin-Orbit Interactions in Electron Vortices," Physical Review Letters **109** (25), 254801.

Lloyd, Sophia, Mohamed Babiker, and Jun Yuan (2012c), "Quantized Orbital Angular Momentum Transfer and Magnetic Dichroism in the Interaction of Electron Vortices with Matter," Physical Review Letters **108** (7), 074802.

Löffler, W, Andrea Aiello, and J. P. Woerdman (2012), "Observation of Orbital Angular Momentum Sidebands due to Optical Reflection," Physical Review Letters **109** (11), 113602.

Löffler, W, D. Broer, and J. Woerdman (2011), "Circular dichroism of cholesteric polymers and the orbital angular momentum of light," Physical Review A **83** (6), 065801.

Löfgren, André, Paul Zeiger, Vancho Kocevski, and Ján Rusz (2016), "Influence of nuclear quantum effects on frozen phonon simulations of electron vortex beam HAADF-STEM images," Ultramicroscopy **164**, 62–69.

Lubk, Axel, Laura Clark, Giulio Guzzinati, and Jo Verbeeck (2013a), "Topological analysis of paraxially scattered electron vortex beams," Physical Review A **87** (3), 033834.

Lubk, Axel, Giulio Guzzinati, Felix Börrnert, and Jo Verbeeck (2013b), "Transport of Intensity Phase Retrieval of Arbitrary Wave Fields Including Vortices," Physical Review Letters **111** (17), 173902.

MacDonald, R P, S A Boothroyd, T Okamoto, J Chrostowski, and B A Syrett (1996), "Interboard optical data distribution by Bessel beam shadowing," Optics Communications **122**, 169–177.

Magnusson, R, and T. K. Gaylord (1978), "Diffraction efficiencies of thin phase gratings with arbitrary grating shape," Journal of the Optical Society of America **68** (6), 806.

Mair, a, A Vaziri, G Weihs, and A Zeilinger (2001), "Entanglement of the orbital angular momentum states of photons." Nature **412** (6844), 313–316.

Marrucci, L, E Karimi, S Slussarenko, B Piccirillo, E Santamato, E Nagali, and F Sciarrino (2012), "Spin-to-Orbital Optical Angular Momentum Conversion in Liquid Crystal q-Plates: Classical and Quantum Applications," Molecular Crystals and Liquid Crystals **561** (1), 48–56.

Marrucci, L, C. Manzo, and D. Paparo (2006), "Optical Spin-to-Orbital Angular Momentum Conversion in Inhomogeneous Anisotropic Media," Physical Review Letters **96** (16), 163905.

Marrucci, Lorenzo (2013), "The q-plate and its future," Journal of Nanophotonics **7** (1), 078598.

Matula, O, a G Hayrapetyan, V G Serbo, A Surzhykov, and S Fritzsche (2014), "Radiative capture of twisted electrons by bare ions," New Journal of Physics **16** (5), 053024.

McGloin, D, and K Dholakia (2005), "Bessel beams: Diffraction in a new light," Contemporary Physics **46** (1), 15–28.

McMorran, B J, Amit Agrawal, I.M. M Anderson, A.A. A Herzing, H.J. J Lezec, J.J. J McClelland, and John Unguris (2011), "Electron Vortex Beams with High Quanta of Orbital Angular Momentum," Science **331** (6014), 192–195.

McMorran, Benjamin J, Amit Agrawal, Peter A. Ercius, Vincenzo Grillo, Andrew A. Herzing, Tyler R. Harvey, Martin Linck, and Jordan S. Pierce (2017), "Origins and demonstrations of electrons with orbital angular momentum," Philosophical Transactions of the Royal Society A: Mathematical, Physical and Engineering Sciences **375** (2087), 20150434.

Midgley, Paul A, and Rafal E. Dunin-Borkowski (2009), "Electron tomography and holography in materials science." Nature materials **8** (4), 271–80.

Mo, Yifei, Kevin T Turner, and Izabela Szlufarska (2009), "Friction laws at the nanoscale." Nature **457** (7233), 1116–1119.

Mohammadi, Zeinab, Cole P. Van Vlack, Stephen Hughes, Jens Bornemann, and Reuven Gordon (2012), "Vortex electron energy loss spectroscopy for near-field mapping of magnetic plasmons," Optics Express **20** (14), 15024.

Molina-Terriza, Gabriel, Juan P. Torres, and Lluis Torner (2007), "Twisted photons," Nature Physics **3** (5), 305–310.

Mousley, Michael, Gnanavel Thirunavukkarasu, Mohamed Babiker, and Jun Yuan (2015), "C-shaped electron beams: design, experimental production and application," in *Laser Beam Shaping XVI*, edited by Andrew Forbes and Todd E. Lizotte, p. 95810C.

Mutzafi, Maor, Ido Kaminer, Gal Harari, and Mordechai Segev (2014), "Non-Linear Shape Preserving Electron-Beams," in *CLEO: 2014*, 2 (OSA, Washington, D.C.) p. FM3D.7.

Nagayama, Kuniaki (2011), "60th Anniversary Issue : Biological Another 60 years in electron microscopy : development of phase-plate electron microscopy and biological applications," J Electron Microscopy **60** (Supplement 1), S43–S62.

Nelayah, Jaysen, Mathieu Kociak, Odile Stéphan, F. Javier García de Abajo, Marcel Tencé, Luc Henrard, Dario Taverna, Isabel Pastoriza-Santos, Luis M. Liz-Marzán, and Christian Colliex (2007), "Mapping surface plasmons on a single metallic nanoparticle," Nature Physics **3** (5), 348–353.

Nienhuis, G, J P Woerdman, and I. Kuščer (1992), "Magnetic and mechanical Faraday effects," Physical Review A **46** (11), 7079–7092.

Niermann, T, J. Verbeeck, and M. Lehmann (2014), "Creating arrays of electron vortices," Ultramicroscopy **136**, 165–170.

Nye, J F (2006), "Dislocation lines in the hyperbolic umbilic diffraction catastrophe," Proceedings of the Royal Society A: Mathematical, Physical and Engineering Sciences **462** (2072), 2299–2313.

Nye, J F, and M. V. Berry (1974), "Dislocations in Wave Trains," Proceedings of the Royal Society A: Mathematical, Physical and Engineering Sciences **336** (1605), 165–190.

O'Holleran, Kevin, Mark R. Dennis, Florian Flossmann, and Miles J. Padgett (2008), "Fractality of Light's Darkness," Physical Review Letters **100** (5), 053902.

O'Neil, A T, I. MacVicar, L. Allen, and M. J. Padgett (2002), "Intrinsic and Extrinsic Nature of the Orbital Angular Momentum of a Light Beam," Physical Review Letters **88** (5), 053601.

Padgett, M (1996), "An experiment to observe the intensity and phase structure of LaguerreGaussian laser modes," American Journal of Physics **64** (1), 77.

Pepino, R a, J. Cooper, D. Meiser, D. Z Anderson, and M. J Holland (2010), "Open quantum systems approach to atomtronics," Physical Review A **82** (1), 13640.

Petersen, T C, D M Paganin, M Weyland, T P Simula, S A Eastwood, and M J Morgan (2014), "Unifying interpretations of the Gouy phase anomaly for electron waves," Phys Rev A **89**, 063801.

Petersen, T C, M. Weyland, D. M. Paganin, T. P. Simula, S. a. Eastwood, and M. J. Morgan (2013), "Electron Vortex Production and Control Using Aberration Induced Diffraction Catastrophes," Physical Review Letters **110** (3), 033901.

Podolskiy, V A, A K Sarychev, and V Shalaev (2002), "Plasmon modes in metal nanowires and left-handed materials," Journal of Nonlinear Optical and Physical Materials **11** (1), 65–74.

Pohl, Darius, Jan Rusz, Jakob Spiegelberg, Sebastian Schneider, Peter Tiemeijer, Kornelius Nielsch, and Bernd Rellinghaus (2016), "Towards atomic magnetic measurements with single electron vortex beams on nanocubes," in *European Microscopy Congress 2016: Proceedings* (Wiley-VCH Verlag GmbH & Co. KGaA, Weinheim, Germany) pp. 907–908.

Pohl, Darius, Sebastian Schneider, Jan Rusz, and Bernd Rellinghaus (2015), "Electron vortex beams prepared by a spiral aperture with the goal to measure EMCD on ferromagnetic films via STEM," Ultramicroscopy **150**, 16–22.

Qiu, Jiangdong, Changliang Ren, and Zhiyou Zhang (2016), "Precisely measuring the orbital angular momentum of beams via weak measurement," Physical Review A **93** (6), 063841.

Reimer, Ludwig, and Helmut Kohl (2008), *Transmission Electron Microscopy Physics of Image Formation*, 5th ed. (Springer, Berlin).

Ricci, F, W Löffler, and M.P. van Exter (2012), "Instability of higher-order optical vortices analyzed with a multi-pinhole interferometer," Optical Express **20** (20), 22961.

Rose, H H (2008), "Optics of high-performance electron microscopes," Science and Technology of Advanced Materials **9** (1), 014107.

Ruffner, David B, and David G. Grier (2012), "Optical Forces and Torques in Nonuniform Beams of Light," Physical Review Letters **108** (17), 173602.

Rusz, Ján, and Somnath Bhowmick (2013), "Boundaries for Efficient Use of Electron Vortex Beams to Measure Magnetic Properties," Physical Review Letters **111** (10), 105504.

Rusz, Ján, Somnath Bhowmick, Mattias Eriksson, and Nikolaj Karlsson (2014), "Scattering of electron vortex beams on a magnetic crystal: Towards atomic-resolution magnetic measurements," Physical Review B **89** (13), 134428, arXiv:arXiv:1403.7730v1.

Saitoh, Koh, Yuya Hasegawa, Kazuma Hirakawa, Nobuo Tanaka, and Masaya Uchida (2013), "Measuring the Orbital Angular Momentum of Electron Vortex Beams Using a Forked Grating," Physical Review Letters **111** (7), 074801, arXiv:1307.6304.

Saitoh, Koh, Yuya Hasegawa, Nobuo Tanaka, and Masaya Uchida (2012), "Production of electron vortex beams carrying large orbital angular momentum using spiral zone plates," Journal of Electron Microscopy **0** (0), 1–7.

Saleh, B E A, and M C Teich (1991), *Fundementals of photonics* (Wiley Interscience).

Sarychev, Andrey K, Gennady Shvets, and Vladimir M. Shalaev (2006), "Magnetic plasmon resonance," Physical Review E **73** (3), 036609.

Saslow, W M (1992), "Maxwell's theory of eddy currents in thin conducting sheets, and applications to electromagnetic shielding and MAGLEV," American Journal of Physics **60** (8), 693–711.

Schachinger, T, S. Löffler, A. Steiger-Thirsfeld, M. Stöger-Pollach, S. Schneider, D. Pohl, B. Rellinghaus, and P. Schattschneider (2017), "EMCD with an electron vortex filter: Limitations and possibilities," Ultramicroscopy **179**, 15–23.

Schachinger, T, S. Löffler, M. Stöger-Pollach, and P. Schattschneider (2015), "Peculiar rotation of electron vortex beams," Ultramicroscopy **158**, 17–25.

Schattschneider, P, V Grillo, and D Aubry (2017), "Spin polarisation with electron Bessel beams," Ultramicroscopy **in press**, 1–6.

Schattschneider, P, S. Löffler, M. Stöger-Pollach, and J. Verbeeck (2014a), "Is magnetic chiral dichroism feasible with electron vortices?" Ultramicroscopy **136**, 81–85.

Schattschneider, P, S Rubino, C Hébert, J Rusz, J. Kuneš, P Novák, E Carlino, M Fabrizioli, G Panaccione, and G Rossi (2006), "Detection of magnetic circular dichroism using a transmission electron microscope," Nature **441** (7092), 486–488.

Schattschneider, P, Th Schachinger, M Stöger-Pollach, S Löffler, A Steiger-Thirsfeld, K Y Bliokh, and Franco Nori (2014b), "Imaging the dynamics of free-electron Landau states," Nature Communications **5**, 4586.

Schattschneider, P, M. Stöger-Pollach, and J. Verbeeck (2012a), "Novel Vortex Generator and Mode Converter for Electron Beams," Physical Review Letters **109** (8), 084801.

Schattschneider, P, and J. Verbeeck (2011), "Theory of free electron vortices," Ultramicroscopy **111** (9-10), 1461–1468.

Schattschneider, Peter, Bernhard Schaffer, Inga Ennen, and Johan Verbeeck (2012b), "Mapping spin-polarized transitions with atomic resolution," Physical Review B **85** (13), 134422.

Schmidt, L Ph H, C. Goihl, D. Metz, H. Schmidt-Böcking, R. Dörner, S. Yu Ovchinnikov, J. H. Macek, and D. R. Schultz (2014), "Vortices associated with the wave function of a single electron emitted in slow ion-atom collisions," Physical Review Letters **112** (8), 1–5.

Seaman, B T, M. Krämer, D. Z. Anderson, and M. J. Holland (2007), "Atomtronics: Ultracold-atom analogs of electronic devices," Physical Review A **75** (2), 23615, arXiv:0606625v1 [arXiv:cond-mat].

Seipt, D, a. Surzhykov, and S. Fritzsche (2014), "Structured x-ray beams from twisted electrons by inverse Compton scattering of laser light," Physical Review A - Atomic, Molecular, and Optical Physics **90** (1), 1–7, arXiv:arXiv:1407.4329v1.

Serbo, V, I. P. Ivanov, S. Fritzsche, D. Seipt, and a. Surzhykov (2015), "Scattering of twisted relativistic electrons by atoms," Physical Review A **92** (1), 012705.

Shiloh, Roy, Yossi Lereah, Yigal Lilach, and Ady Arie (2014), "Sculpturing the electron wave function using nanoscale phase masks," Ultramicroscopy **144**, 26–31.

Shiloh, Roy, Yuval Tsur, Roei Remez, Yossi Lereah, Boris a. Malomed, Vladlen Shvedov, Cyril Hnatovsky, Wieslaw Krolikowski, and Ady Arie (2015), "Unveiling the Orbital Angular Momentum and Acceleration of Electron Beams," Physical Review Letters **114** (9), 096102.

Speirits, Fiona C, and Stephen M. Barnett (2013), "Do Waves Carrying Orbital Angular Momentum Possess Azimuthal Linear Momentum?" Physical Review Letters **111** (10), 103602.

Sueda, K, G Miyaji, N Miyanaga, and M Nakatsuka (2004), "Laguerre-Gaussian beam generated with a multilevel spiral phase plate for high intensity laser pulses," Optics Express **12** (15), 3548.

Surzhykov, A, D. Seipt, V. G. Serbo, and S. Fritzsche (2015), "Interaction of twisted light with many-electron atoms and ions," Physical Review A **91** (1), 013403.

Swartzlander, Grover A, and Raul I. Hernandez-Aranda (2007), "Optical Rankine Vortex and Anomalous Circulation of Light," Physical Review Letters **99** (16), 163901.

Takahashi, Ryuji, and Naoto Nagaosa (2015), "Berry curvature and orbital angular momentum of electrons in angle-resolved photoemission spectroscopy," Physical Review B **91** (24), 245133.

Tamburini, Fabrizio, Bo Thidé, Gabriel Molina-Terriza, and Gabriele Anzolin (2011), "Twisting of light around rotating black holes," Nature Physics **7** (3), 195–197.

Thidé, B, H. Then, J. Sjöholm, K. Palmer, J. Bergman, T. D. Carozzi, Ya. N. Istomin, N. H. Ibragimov, and R. Khamitova (2007), "Utilization of Photon Orbital Angular Momentum in the Low-Frequency Radio Domain," Physical Review Letters **99** (8), 087701.

Thirunavukkarasu, G, M Mousley, M Babiker, and J Yuan (2017), "Normal modes and mode transformation of pure electron vortex beams," Philosophical Transactions of the Royal Society A: Mathematical, Physical and Engineering Sciences **375** (2087), 20150438.

Thole, BT, P Carra, F Sette, and G. Van der Laan (1992), "X-ray circular dichroism as a probe of orbital magnetization," Physical review letters **68** (12), 1943–1946.

Tonomura, Akira (1987), "Applications of electron holography," Reviews of Modern Physics **59** (3), 639–669.

Turnbull, G (1996), "The generation of free-space Laguerre-Gaussian modes at millimetre-wave frequencies by use of a spiral phaseplate," Optics Communications **127** (4-6), 183–188.

Uchida, Masaya, and Akira Tonomura (2010), "Generation of electron beams carrying orbital angular momentum." Nature **464** (7289), 737–9.

van Boxem, Ruben, Bart Partoens, and Jo Verbeeck (2015), "Inelastic electron-vortex-beam scattering," Physical Review A **91** (3), 032703.

van Boxem, Ruben, Bart Partoens, and Johan Verbeeck (2014), "Rutherford scattering of electron vortices," Physical Review A **89** (3), 032715.

Van Enk, SJ J, G. Nienhuis, S J Van Enk, and G. Nienhuis (1994), "Commutation Rules and Eigenvalues of Spin and Orbital Angular Momentum of Radiation Fields," Journal of Modern Optics **41** (5), 963–977.

Velasco-Martínez, D, V. G. Ibarra-Sierra, J. C. Sandoval-Santana, J. L. Cardoso, and A. Kunold (2016), "Singularities and internal rotational dynamics of electron beams," Physical Review A **94** (6), 063815.

Verbeeck, J, P Schattschneider, S Lazar, M. Stoger-Pollach, S. Loffler, A. Steiger-Thirsfeld, and G. Van Tendeloo (2011a), "Atomic scale electron vortices for nanoresearch," Applied Physics Letters **99** (20), 203109.

Verbeeck, J, H. Tian, and P. Schattschneider (2010), "Production and application of electron vortex beams." Nature **467** (7313), 301–4.

Verbeeck, J Jo, H. He Tian, and a. Béché (2012), "A new way of producing electron vortex probes for STEM," Ultramicroscopy **113**, 83–87.

Verbeeck, Jo, Giulio Guzzinati, Laura Clark, Roeland Juchtmans, Ruben van Boxem, He Tian, Armand Béché, Axel Lubk, and Gustaaf Van Tendeloo (2014), "Shaping electron beams for the generation of innovative measurements in the (S)TEM," Comptes Rendus Physique **15** (2-3), 190–199.

Verbeeck, Jo, Peter Schattschneider, S Lazar, M Stöger-Pollach, and Stefan Loffler (2011b), "Atomic scale elec-

tron vortices for nanoresearch (supplementary material)," Applied Physics Letters **99** (October 2011), 1–6.

Verbeeck, Jo, He Tian, and Gustaaf Van Tendeloo (2013), "How to Manipulate Nanoparticles with an Electron Beam?" Advanced Materials **25** (8), 1114–1117.

Wang, Yan, and Chun-Fang Li (2011), "Bessel-Gaussian electron beams of cylindrically symmetric spin polarization," EPL (Europhysics Letters) **95** (4), 44001.

Williams, David B, and C Barry Carter (2009), *Transmission Electron Microscopy* (Springer US, Boston, MA).

Wu, Tai Tsun, and Chen Ning Yang (1976), "Dirac monopole without strings: Monopole harmonics," Nuclear Physics B **107** (3), 365–380.

Xie, L, P. Wang, and X.Q. Pan (2014), "A perturbation theory study of electron vortices in electromagnetic fields: The case of infinitely long line charge and magnetic dipole," Micron **63**, 9–14.

Xin, Huolin L, and Haimei Zheng (2012), "On-Column 2p Bound State with Topological Charge 1 Excited by an Atomic-Size Vortex Beam in an Aberration-Corrected Scanning Transmission Electron Microscope," Microscopy and Microanalysis **18** (04), 711–719.

Yao, Alison M, and Miles J Padgett (2011), "Orbital angular momentum : origins , behavior and applications," Advances in Optics and Photonics **204**, 161–204.

Yuan, J, S. M. Lloyd, and M Babiker (2013), "Chiral-specific electron-vortex-beam spectroscopy," Physical Review A **88** (3), 031801.

Yuan, J, and N. K. Menon (1997), "Magnetic linear dichroism in electron energy loss spectroscopy," Journal of Applied Physics **81** (8), 5087.

Yuan, Jun (2014), "Bright electron twisters," Nature **509**, 37.

Zaytsev, V A, V. G. Serbo, and V. M. Shabaev (2017), "Radiative recombination of twisted electrons with bare nuclei: Going beyond the Born approximation," Physical Review A **95** (1), 012702, arXiv:1610.09648.

Züchner, Tina, Antonio Virgilio Failla, and Alfred J. Meixner (2011), "Light microscopy with doughnut modes: a concept to detect, characterize, and manipulate individual nanoobjects." Angewandte Chemie (International ed. in English) **50** (23), 5274–93.